PLASMONICS FOR NANOTECHNOLOGY:

ENERGY HARVESTING AND MEMORY DEVICES

A Dissertation

Submitted to the Faculty

of

Purdue University

by

Aveek Dutta

In Partial Fulfillment of the

Requirements for the Degree

of

Doctor of Philosophy

August 2020

Purdue University

West Lafayette, Indiana

THE PURDUE UNIVERSITY GRADUATE SCHOOL
STATEMENT OF DISSERTATION APPROVAL

Dr. Alexandra Boltasseva, Chair

    Department of Electrical and Computer Engineering

Dr. Vladimir M. Shalaev

    Department of Electrical and Computer Engineering

Dr. Alexander V. Kildishev

    Department of Electrical and Computer Engineering

Dr. Ernesto E. Marinero

    Department of Materials Science and Engineering

Approved by:

    Dr. Dimitrios Peroulis

        Head of the School Graduate Program

to my grandparents

late Mr. Basudev Dutta, late Mrs. Chameli Dutta,

Mr. Nanda Dulal Dutta and late Mrs. Sucheta Dutta

ACKNOWLEDGMENTS

As I am writing my thesis, after nearly seven years of PhD research, I realize that there is a lot of difference between the person who began this PhD journey and the person who is about to complete it. Over the last several years, I have not only become more mature as a scientific researcher but also as an individual. This of course would not have been possible without the guidance and support of a number of people. And all of them deserve an acknowledgement from my side.

So I would like to begin by expressing my immense gratitude to my advisors Prof. Vladimir M. Shalaev and Prof. Alexandra Boltasseva. They have not only helped me navigate the twist and turns of graduate research but also supported me tremendously as I searched for possible postdoc and research opportunities after graduation. I would like to thank Prof. Alexander V. Kildishev for helping me master the intricacies of numerical simulations of electromagnetic problems. I would also like to thank Prof. Ernesto E. Marinero for introducing me to the amazing phenomenon that is magnetism and to Dr. Alexei Lagoutchev for valuable guidance in designing optical experiments. Finally, a special mention to Prof. Vladimir Belotelov who helped me complete my research involving magnetic materials under very challenging circumstances.

A notable PhD experience is made not only by caring advisors but also by very supportive colleagues. So I would like to thank all the former members of our research group who helped me gel seamlessly into the research activities of our group. PhD research invariably includes a lot of failures, to overcome which one needs very pragmatic group members. I would like to thank all the members of our research group who have worked diligently by my side over the last few years and provided constant encouragement in times of hardships. I am fortunate to have had the opportunity to conduct research in a world-class facility like the Birck Nanotechnology Center.

So I would also like to acknowledge all the Birck staff members who have helped me during my PhD, from technical inputs on sample preparation to help with research grant related expenses.

Last but not least, I am immensely thankful to my family. Being somewhat of a a workaholic with numerous hobbies outside academia, on multiple occasions I have prioritized research work or extracurricular activities over the usual weekend call back to my home in India. This, understandably, has not made the life of my family members, especially my parents, any less stressful. However, they have always been a constant voice of reason and calm during the time of my PhD research. And I don't have words to express my gratitude to them.

TABLE OF CONTENTS

LIST OF FIGURES

Figure   Page

ABSTRACT

Dutta, Aveek Ph.D., Purdue University, August 2020. Plasmonics for Nanotechnology: Energy Harvesting and Memory Devices. Major Professor: Alexandra Boltasseva.

My dissertation research is in the field of plasmonics. Specifically, my focus is on the use of plasmonics for various applications such as solar energy harvesting and optically addressable magnetic memory devices. Plasmonics is the study of collective oscillations of free electrons in a metal coupled to an electromagnetic field. Such oscillations are characterized by large electromagnetic field intensities confined in nanoscale volumes and are called plasmons. Plasmons can be excited on a thin metal film, in which case they are called surface plasmon polaritons or in nanoscale metallic particles, in which case they are called localized surface plasmon resonances. Researchers have taken advantage of this electromagnetic field enhancement resulting from the excitation of plasmons in metallic structures and demonstrated phenomenon such as plasmon-assisted photocatalysis, plasmon-induced local heating, plasmon-enhanced chemical sensing, optical modulators, nanolasers, etc.

In the first half of my dissertation, I study the role of plasmonics in hydrogen production from water using solar energy. Hydrogen is believed to be a very viable source of alternative green fuel to meet the growing energy demands of the world. There are significant efforts in government and private sectors worldwide to implement hydrogen fuel cells as the future of the automotive and transportation industry. In this regard, water splitting using solar energy to produce hydrogen is a widely researched topic. It is believed that a Solar-to-Hydrogen (STH) conversion efficiency of 10% is good enough to be considered for practical applications. Iron oxide (α-Fe_2O_3) or hematite is one of the candidate materials for hydrogen generation by water splitting with a

theoretical STH efficiency of about 15%. In this work, I experimentally show that through metallic gold nanostructures we can enhance the water oxidation photocurrent in hematite by two times for above bandgap wavelengths, thereby increasing hydrogen production. Moreover, I also show that gold nanostructures can result in a hematite photocurrent enhancement of six times for below bandgap wavelengths. The latter, I believe, is due to the excitation of plasmons in the gold nanostructures and their subsequent decay into hot holes which are harvested by hematite.

The second part of my dissertation involves data storage in magnetic media. Memory devices based on magnetic media have been widely investigated as a compact information storage platform with bit densities exceeding $1Tb/in^2$. As the size of nanomagnets continue to reduce to achieve higher bit densities, the magnetic fields required to write information in these bits increases. To counter this, the field of heat-assisted magnetic recording (HAMR) was developed where a laser is used to locally heat up a magnet and make it susceptible to smaller magnetic switching fields. About two decades ago, it was realized that a single femtosecond laser pulse can switch magnetic media and therefore could be used to write information in magnetic bits. This field is now known as All-Optical Magnetic Switching (AOMS). My research aims to bring together the two fields of HAMR and AOMS to create optically addressable nanomagnets for information storage. Specifically, I want to show that plasmonic resonators can couple the laser field to nanomagnets more efficiently. This can therefore be used not only to heat the nanomagnets but also switch them with lower optical energy compared to free-standing nanomagnets without any plasmonic resonator. The results of my research show that by coupling metallic resonators, supporting surface plasmons, to nanomagnets, one can reduce the light intensity required for laser induced magnetization reversal.

1. INTRODUCTION

For over a millennia light has been omnipresent in scientific research and literature. Early Greek philosophers like Aristotle, Socrates and Plato studied the nature of light during the 3rd and 4th century B.C. Euclid's book on optics provides references to reflection, diffusion and other optical phenomenon [1]. Over a millenium later, Ibn al-Haytham, an Islamic philosopher wrote his "Book of Optics" during the 11th century which can be regarded as a precursor to numerous experiments in modern optics. Come the 17th century and we have Sir Isaac Newton who studied light as being composed of different colors [2] and also proposed the corpuscular theory of light in his book "Opticks". Around the same time, Christiaan Huygens proposed his theory on the wave nature of light which was supported experimentally by Thomas Young in the 19th century. Later James Clerk Maxwell explained that light can be thought of as electromagnetic waves described by four equations which collectively came to be known as Maxwell's Equations. By now, there seemed to be enough evidence against Newton's corpuscular theory of light. However, the beginning of the 20th century saw the emergence of Albert Einstein. In his 1905 paper on the photoelectric effect, Einstein firmly established that light is composed of particles called photons. The 20th century also saw the emergence of quantum mechanics and concepts such as the wave-particle dual nature of fundamental particles like electrons. The theoretical foundations of the quantum theory were established by the pioneering works of Max Planck, Ernst Schrodinger, William Heisenberg, Paul Dirac and others. Following these works, the laws of quantum mechanics and not Newtonian mechanics, were accepted as the description of physics around us for all length scales, barring astronomical. It was only later during the 1960s that George Sudarshan, Roy Glauber and Leonard Mandel provided a successful quantum description of the photon thereby giving birth to the field of quantum optics [3]. Incidentally, the same decade saw the

emergence of two very influential sub-fields of optics namely lasers in 1960 [4] and nonlinear optics in 1961 [5]. Over the next several decades, these two topics have worked hand-in-hand to deliver ground breaking progress in technology from optical communications, to microscopy, spectroscopy, sensing and others. I should clarify at this point that this paragraph is by no means an attempt to summarize centuries worth of research in light and optics. Something like that is beyond the scope of my thesis as well as my knowledge. This is just a platform on which I can now introduce plasmonics.

Photons by themselves are non-interacting and hence to the best of my knowledge, they can only be studied or leveraged when they interact with matter. Plasmonics is the field of optical science that deals with interaction of light/photons with metals. Such interaction manifests as collective oscillation of free electrons in a metal coupled to electromagnetic waves. These oscillations are called surface plasmons and were first theoretically predicted by R. Ritchie in 1957 [6]. They were subsequently observed in aluminum and magnesium thin films with electron energy loss spectroscopy by Powell and Swan [7, 8]. These early demonstrations were followed by works of Raether, Kretschmann and Otto in the 1960s and 70s where they observed and characterized the nature of surface plasmons in metallic gratings or films of silver [9–11]. Surface plasmons have very large wave-vectors and hence they are ideally suited to couple light to sub-wavelength dimensions. Besides high confinement, plasmons in metallic structures also result in very large intensities on the electromagnetic field in nanoscale volumes [12,13]. Hence metal-based optics or plasmonics has been widely proposed for many applications in the field of optics, chemical and biological sensing, etc. Over the last couple of decades, with the advent of state-of-the-art nanofabrication facilities, the field of plasmonics has witnessed renewed interest from the scientific community. Plasmonics has been demonstrated for on-chip optical modulators, holograms, optical tweezers, nanolasers, chemical and biological sensing, catalysis, etc. [14–23]. In the following sections I will briefly review the fundamentals of plasmonics, different ma-

terials that have been investigated for plasmonic applications and some applications of plasmonics in nanotechnology relevant to my research.

1.1 Fundamentals of plasmonics

Plasmonics, as I have stated earlier, deals with the collective oscillations of free electrons in a metal coupled to electromagnetic waves. In general, the response of a metal to incident electromagnetic waves depends on its permittivity $\varepsilon_m(\omega)$, where ω is the frequency of the electromagnetic wave. Mathematically, the permittivity can be expressed as $\varepsilon_m(\omega) = \varepsilon'(\omega) + i\varepsilon''(\omega)$. $\varepsilon'(\omega)$ is the real part of permittivity (negative for a metal) and characterizes the reflectivity of the metal. $\varepsilon''(\omega)$ is the imaginary part of permittivity and characterizes the optical losses in the metal. I will present more details on the permittivity of metals in the Materials section of the chapter. The interface of a metal and a dielectric can support a special type of excitation called a Surface Plasmon Polariton (SPP). SPPs are propagating excitations along the interface and are characterized by wavevector much greater than that of free space light with evanescent coupling in the perpendicular direction [12]. Due to the wavevector mismatch with free-space light, SPPs can only be excited on metal-dielectric interface through prism-couplers or gratings. The propagation of the SPP along the x-axis is characterized by a transverse-magnetic (TM) or p polarization and is associated with a surface charge density fluctuation, as shown in Figure 1.1a. In addition, the out-of-plane electric field component E_z decays along the normal direction to the interface with different penetration depths in the metal (δ_m) and the dielectric (δ_d) (Figure 1.1a). These quantities are typically in the order of 100 nm–1 μm, and are inversely proportional to the propagation length of the SPP (i.e., 10 μm–1 mm) [24, 25]. The characteristic SPP wavevector k_{spp} and frequency ω_{spp} are given by [12]:

$$k_{spp} = k_0\sqrt{\frac{\varepsilon_m}{\varepsilon_m + \varepsilon_d}} \tag{1.1}$$

$$\omega_{spp} = \frac{\omega_p}{\sqrt{1 + \varepsilon_d}} \tag{1.2}$$

where k_0 is the free space wavevector of the electromagnetic wave, ω_p is the plasma frequency of the metal and ε_d is the permittivity of the dielectric. While we have propagating plasmons along the interface of a metal and a dielectric, for nanoparticles or nanostructures we have the so-called Localized Surface Plasmon Resonance (LSPR). Contrary to SPPs, LSPRs are non-propagating plasmon excitations and can be directly excited by free-space light. Figure 1.1b shows the schematic of the electric field profile and charge distribution for LSPRs in small spherical metal particles. The essential features of LSPRs can be understood by considering a quasi-static approximation, valid for spherical metal particles, where the particle radius R is such that $2R << \lambda$ (small) and $\varepsilon'' << 1$ where λ is the wavelength of the incident light. In this case, the particle polarizability α exhibits a resonance for the Frölich condition, $\varepsilon'(\omega) = -2\varepsilon_d$, and the LSPR frequency is given by

$$\omega_{LSPR} = \frac{\omega_p}{\sqrt{1 + 2\varepsilon_d}} \tag{1.3}$$

A characteristic feature of LSPRs is the electric field enhancement in nanoscale volumes. This is particularly evident in nanostructures exhibiting sharp corners, as shown in Figure 1.1c and d. Through numerical simulations it has been shown that a 75 nm silver cube shows three orders of magnitude enhancement in the electric field at the corners when illuminated with 420 nm wavelength light [26]. Still higher enhancements can be obtained in nm-scale gaps between metal nanostructures; these are particularly useful for enhancing the brightness of emitters as well as for local heating. The electromagnetic waves exciting LSPRs can either be absorbed or scattered by the nanoparticle. The corresponding absorption and scattering cross-sections are respectively given by [27]:

$$\sigma_{abs} = 4\pi k_0 R^3 Im[\frac{\varepsilon_m - \varepsilon_d}{\varepsilon_m + 2\varepsilon_d}] \tag{1.4}$$

$$\sigma_{sca} = \frac{8\pi}{3} k_0^4 R^6 \mid \frac{\varepsilon_m - \varepsilon_d}{\varepsilon_m + 2\varepsilon_d} \mid^2 \tag{1.5}$$
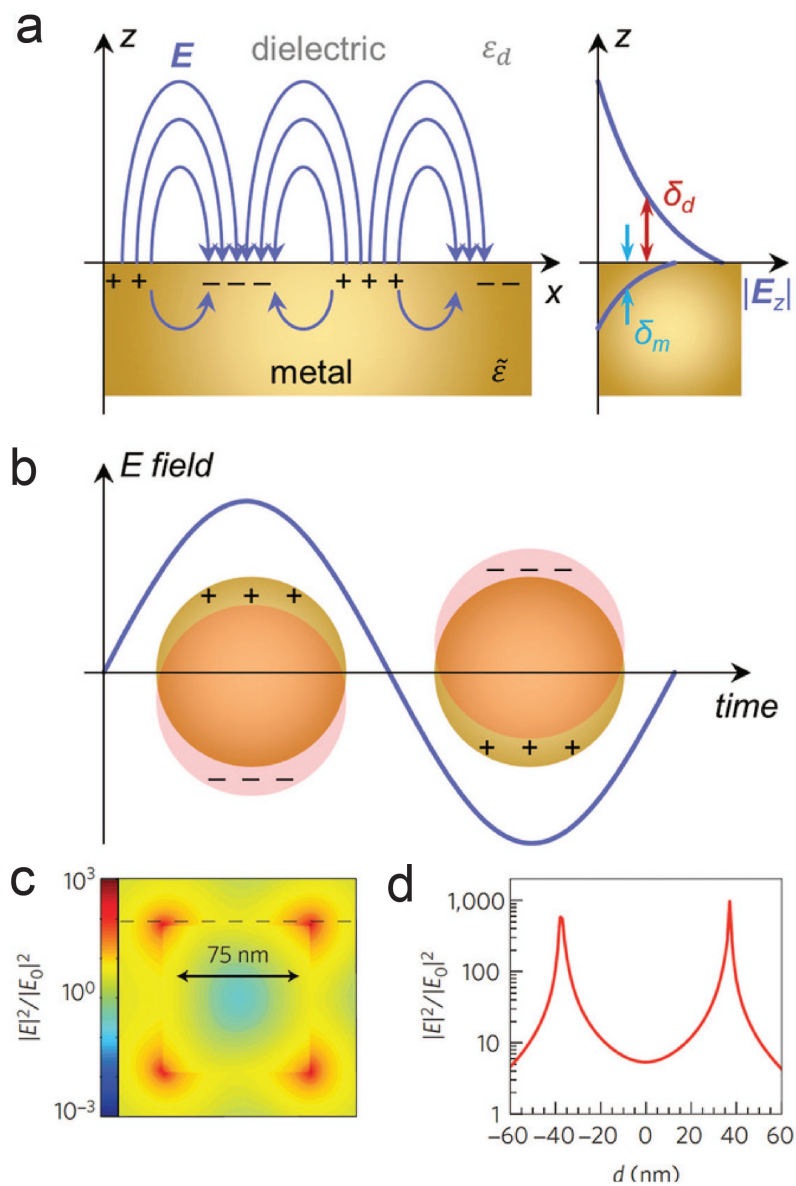
Fig. 1.1. a) Electric field distribution for a surface plasmon polariton (SPP) propagating along a metal-dielectric interface. b) Electric field distribution for localized surface plasmon (LSP). c) Spatial distribution of the LSP-induced enhancement of the electric field intensity at 420 nm wavelength, determined from a finite-difference time-domain (FDTD) simulation for a 75 nm Ag nanocube. d) The electric field profile vs. distance calculated along the dashed line in c. (c and d taken from [26])

Note that the different scaling laws for the absorption(R^3) and scattering(R^6) imply that smaller particles predominantly absorb radiation upon LSPR excitation whereas larger particles ($R >$ 50nm) scatter light upon LSPR excitation [28]. For such large particles though, the quasi-static approximation is no longer valid and Mie theory, valid for spherical particles of arbitrary size, must be considered [29]. Nevertheless, the scaling laws with particle size still remains valid. Figure 1.2 shows how the absorption and scattering cross-sections vary with different size and excitation wavelength for gold nanoparticles in air (taken from [30]). Besides the size of metal nanoparticles, the LSPR resonance frequency and the scattering and absorption cross-sections can also be tuned by controlling their shape. For a detailed review the reader can refer to [31]. With this brief overview of plasmonics I will now provide a small overview of materials used for plasmonics followed by a highlight of a couple of applications of plasmonics relevant to my thesis.

1.2   Materials for Plasmonics

The widespread application of plasmonics in the fields of physics, chemistry and biology would not have been possible without a diverse material database. As mentioned earlier, the optical properties of a plasmonic metal is characterized by the permittivity ε_m. A typical mathematical expression of the permittivity of a metal is given by the Drude-Lorentz formula as

$$\varepsilon_m = \varepsilon_\infty - \frac{\omega_p^2}{\omega_D^2 + i\Gamma_D\omega} + \sum_k \frac{A_k}{\omega_k^2 - i\Gamma_k\omega - \omega^2} \tag{1.6}$$

where ε_∞ is the optical response of the metal due to absorption at deep UV wavelengths. The next term in the equation is the Drude term which accounts for the free electrons in the metal where Γ_D is the scattering rate of the free electrons in the metal. The terms in the summation in Eq. 1.6 are Lorentz oscillators which account for optical losses due to band-to-band absorption. Here A_k is the amplitude of the Lorentz term and ω_k and Γ_k is the corresponding center frequency and spectral width of absorption. The parameters of Eq. 1.6 are generally obtained by a measurement
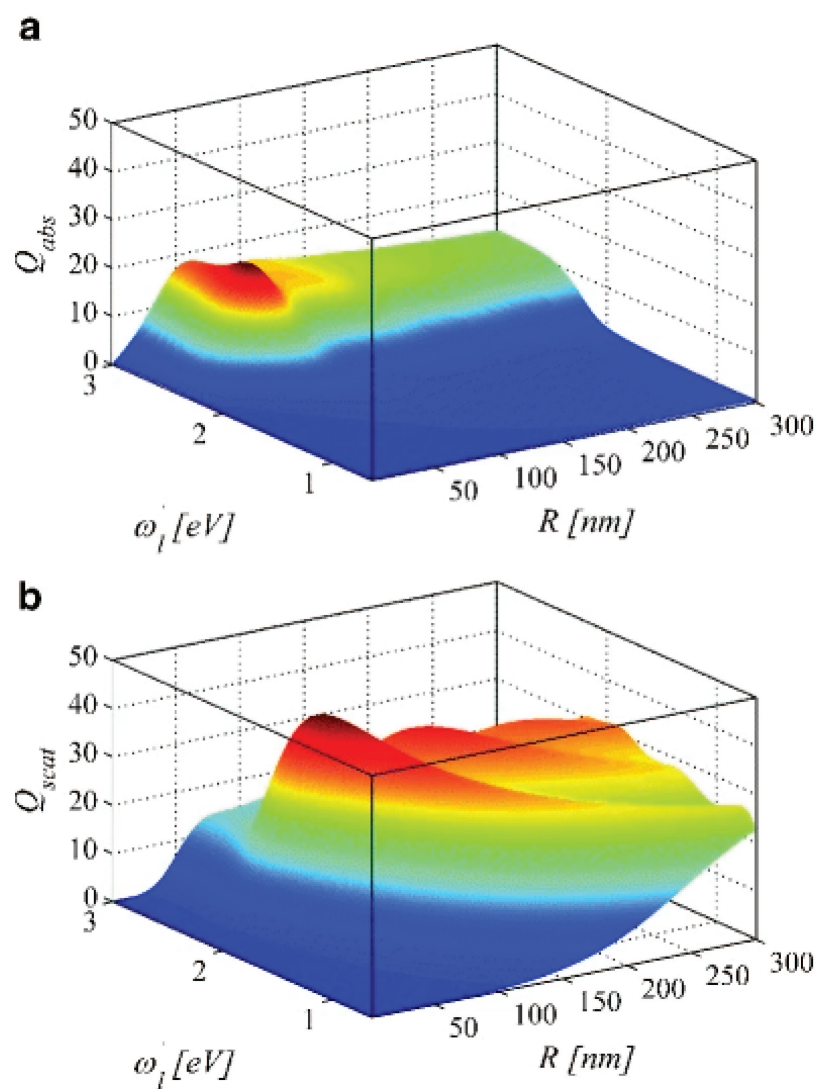
Fig. 1.2. Efficiency of a) absorption $Q_{abs}(\omega_l, R)$ and b) scattering $Q_{sca}(\omega_l, R)$ of gold nanospheres in air obtained from Mie theory based calculations ($Q = \sigma/S$, where σ is either the absorption or scattering cross-section and S is the particle area).

technique known as Variable Angle Spectroscopic Ellipsometry [32,33]. Eq. 1.6 is by no means the only formula to describe the permittivity of metals. The permittivity can have additional terms like Tauc-Lorentz, Cody-Lorentz, Gaussian, etc. [32,33].

As for the choice of materials, gold and silver have been the two most widely investigated materials for plasmonics [34–39]. These noble metals have excellent metallic properties and very low losses in the visible. Besides gold and silver, other metals such as aluminum and copper have also been studied for plasmonic applications [40–44]. Some more metals that have been investigated for plasmonics include magnesium, lead, niobium, etc [45–47]. Gold and silver are expensive plasmonic materials whereas, apart from gold, the other metals like silver, aluminum and copper suffer from chemical instability as they are prone to oxidation. This invariably leads to poor metallic properties and plasmonic behavior over time. Although researchers have demonstrated methods to overcome the low thermal stability of gold and oxidation of silver, with a passivation layer alumina grown through Atomic Layer Deposition (ALD), integrating such methods can be challenging in certain cases [48,49]. These drawbacks, along with CMOS incompatibility of noble metals, has led to a widespread search for alternate plasmonic materials over the last decade [50]. Transition Metal Nitrides (TMNs) such as Titanium Nitride (TiN) and Zirconium Nitride (ZrN) have been proposed as suitable replacements of noble metals for plasmonics [51–53]. TMNs have very high thermal stability, are biocompatible and can be processed with standard CMOS technologies [54–56]. These materials can be grown epitaxially on substrates like Magnesiun Oxide (MgO) and have optical properties comparable to that of gold. Figure 1.3a shows the optical permittivity of gold, epitaxial silver on MgO and TiN on MgO. As we can see, epitaxial silver has the lowest of losses among these metals. While gold, silver and TiN are excellent plasmonic materials in the visible, Transparent Conducting Oxides (TCOs) like Tin-doped Indium Oxide, Aluminium and Gallium-doped Zinc Oxide (AZO and GZO) are the choice for plasmonics at infrared wavelengths [51]. Figure 1.3b shows the permittivity of AZO and GZO. As can be seen these materials have very low losses near the telecommunication wavelengths.

This has sparked lot of research in TCOs for optical modulators at telecommunication wavelengths, Epsilon-Near-Zero materials and nonlinear optics [57–60]. Figure 1.3c shows the permittivity of TiN films that are 10 nm or lower in thickness. These ultrathin films show quantum confinement effects leading to wavevector dependent plasma frequency and are referred to as transdimensional materials [61,62]. Graphene has also made its mark in plasmonics and has been researched widely by the community [63–65]. Recently, a class of materials called Transition Metal Dichalcogenides (MXenes) have also received a lot of attention in the scientific community [66–68]. These materials have outstanding electrochemical properties and can be potentially used as electrocatalysts as well as for plasmonics.
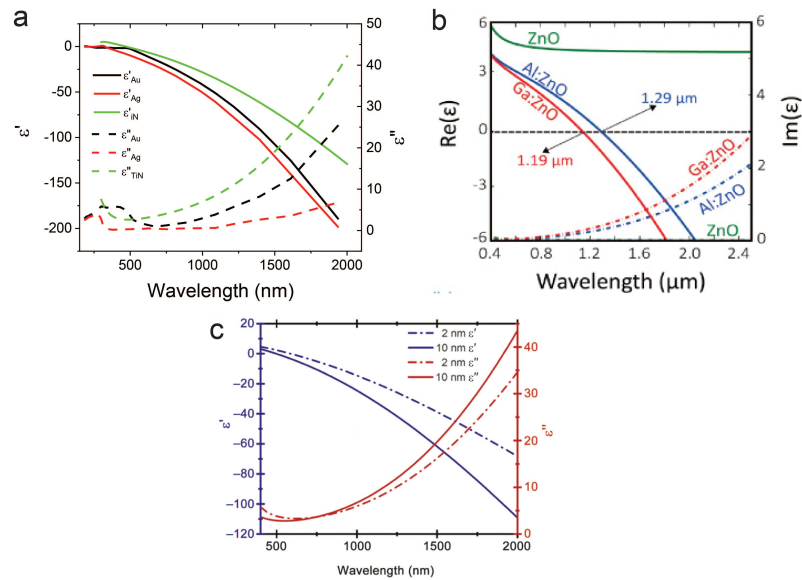
Fig. 1.3. a) Real and imaginary part of the permittivity of optically thick films of gold, epitaxial silver on MgO and Titanium Nitride on MgO measured with spectroscopic ellipsometry. b) Permittivity (real and imaginary) of transparent conducting oxides like Aluminium and Gallium-doped Zinc Oxide (taken from [58]). c) Permittivity (real and imaginary) of transdimensional metals (taken from [62]).

1.3 Applications of Plasmonics

Plasmons can decay with the excitation of a free electron in the conduction band of the metal above the Fermi energy. Such excitations are referred to as "hot electrons" and create a non-equilibrium population of electrons above the Fermi surface. Hot electrons thermalize and return to the Fermi surface through electron-electron and electron-phonon scattering in timescales that can range from tens to hundreds of picoseconds. However, before relaxation, these hot electrons can be harvested by tunnelling through a Schottky barrier or a tunnel junction for catalysis or photocurrent generation [69, 70]. Figure 1.4a shows gold nanoparticles on TiO_2 and the schematic of hot electron generation from plasmon decay. The generated hot electrons can be detected through tunneling over a Schottky barrier (bottom left) or tunneling across an insulating barrier in a metal-insulator-metal configuration (bottom middle) or metal-insulator-semiconductor configuration (bottom right) [71]. I will cover hot electron generation and its application for photocatalysis in more detail in Chapter 2. Surface plasmons can also decay into the phonon modes of the metallic structure and lead to local heat generation [72]. This phenomenon can be very useful in different fields of science and technology. For example, plasmon induced heat generation in metallic nanoparticles has been suggested for photothermal therapy [73]. Plasmon induced heating has also been investigated for Heat Assisted Magnetic Recording (HAMR) [74]. I will cover more details on HAMR in Chapter 4. Figure 1.4b illustrates the concepts of local heating with surface plasmons [72]. Figure 1.4b (left top) shows SEM image of a gold nanowire 600 nm long, 13 nm thick and 100 nm wide connecting two gold pads. Figure 1.4b (left bottom shows) the diffraction limited measurement of change in conductance as a laser is scanned across the sample surface. The laser is a 785 nm wavelength $20kW/cm^2$ Gaussian beam with fwhm of 1.8 μm. Figure 1.4b (right) shows the simulated and experimentally measured change in temperature as a function of the width of the nanowire. As can be seen, the maximum change in temperature is 1K. However plasmon induced heating can lead to a

temperature rise of several tens to hundreds of Kelvins depending on the laser power and the particular plasmonic excitation [75, 76].

With this brief overview of plasmonics, it is now time to move towards the main part of my thesis. As stated in the title, I will focus on two projects related to plasmonics that I have worked on during my PhD. The first one is gap plasmon-enhanced solar water splitting. So, in Chapter 2, I will present an overview of solar water splitting and hydrogen generation from water to be used as a renewable fuel, as well as the role of plasmonics in this phenomenon. Then in Chapter 3, I will provide details of my research work in this area. My second project is on magnetic memory devices and the role of optics in storing information in magnets. So, in Chapter 4, I will present a brief overview of techniques like Heat Assisted Magnetic Recording (HAMR) and All-Optical Magnetic Switching (AOMS) using femtosecond (fs) laser pulses. In Chapter 5, I will detail my research on using plasmonics to switch magnets in an energy efficient way. Finally, in Chapter 6, I will provide future research directions for both these projects that I feel are promising.
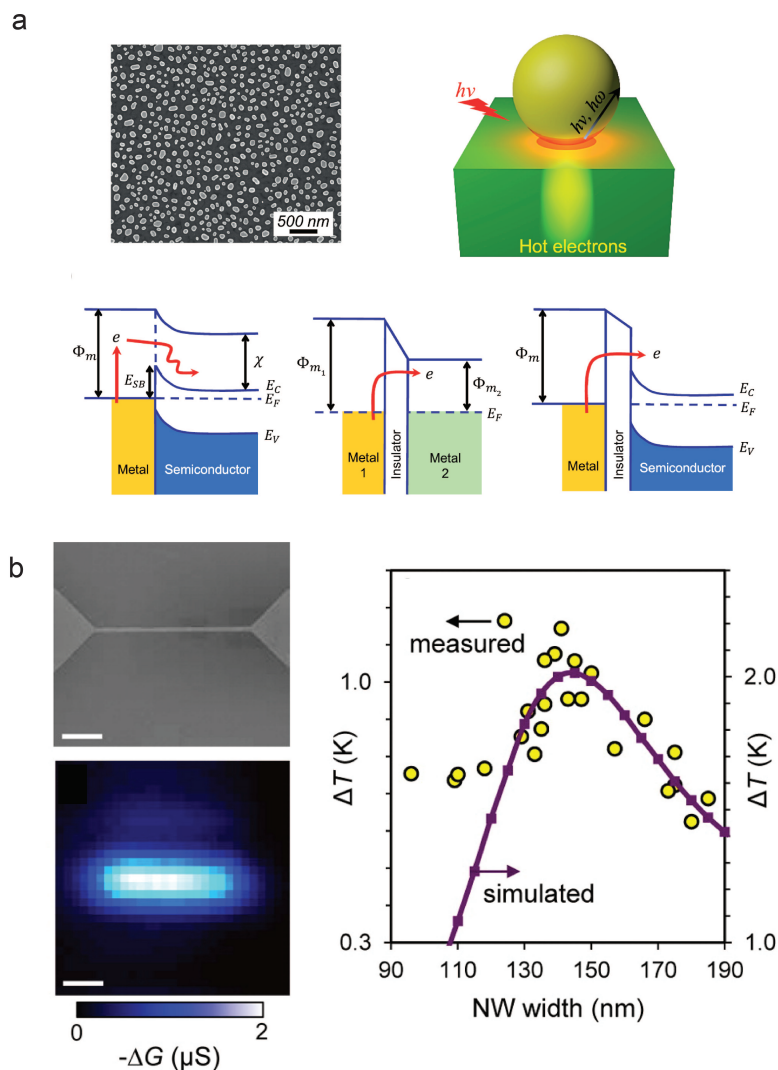
Fig. 1.4. a) The top left shows a SEM image of gold nanoparticles on TiO$_2$ semiconductor. Top right shows a scheme for the generation of hot electrons in a metal nanoparticle on a semiconductor enhanced by surface plasmons. Different mechanisms for the detection of hot electrons are presented (from left to right): a metal-semiconductor Schottky diode, a metal-insulator-metal tunnel device, and a metal-oxide-semiconductor device (bottom) (taken from [71]). b) Image of a gold nanowire on 0.2 μm of SiO$_2$ and room-temperature diffraction-limited scans of the change in conductance due to optical heating with light polarization perpendicular to the nanowire length. Scale-bar 1 μm (left). Calculated and simulated plasmonic heating as a function of nanowire width for sample at T = 300 K on a substrate with 0.2 μm thick oxide (right) (taken from [72]).

2. PLASMONICS AND PHOTOELECTROCHEMICAL (PEC) SOLAR WATER SPLITTING

The conversion of solar energy into chemical fuels represents the most promising route for achieving a sustainable energy economy. A photoelectrochemical (PEC) cell for water splitting [77] uses semiconductors to split water into pure hydrogen (H_2) and oxygen (O_2). H_2 is an ideal energy source for transportation, energy storage, and the production of electricity at zero-carbon emission. These properties are attributed to its very high energy density (120 MJ/kg), which is approximately 2.5 times higher than that of traditional fossil fuels such as methane, gasoline, and diesel. H_2 is also essential for ammonia production and as a feedstock for the production of liquid fuels from CO_2 reduction. The overall solar water splitting reaction is endothermic ($\Delta E = 1.23$ V) and consists of two half reactions, i.e., the hydrogen evolution reaction (HER) and the oxygen evolution reaction (OER) which are given by

$$2H_2 0 \rightarrow 2H_2 + O_2 \tag{2.1}$$

$$2H^+ + 2e \rightarrow H_2 \qquad (HER, E_{red}^0 = 0.0\,V\ vs\ RHE) \tag{2.2}$$

$$2H_2O + 4h^+ \rightarrow O_2 + 4H^+ \qquad (OER, E_{ox}^0 = 1.23\,V\ vs\ RHE) \tag{2.3}$$

where the redox potentials are referred with respect to the Reference Hydrogen Electrode (RHE). In a conventional PEC device, the reduction (HER) and oxidation (OER) half reactions occur on the surface of the cathode and anode, respectively, in an aqueous electrolyte, which closes the current circuit between the electrodes. The electrochemical behavior of the photoelectrodes is dictated by their electronic properties and type of mobility, such that n-type semiconductors operate as photoanodes and accordingly p-type as photocathodes [77–80]. Once the photoelectrode is in contact with an electrolyte, a space-charge (depletion) layer is formed at the semiconductor/liquid junction. Photoexcited electron-hole pairs are generated dur-

ing light illumination and become separated due to the space-charge field (i.e., the photovoltage). In the case of a photoanode (photocathode), this electric field drives holes (electrons) toward the interface of the solid electrode and the liquid electrolyte, where they oxidize (reduce) water, thereby generating $O_2(H_2)$. In contrast, the photogenerated electrons (holes) are transferred via the external circuit to a metallic cathode (anode), where they reduce (oxidize) water, thereby generating H_2 (O_2). This category of PEC cells is referred to as Schottky type configuration (Figure 2.1a) and is currently the most frequently investigated configuration. With this architecture, semiconductor candidates for the cathodic or the anodic half-reaction can be separately studied, and eventually coupled either together or with a solar cell to provide the necessary photovoltage to drive water splitting without the application of an external bias voltage.

Materials used for PEC water splitting must have bandgap $E_g \geq 1.23$ V i.e higher than the thermodynamic redox potential as highlighted in Eq. 2.3. They also must have their conduction and valence band edges, E_{CB} and E_{VB} respectively, straddle the water redox potentials E^0_{red} and E^0_{ox} respectively. Actually, due to unavoidable potential losses and kinetic overpotentials, the bandgap of a suitable material should be between 1.6 -2.4 eV to sustain overall water splitting. Besides the semiconductor must also be low cost, have high chemical stability, high carrier mobility, high carrier lifetime and rapid interfacial charge transfer. Figure 2.1b shows the bandgap and band edge positions of several candidate materials that have been investigated for PEC water splitting [81]. As mentioned earlier, only those materials with E_{CB} above E^0_{red} (HER) and E_{VB} below E^0_{ox} (OER) can be used as either the photocathode or photoanode. One should also keep in mind that in contrast to materials for photovoltaics (PV), PEC electrodes (especially photoanodes) undergo severe photocorrosion, due to charge carriers with high oxidation potential at the semiconductor surface. Nevertheless, it is believed that a Solar-to-Hydrogen (STH) efficiency of 10% should be viable for commercialization of PEC solar water splitting [82]. In this regard, record STH efficiency values (10% for Si [83] and 19.3% for GaAs/GaInAs/GaInP/AlInP dual
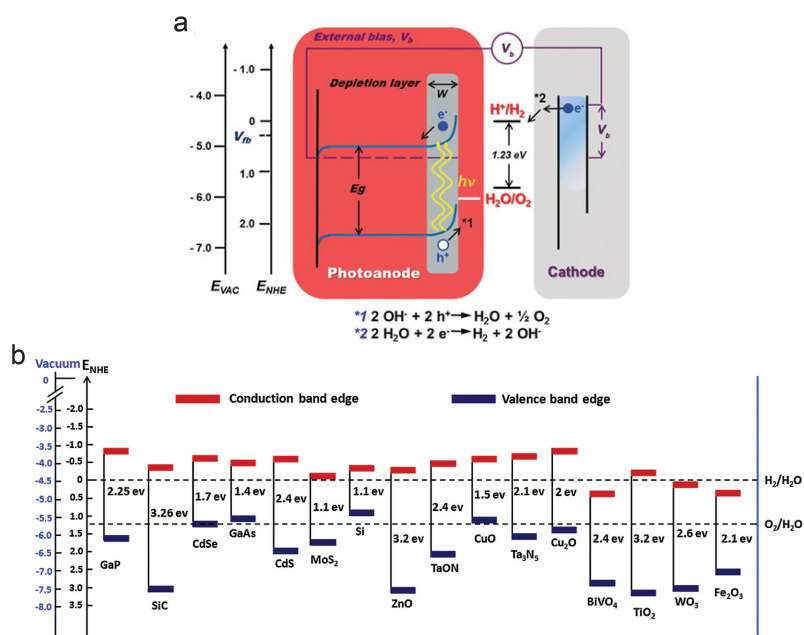
Fig. 2.1. a) Schematic of a Schottky PEC cell showing a photoanode in contact with the electrolyte resulting in the formation of a depletion layer (width: w). The photoanode has a bandgap (E_g), a flat band potential (V_{fb}), and drives the water splitting under an applied bias (V_b). Energy scales are reported both vs. vacuum (E_{VAC}) and the normal hydrogen electrode (E_{NHE}). b)Band edge positions of semiconductors in contact with the aqueous electrolyte at pH = 0 relative to NHE and the vacuum level. For comparison the HER and OER redox potentials are shown by dashed lines.

junction tandem PEC/PV) [84] have been realized, although these materials exhibit low stability (maximum 100 h for Si) [85, 86]. These semiconductors are characterized by large charge mobility, high light absorption and optimal E_g, but are associated with high manufacturing costs. Moreover, their poor stability in PEC conditions prevents long-term device durability. On the other hand, earth-abundant metal oxides (Figure 2.1b), such as TiO_2, α-Fe_2O_3, WO_3, and $BiVO_4$ exhibit outstanding PEC long-term stability and promising efficiency (7.7% for a dual α-Fe_2O_3/$BiVO_4$ photoanode) [87–90], representing a promising option for PEC cells. They are characterized (in general) by low processing cost, high stability (even in harsh environments), low light absorption, low minority carrier diffusion length, and high recombination. These are some drawbacks which need to be addressed before we can think of application of these materials for commercial PEC solar water splitting. While material quality improvement is definitely a path to efficient PEC solar water splitting, enhanced light trapping in the semiconductor is also an effective approach. In order to achieve this, plasmonics has emerged as a powerful approach to improve light collection and thereby overcome the general drawbacks of earth-abundant materials. Several review articles can be found in literature that highlight the progress in plasmon-enhanced PEC water splitting [91–94]. I introduced the concept of a LSPR in the previous chapter. The lifetime of an LSPR resonance can be described as the plasmon dephasing time T_2 which is related to the damping constant Γ by

$$T_2 = \frac{2\hbar}{\Gamma} \tag{2.4}$$

where Γ is related to the electron scattering rate. Figure 2.2 shows the timescales of the different processes related to LSPR decay which are significant for PEC water splitting. As shown in Figure 2.2a, after excitation LSPR decays in 1-20 fs: T_2 values of 5-8 fs and 1.4 fs have been obtained respectively for small (15-20 nm diameter) and "big" (150 nm) Au nanoparticles (NPs), while 100 nm-long nanorods have dephasing times up to 18 fs [95, 96]. The LSPR is associated to a large dipole moment, which can couple to the semiconductor, generating electron-hole pairs in the latter if occurring in a spectral region where the semiconductor absorbs light. This effect
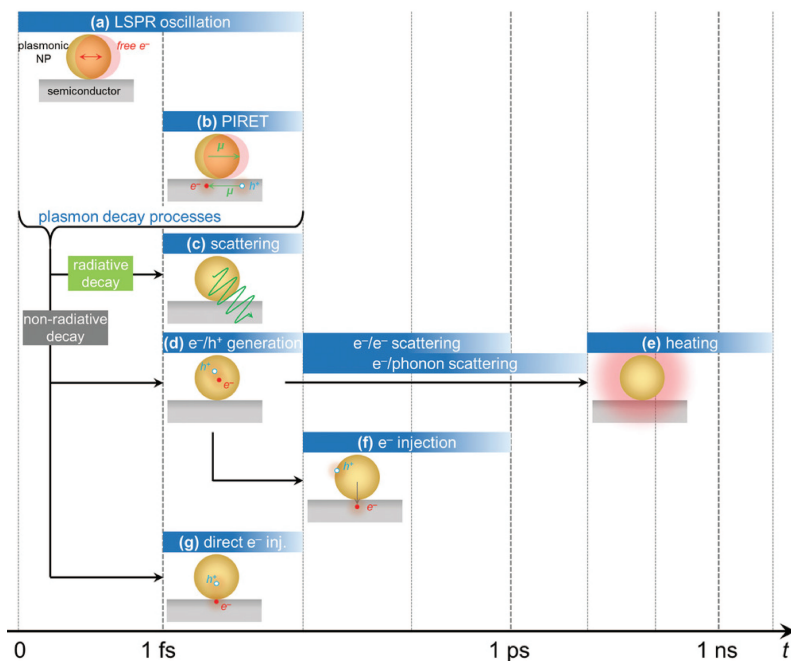
Fig. 2.2. a) The LSPR oscillation and decay in 1-20 fs. b) LSPR coupled to semiconductor for Plasmon Induced Resonance energy Transfer (PIRET). c) Radiative decay of the LSPR d) Non-radiative decay of LSPR leading to hot carrier generation. e) Heating of the plasmonic material as hot electrons lose energy f) Hot carriers can also be injected into the semiconductor (indirect method). g) Direct carrier injection into semiconductor.

is referred to as Plasmon Induced Resonant Energy Transfer (PIRET) [97, 98]. Subsequently, the plasmon resonance may dissipate either radiatively or non-radiatively. Radiative decay occurs via re-emission of photons (scattering) that may increase light absorption in the semiconductor if the plasmon energy is higher than the semiconductor bandgap. Non-radiative decay, also referred to as Landau damping, generates energetic electron-hole pairs (with a non-thermal distribution) in the metal. These hot carriers rapidly relax to a thermal (Fermi-Dirac) distribution via electron-electron scattering, with a characteristic time of $\tau_{el} \sim$100 fs-1 ps [99–104]. The resulting effective electron temperature equilibrates with the lattice by electron-phonon scattering in $\tau_{ph} \sim$1–10 ps [103, 104]. This process results in heating of the plasmonic material, which finally cools through heat transfer to the surrounding medium in 100 ps–10 ns, depending on the material, the particle size and the thermal conductivity of the environment [70, 105]. In particular, heat generation is associated with Ohmic losses and is proportional to $\varepsilon(\omega) \mid E_{in} \mid^2$, where E_{in} is the electric field inside the material [106]. This heat can lead to a temperature rise of tens-of-hundreds of degrees depending on the incident power and the particular plasmonic excitation [75, 76]. Alternatively, prior to their relaxation, hot charge carriers can be extracted from the plasmonic material and injected into the semiconductor. This process is referred to as hot electron (hole) injection and must occur within 1 ps from plasmon generation, in order to compete against electron-electron and electron-phonon scattering. This process is also referred to as indirect electron transfer, as recently a so-called direct electron injection process has been reported where hot electrons (holes) are directly generated in the conduction (valence) band of an n-type (p-type) semiconductor in contact with the plasmonic material. This process occurs in 20–50 fs and is therefore characterized by substantially faster dynamics than the indirect mechanism [107–110]. In both the direct and indirect processes, the interest in PEC water splitting resides in the possibility of generating additional charge carriers through the plasmonic unit, with energies lower than the bandgap. In the following sections, I will go over some established literature on scattering and hot electron injection mechanisms for PEC

solar water splitting. These two methods will be relevant to my research work that I will outline in Chapter 3. These sections are borrowed from the review paper that I published with our collaborator Dr. Alberto Naldoni and his colleagues [111]. For a detailed overview on the other methods for plasmon-enhanced PEC water splitting, I would encourage the curious reader to go through our entire review paper.

2.1   Scattering effects in plasmon-enhanced PEC water splitting

Figure 2.3a shows a schematic of the scattering effect, originating from the radiative decay of a LSPR. Symmetrical photon emission occurs when the plasmonic NPs are embedded in a homogeneous medium, while it is preferentially directed toward the material with the highest refractive index n for NPs close to an interface between different media [115]. This holds for aqueous electrolytes (n~1.3) in contact with typical semiconductors used for water splitting (n~2.6 for TiO_2 and n~2.9 for α-Fe_2O_3). Thus, a sort of antireflection layer can be obtained by placing plasmonic NPs at the electrolyte/semiconductor interface. Moreover, in the case of several closely spaced NPs, multiple scattering events can occur, leading to a substantial increase in the light pathway within the semiconductor, similar to that reported for solar cells [116]. Valenti et al. reported a scattering effect for 65 nm Ag NPs on top of 100 nm-thick $BiVO_4$ photoanodes [112]. As shown in Figure 2.3b, at energies higher than the bandgap, the absorption of the composite material was moderately higher than that of bare $BiVO_4$. This is due to a radiative plasmon decay by scattering. The Incident Photon Conversion Efficiency or IPCE spectra of the pristine and Ag NP-decorated films were measured with a hole scavenger (i.e., H_2O_2) with back-illumination (Figure 2.3c). This analysis revealed that in H_2O_2 the NPs yielded a relatively small increase in the photoactivity, which was attributed to scattering effects. The larger IPCE enhancement in the absence of the hole scavenger, conversely, was related to catalytic effects of Ag NPs [117]. A higher IPCE increase (~6%) could be obtained by front illumination. Zhang et al. also combined Au NPs with $BiVO_4$
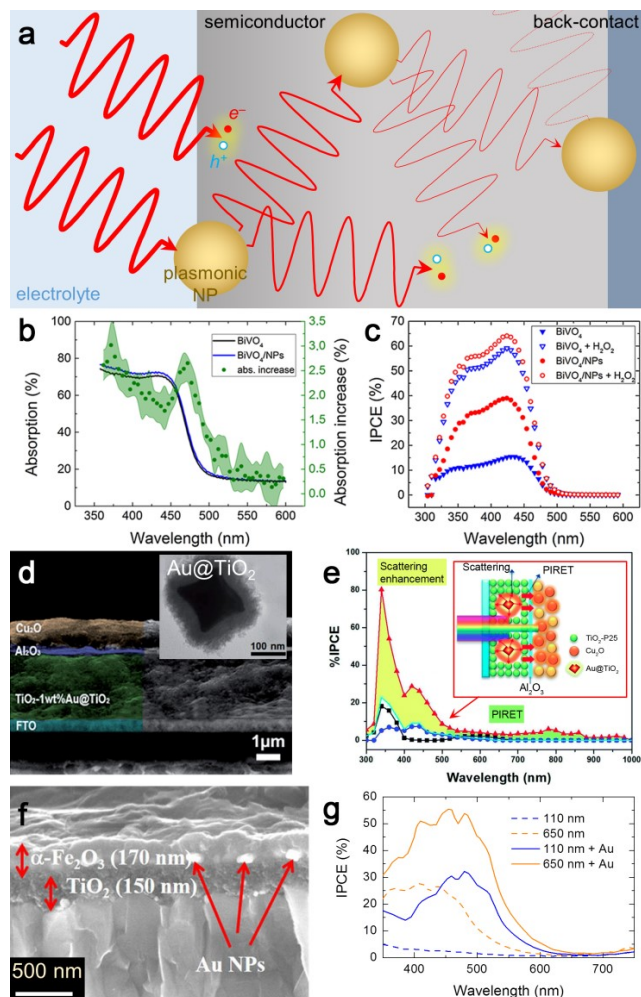
Fig. 2.3. a) Schematic of the plasmonic scattering effect in semiconductor photoelectrodes. b) Absorption increase in BiVO$_4$ decorated with 65 nm Au NPs under back illumination. c) IPCE measurements of BiVO$_4$ photoanodes with/without Au NPs and with/without H$_2$O$_2$ as a hole scavenger in the electrolyte solution. d) SEM image of TiO$_2$-Au@TiO$_2$/Al$_2$O$_3$/Cu$_2$O photoelectrode on FTO substrate (inset: TEM image of an individual Au@TiO$_2$ unit). e) IPCE spectrum of the composite photoelectrode in d) (red triangles) compared with the spectra of TiO$_2$-Au@TiO$_2$ (black squares), Cu$_2$O (blue circles), and TiO$_2$/Cu$_2$O (light-blue line). The inset shows schematics of the proposed enhancement mechanism. f) SEM image of α-Fe$_2$O$_3$ photoanode with Au NPs at the interface with a TiO$_2$ layer underneath. g) IPCE spectra of α-Fe$_2$O$_3$ photoanodes (thicknesses: 110 nm and 650 nm) with or without Au NPs (b,c taken from [112]; d,e taken from [113]; f,g taken from [114]).

and studied the size-dependent plasmonic effects through PEC characterizations and finite-difference time-domain (FDTD) simulations [118]. In particular, the scattering effect was predominant for Au NPs larger than 60 nm, while FDTD simulations suggested that PIRET occurred for smaller NPs ($\leq$40 nm). Scattering and PIRET were also reported for a heterojunction photoelectrode composed of p-type Cu_2O and n-type TiO_2 that was loaded with 1 wt.% Au@TiO_2 core-shell NPs with different Au-core sizes (37–120 nm) [113]. Figure 2.3d shows a SEM micrograph of the device, which also included an insulating Al_2O_3 layer between TiO_2 and Cu_2O for improved interfacial charge separation. The cathodic photocurrent generated by the photo-electrodes increased gradually with increasing Au particle size, reaching a maximum value of -4.34 mA/cm^2, which is almost 20 times higher than that of the TiO_2/Cu_2O photoelectrode. Figure 2.3e shows IPCE measurements confirm that the maximum performance was achieved with 120 nm NPs. This enhancement was attributed to scattering (in the UV range) as well as PIRET effects (visible-NIR range) depending on the incident wavelength. Archana et al. reported scattering and catalytic effects from Au NPs ($\sim$80 nm diameter) embedded at the α-Fe_2O_3/TiO_2 layer interface of composite photoanodes (Figure 2.3f) [114]. The LSPR of Au NPs occurred at $\sim$600–700 nm and the IPCE of films with different α-Fe_2O_3 thicknesses (110 and 650 nm) increased at wavelengths below 600 nm, i.e., in the spectral region of the semiconductor absorption (Figure 2.3g). In particular, the inclusion of Au NPs led to a stronger enhancement for the thinner film. This was ascribed to a stronger scattering effect as, compared with the thicker film, the Au NPs could better interact with light.

2.2   Hot carrier effects in plasmon-enhanced PEC water splitting

Hot electron injection may be either direct or indirect and is one of the most widely investigated plasmonic mechanisms for enhancing the efficiency of PEC water splitting. This mechanism enables the use of visible and near infrared (NIR) pho-
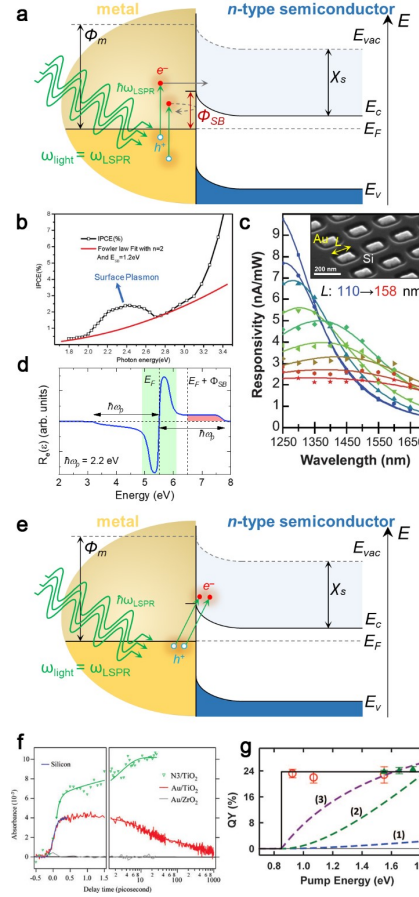
Fig. 2.4. a) Schematics of indirect hot electron injection from a plasmonic metal to an n-type semiconductor (E_{vac}: vacuum energy; E_F: Fermi level; ϕ_m: work function of the metal; χ_s: electron affinity of the semiconductor; ϕ_{SB}: Schottky barrier). b) IPCE of a plasmonic Au/TiO2 diode [119]. c) Experimental photocurrent of Au nanoantennas/Si diodes for different antenna lengths (points); solid lines represent the fit of Eq. 2.7 to the data for $\phi_{SB} = 0.5$ eV [120]. d) Typical spectrum showing the rate of electron generation in a localized plasmon wave in a metal nanocube. Two types of excited intraband carriers can be observed: Drude (green region) and hot carriers (red region) [121]. e) Schematic of direct hot electron injection from a plasmonic metal to an n-type semiconductor. f) Transient absorption kinetics at 3500 nm of nanocrystalline films (green: N_3/TiO_2; red: Au/TiO_2; grey: Au/ZrO_2). The blue line shows the response of the apparatus obtained using a Si plate [107]. g) Measured quantum yield of direct electron injection in quantum dots (red open circles: PbS; green triangles: Cd_3P_2) and yield predicted from three different variations of Fowler's equation (dashed lines) [110].

tons that are not absorbed by wide-bandgap semiconductors typically employed as photoelectrodes.

2.2.1 Indirect mechanism

When a Schottky barrier is formed at a metal/semiconductor interface (Figure 2.4a), the barrier height (ϕ_{SB}) can be roughly evaluated with the Schottky-Mott rule [122, 123] as

$$\phi_{SB} = \phi_m - \chi_s \tag{2.5}$$

where ϕ_m is the work function of the metal and χ_s is the electron affinity of the semi-conductor. This simple rule neglects other parameters, such as structural/electronic inhomogeneity, quantum tunneling and interfacial chemical effects, that may lower ϕ_{SB} [124, 125]. The indirect mechanism for hot electron transfer (Figure 2.4a) is composed of three elementary steps: (i) hot electron generation in the metal upon plasmon decay, (ii) electron transport to the interface with the semiconductor, and (iii) the transfer of those with energy higher than ϕ_{SB} to the semiconductor conduction band [120, 126]. Hot electron injection is not peculiar of plasmonics, it is the working mechanism of Schottky diodes [127]. The photocurrent in the diode can be expressed in terms of Fowler's law as [128]

$$I = c\frac{h\nu - \phi_{SB}}{h\nu} \tag{2.6}$$

where c is a constant and $h\nu$ is the photon energy. The value of ϕ_{SB} can be determined by fitting the experimental photocurrent with Eq. 2.6, and compare it with that determined from Eq. 2.5. For plasmonic metals in contact with semiconductors, a deviation from Fowler's law exists due to the plasmon resonance which is shown in Figure 2.4b for an Au/TiO$_2$ diode [57]. This law can then be modified in order to determine the photocurrent in the plasmonic diode (I_{plasm}) [120]. The modified law is given by

$$I_{plasm} = I.A \tag{2.7}$$

where A is the plasmon absorption spectrum. This is illustrated in Figure 2.4c for Au/Si diodes where Au is in the form of nanorods [120]. The generation of hot carriers has been theoretically modeled by several groups using different degrees of approximation [121, 129–135]. For example, Govorov and co-workers formulated a quantum theory for plasmonic hot carriers generation and injection under optical excitation [121, 129, 130]. Figure 2.4d shows an example of a non-equilibrium distribution of charge carriers in a localized plasmon wave in a metal nanostructure [121]. Most electrons and holes are generated with an energy close to the Fermi level (Drude carriers), while higher energy charge carriers (hot) are also present and are formed by quantum optical transitions near the surfaces, which in turn can occur due to the breaking of linear momentum conservation. The ratio between the generation rates of hot and Drude carriers is proportional to $\frac{1}{d^2}$, where d is the NP diameter [136]. Thus, the likelihood of hot electron injection into a semiconductor increases with decreasing size of the NP. The generation rate of high-energy electrons capable of crossing the Schottky barrier is given by [137]

$$Rate_{high-E} = \frac{2}{\pi^2} \frac{e^2 E_F^2}{\hbar} \frac{\hbar\omega - \phi_{SB}}{(\hbar\omega)^4} \int S| E_{norm}(\theta, \phi) |^2 ds \qquad (2.8)$$

where E_F is the Fermi level of the metal and $E_{norm}(\theta, \phi)$ is the normal component of the electric field near the NP surface. It is to be noted that Atwater and co-workers have reported a non-symmetrical energy distribution of hot carriers for Au and Cu, where, compared to hot electrons, a higher fraction of hot holes was located farther from E_F [131, 132].

2.2.2 Direct Mechanism

Figure 2.4e shows a schematic of the direct hot electron injection for a metal/n-type semiconductor. In contrast to the indirect mechanism, the LSPR decays providing the direct generation of hot electrons in the semiconductor conduction band and leaving hot holes in the metal, respectively, without any intermediate step. The direct mechanism has been theoretically proposed by Prezhdo [109] for a Au_{20} clus-

ter on TiO_2, where a considerable delocalization of the plasmon on TiO_2 and a high probability (50%) of direct electron localization in the TiO_2 conduction band occur 40 fs after optical excitation. The aim of the model was to find a theoretical basis for the experimental results reported by Furube et al., [107] who observed that an electron transfer in Au/TiO_2 occurred in $\leq$240 fs as shown in Figure 2.4f. A follow-up study on Au/TiO_2 found that the electron injection was complete in 50 fs, with an efficiency of 20–50%, depending on the TiO_2 particle size [108]. However, in 2015 Wu et al. investigated colloidal CdSe nanorods functionalized with Au NPs and reported the first clear experimental evidence pointing to the existence of the direct pathway [110]. They found that an ultrafast electron transfer from Au to CdSe occurred within 20$\pm$10 fs and obtained a quantum yield of 24% independent of the pump energy (Figure 2.4g). However, theoretical curves calculated from Fowler's equation are inconsistent with experimental data (details provided in Figure 2.4). As plasmon decay directly excited an electron from Au to CdSe, the quantum yield was independent of the excess energy of the electron above the conduction band edge. In 2017, Tan et al. measured a hot electron transfer from Ag NPs (4 nm diameter) on TiO_2 occurring in $\leq$10 fs [138]. The direct mechanism has recently been identified, but a systematic study on indirect vs. direct pathways in PEC water splitting experiments still remains to be performed. At this point, I will draw an end to the discussion on plasmon-induced mechanism for PEC water splitting. There are several other mechanisms through which plasmons can be beneficial to PEC water splitting. However, the two mechanisms that I overviewed in this chapter will be the major players in my experiments that I will describe in Chapter 3. As mentioned before, a detailed overview of the other plasmon-induced phenomenon in PEC water splitting can be found in [111].

3. GAP PLASMON ENHANCED PEC SOLAR WATER SPLITTING

For my research, the material choice for PEC water splitting was α-Fe$_2$O$_3$ or hematite. It is one of the more rigorously studied semiconductor material for PEC water splitting. It is an earth abundant, non-toxic and photochemically stable semiconductor. The progress made in PEC water splitting with hematite is outlined in several review articles [81, 139, 140].

Hematite has a band gap of 2.0-2.2 eV which is ideally suited for PEC water splitting [141]. It is to be noted that the position of hematite's band edges only allow us to use it as the photoanode for oxygen production half-reaction. The maximum theoretical solar energy conversion efficiency for hematite is 14-16% [142]. However, the reported Solar-to-Hydrogen (STH) efficiency of hematite is very low mainly due to the short excited state lifetime (<10ps) [143, 144] and the short hole diffusion length of 2-4 nm [145, 146]. The majority of photoexcited electrons are lost in hematite through electron-hole recombination processes within the first few picoseconds and only holes close to the semiconductor electrolyte interface contribute to the oxygen evolution reaction. Furthermore, hematite is an indirect bandgap material, and it requires a relatively thick layer of material for total solar absorption. This competes with the small hole diffusion lengths which calls for a thin layer. Poor electrical conductivity of hematite also limits charge transport in the material [147]. This can however be overcome by elemental doping. Reports of Si [148] and Ti [149] doping in hematite to increase photo current from water oxidation can be found in literature. These dopants can significantly increase the photocurrent and reduce the photocurrent onset potential. Si doping can result in photocurrents of around 2.2mA/cm^2 at 1.23 V vs RHE as reported in [150]. Ti doping can cause a negative offset of 0.2V of the onset photocurrent potential as per [151]. The slow kinetics of

water oxidation at the hematite surface is also a cause for the low solar conversion efficiency of hematite. Surface catalysts such as IrO_2 can significantly enhance the photocurrent [152]. One of the possible ways to improve oxidation photocurrent and address the trade-off between light absorption and hole diffusion length is to use resonant nanostructures to enhance the light collection efficiency of the active hematite layer. It has already been shown that optical Mie resonances and guided modes in a nanostructured hematite layer can enhance the photocurrent by three times [153]. As described in the previous chapter, plasmonics can also be used to efficiently trap light inside the active layer for PEC water splitting. Over an order of magnitude enhancement in photocurrent from hematite nanorods due to plasmon-induced light trapping from a gold nanohole array has recently been reported [154]. Several other works also report on plasmon-enhanced photocatalytic water splitting with hematite [155–157].

In my research, I focused on plasmon-assisted oxidation photocurrent enhancement in ultrathin ($\sim$10-20 nm) hematite films. Since hematite has a very low hole diffusion length, it is preferable to use thin films with enhanced absorption to harvest the maximum possible solar energy for water splitting. The enhancement reported in this work is due to plasmon resonances and optical scattering in a gold antenna-hematite-gold sandwich structure. Such a metal-insulator-metal configuration is called a continuous layer gap plasmon resonator [158]. Gap plasmon resonators have been studied for plasmon enhanced water splitting before [159]. These plasmonic structures are characterized by high field confinement in the middle insulator upon illumination with electromagnetic waves. Here we design a gold-based plasmonic hematite photoelectrode which shows approximately two-fold enhancement above and six-fold enhancement in oxidation photocurrent below the hematite bandgap. The below bandgap enhancement is possibly to be due to the generation of hot electrons from plasmon decay while the above bandgap enhancement is due to off-resonant scattering from the top gold antenna and gold back-mirror. This work has been performed

in collaboration with Dr. Alberto Naldoni and his colleagues. The work has been published in [160] and most of this chapter is from that particular publication.

3.1 Material Growth, Characterization and Fabrication

The hematite films were grown using Pulsed Laser Deposition (PLD). Figure 3.1a shows a detailed flowchart of the fabrication process. First, a 200 nm thick gold layer was deposited on Si (100) substrate with a 6 nm thick Al_2O_3 adhesion layer. Then a 15 nm thick layer of hematite was deposited using a commercially available 99.9% pure Fe_2O_3 target. The hematite growth temperature was around 500 °C in a 30 mTorr O_2 ambient and the PLD had a 1.5-2 J/cm^2 laser fluence. Gold nanodisks were fabricated on top of the hematite with e-beam lithography and lift-off using PMMA. First PMMA was spin coated on the hematite at 4000 rpm for 60 secs. Then the sample was soft baked at 180 °C for 3 mins. The nanodisk arrays were defined using an e-beam writer. The PMMA was then developed using 1:3 MIBK:IPA solution for 50 secs and rinsed afterwards in IPA for 30 secs. Finally, the gold nanodisks, 50 nm height, were deposited on the sample using e-beam evaporation followed by PMMA removal with acetone. Figure 3.1b shows a schematic of the fabricated sample that contained four arrays of gold nanostructures with various diameters and array periods. The structures support gap plasmon resonances which are used to enhance the light trapping and oxidation photocurrent in thin hematite films. Raman analysis was used to identify phase of hematite grown with PLD. Figure 3.2a shows the Raman spectra. The spectrum was collected using a DXR Raman spectroscope (Thermo Scientific, U.S.A.) with a laser at 633 nm. A total of eight vibration modes were detected in the hematite samples grown with PLD. We associate the peaks at 224, 242, 297 cm^{-1} with the motion of iron cations, while those at 408, 491 and 610 cm^{-1} are associated to the motion of oxygen anions [161]. In nanocrystalline hematite, a peak at approximately 660 cm^{-1} is further detected, owing to the lack of long-range order. Figure 3.2b shows the High Resolution Transmission Electron Microscope (HRTEM)
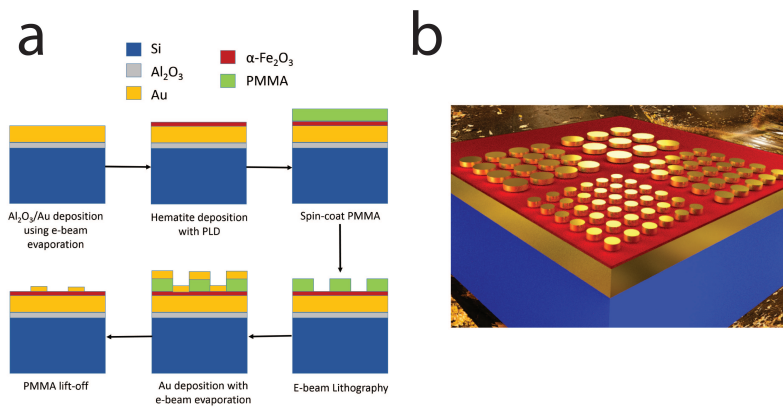
Fig. 3.1. a) Flowchart showing the fabrication steps for realizing gold-hematite gap-plasmon electrode. b) Schematic representation of gap-plasmon array of different nanodisk diameters and periods on top of hematite-gold. (Blue-Silicon, Yellow-Gold and Red-Hematite).

image of the sample. The inset of Figure 3.2b shows the Selected Area Electron Diffraction (SAED) pattern for the hematite flake. Two crystal planes namely the (110) and (006) can be easily seen. The area chosen for SAED image collection is shown in red along with the lattice constants for the (110) and (006) planes. From the Raman and TEM data, we can conclude that the PLD grown hematite films were polycrystalline in nature. For more details on the Raman and TEM measurements, I would encourage the reader to look at our publication [160].

Figure 3.3a shows the SEM images of the fabricated gold nanodisks on hematite. Four different nanodisk diameters (D) and nanodisk pitch sizes (P) were fabricated. These diameter-pitch or D-P combinations were 100-200, 125-200, 150-300 and 200-300 in nanometers. All fabricated nanodisks show minimum amount of gold flakes, which is a common feature of e-beam lift-off with single layer PMMA. Removing the flakes requires the use of more complex bi-layer PMMA e-beam lithography which was not used in the current fabrication. Figure 3.3b shows the absorption spectra of all the nanodisk arrays. Figure 3.3b also shows the absorption measured from a bare hematite film on gold for comparison purposes. The two arrays with 200 nm period and 100 nm and 125 nm nanodisk diameters show absorption peaks at 820 nm and 970 nm wavelength respectively. These correspond to the excitation of gap plasmon resonances as will be discussed later. The two arrays with 300nm period and disk diameters 150 nm and 200 nm show absorption peaks at 1120 nm, for the former, and 730 nm and 1550 nm, for the latter. The peak at 1100 nm for the nanodisk with 150 nm diameter and at 1550 nm for the 200 nm diameter nanodisk are gap plasmon resonances. The absorption peak at 730 nm for the 200 nm diameter nanodisk is a higher order gap plasmon resonance (see Discussion section later in the chapter). Figure 3.3c shows the simulated absorption spectra for all the nanodisk arrays. For all cases, experiment and simulations, the illumination was with p polarized light at an angle of 20°. Simulations were performed with a finite element method using the commercially available software COMSOL.
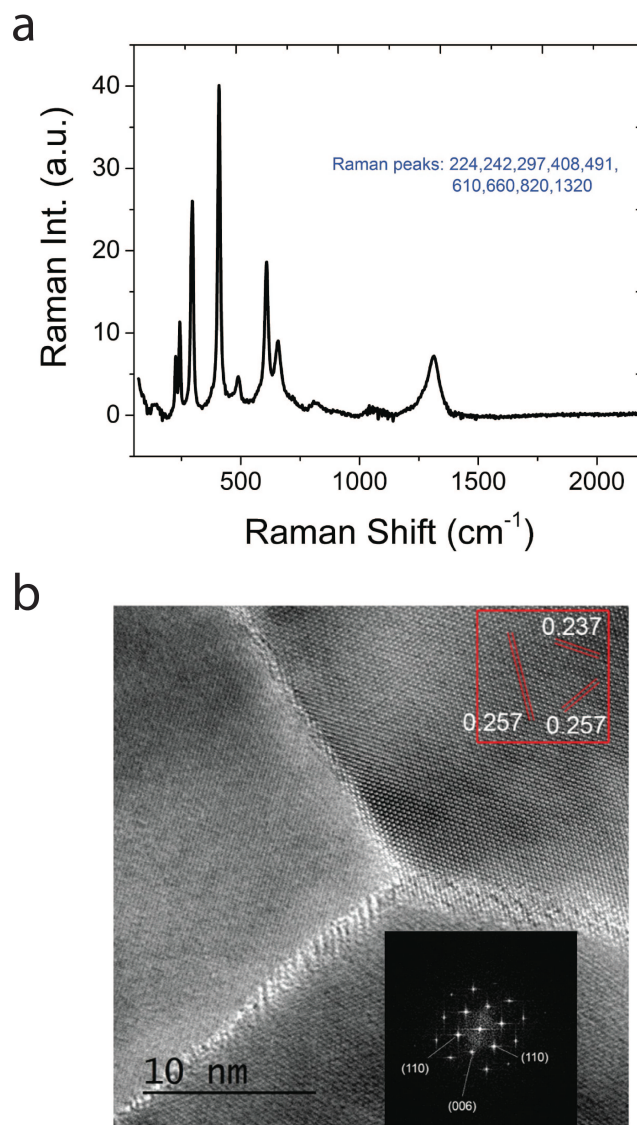
Fig. 3.2. a) Raman spectroscopy data measured from the hematite films grown on gold with pulsed laser deposition. Inset lists the position of the Raman peaks in cm^{-1}. b) High Resolution TEM image of the hematite thin film on gold. The SAED (Selected Area Electron Diffraction) image is shown in the inset. The red box highlights the area chosen for SAED. The inter-plane distances between the (110) and (006) planes are also stated in the red box.
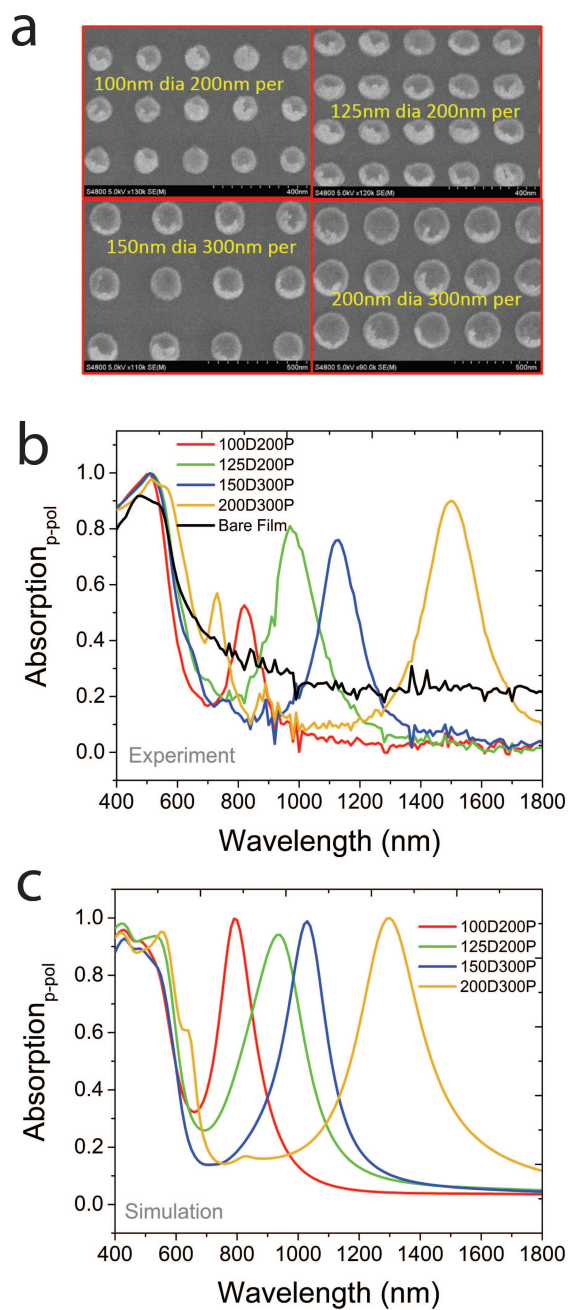
Fig. 3.3. a) SEM image of the fabricated Au nanodisks for gap plasmon array with four different disk diameters. b) Experimentally measured absorption spectra by using p polarized light at 20° incidence for all the arrays. Measured absorption of the bare hematite film on gold is also shown. c) Simulated absorption spectra by using p polarized light at 20° incidence for all the arrays. D: diameter of the nanodisk and P: Period of the array in nanometers
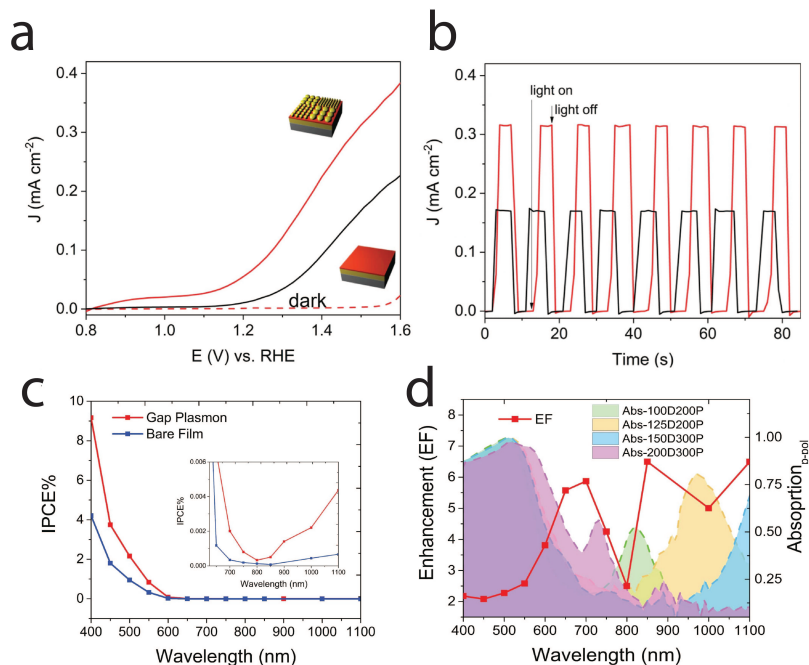
Fig. 3.4. a) Cyclic voltammetry measurement with a 3 electrode PEC cell for gold-hematite gap plasmon and bare hematite films. (Red curve: Gap plasmon, Black: bare Film, Red dash: dark current). b) Chopped photocurrent measured at 1.5 V vs. RHE for the two samples. The photocurrent from gap plasmon resonators is almost 2 times that one of bare flat hematite electrode. c) Incident Photon Conversion Efficiency (IPCE) for the gap plasmon electrode and bare hematite electrode at 1.5V vs. RHE of applied bias. Inset: IPCE in the near IR wavelengths. d) Enhancement Factor (EF) of the IPCE for the gap plasmon electrode with all four arrays of nanostructures and a bare film. Above the hematite bandgap, the gap plasmon electrode has approximately double the efficiency of the bare electrode. Below the bandgap the efficiency increase is up to six/seven-fold. The experimentally measured absorption plots for the four different arrays are also shown. We see a complex, oscillating behavior for the EF in the IR spectral region where the plasmonic resonance are located.

3.2   Experiment

The gap-plasmon electrode was tested in a three electrode PEC setup. The gap-plasmon electrode had all the four different arrays of nanodisks described above, with each array being a 500 μm x 500 μm square. Furthermore, every array of a particular

nanodisk diameter and pitch was replicated four times so as to give us as much of a large area coverage as is possible to fabricate within a reasonable timeframe. A bare hematite film electrode was also measured for comparison purposes. The three–electrode PEC cell had a silver chloride electrode (Ag/AgCl/Sat. KCl) as the reference electrode, while a high surface area Pt mesh was the counter electrode. The potential (E) was referred to the RHE scaled through the Nernst equation:

$$E_{RHE} = E_{AgCl} + 0.197\,V + 0.059\,pH \tag{3.1}$$

where E_{AgCl} is the measured electrode potential vs. the used reference electrode and 0.197 V is the reference electrode standard potential vs. RHE. In the manuscript, all measurements are reported with respect to RHE. The measurements were carried out in 1 M NaOH aqueous solution at pH 13.6. Linear sweep voltammetry curves were measured at a scan rate of 10 mV/s. PEC measurements were made with a PGSTAT204 Autolab potentiostat. At least three electrodes of each type were fabricated and tested. All electrodes showed similar characteristics. Figure 3.4a shows the results of the measured photocurrent with the PEC cell. The red curve corresponds to the photocurrent measured for the gap plasmon electrode whereas the black curve is the photocurrent measured for a bare hematite film on gold. The red dashed curve is the dark current which is negligible. It can be seen that the gap plasmon electrode shows about twice the photocurrent compared to the bare hematite film at 1.23 V vs RHE. There is also a cathodic shift of approximately 0.4 V in the onset potential for the gap plasmon electrode. This can be due to catalytic effect of gold nanodisks. I will discuss more on this later.

Figure 3.4b shows the chopped photocurrent measurements performed at 1.5 V vs. RHE on the gap plasmon (red curve) and bare hematite (black curve) electrode. Once again, the gap plasmon electrode shows twice the photocurrent compared to the bare film. The increase and decrease of photocurrent with the switching on and off of the incident light clearly demonstrates that the solar driven photocatalysis is the dominant response of both the electrodes. That gold nanodisks have a catalytic

influence on the photocurrent due to better charge separation in the space charge layer has already been reported in literature. This effect has been shown to contribute to photocurrent on top of plasmon-induced enhancement [162, 163]. The cathodic shift of the onset potential for the gap plasmon electrode is attributed to catalytic effects of the gold nanodisk. However to better understand the influence of this catalytic effect, we conducted Electrochemical Impedance Spectroscopy (EIS) on the gap plasmon and bare film electrode. The gap plasmon electrode showed a 20% reduction in the charge transfer resistance compared to the bare film electrode. This means that the gap plasmon electrode has a better separation of the generated charge carriers which would lead to some enhancement in the measured photocurrent compared to the bare film electrode. Nevertheless, this increase in charge separation capability is not sufficient to explain the doubling of the measured photocurrent for the gap plasmon electrode which I will discuss now.

To better understand the photocurrent enhancement in the gap plasmon electrode, chronoamperometry measurements at 1.5 V of applied bias were performed on both the electrodes. Figure 3.4c plots the Incident Photon Conversion Efficiency (IPCE) as obtained from measurements. IPCE is calculated as

$$IPCE = \frac{J_{meas} * 1240 * 100}{\lambda * I_0} \tag{3.2}$$

where J_{meas} is the measured photocurrent at wavelength λ of incident intensity I_0. From Figure 3.4c it is clearly seen that the gap plasmon electrode has approximately double the efficiency compared to the bare hematite electrode, especially until 600 nm, i.e. above the hematite band gap. This can be due to off-resonant light scattering by the gold nanodisks and light reflection from the gold back-mirror. I will provide more details on this in the Discussion section. The inset of Figure 3.4c shows a zoomed-in version of the IPCE plot at the visible (red)-to-infrared wavelengths. Figure 3.4d

shows the Enhancement Factor (EF) in the IPCE as a function of the wavelength. The Enhancement Factor is calculated as

$$EF = \frac{IPCE_{GPE}}{IPCE_{BFE}} \tag{3.3}$$

where $IPCE_{GPE}$ stands for the IPCE of the gap plasmon electrode and $IPCE_{BFE}$ stands for the IPCE of the bare film electrode. Around 1 μm wavelength the gap-plasmon electrode shows six-fold enhancement in oxidation photocurrent compared to the bare hematite electrode. This enhancement is possibly due to plasmon decay and hot hole generation. As explained in the last chapter, plasmons can decay and result in the generation of hot carriers. As shown in Figure 3.4d, the gap-plasmon resonator electrode supports plasmon modes at the infrared wavelengths. Also, recently it has been reported that Au nanoparticles are very suitable for hot hole generation [164]. As Figure 3.4d shows qualitative agreement between the plasmon absorption peaks of the different nanodisk arrays and the measured EF at the near-IR wavelengths, I think in the sub bandgap region of hematite we are witnessing a plasmon generated hot hole induced enhanced photoactivity.

3.3   Discussion

Figure 3.5a shows the optical constants of the 15 nm thick hematite film as obtained from Variable Angle Spectroscopic Ellipsometry. These are the optical constants used for simulation of the gap plasmon resonators, the result for which I presented in Figure 3.3c. Figure 3.5b shows the AFM measurement results on the hematite films. As can be seen, the films are pretty rough and given their small thickness, I believe there exists some discrepancy between the optical constants shown in Figure 3.5a vs. the true permittivity of the hematite films. This is perhaps the main reason why there is a discrepancy between the gap plasmon resonance peaks in experiments and simulations. Moreover, the hematite layer was deposited at a high temperature at which, underlying gold may not be stable. Therefore, the properties
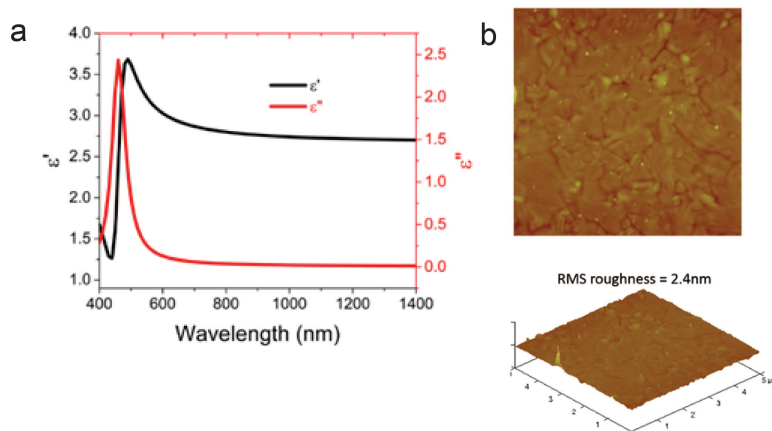
Fig. 3.5. a) Optical permittivity of the hematite film as extracted from Variable Angle Spectroscopic Ellipsometry. b) top-AFM scan of a hematite film on gold; bottom- Section view of the film topology which gives an RMS roughness of 2.4 nm

of gold could be modified, and, in addition, the gold-hematite top boundary may not be perfectly flat as is considered in simulations.

Figure 3.6a and b shows the electric field map for the nanodisk arrays that were fabricated, at the position of the respective gap plasmon resonances. The high field enhancement in the sandwiched hematite layer can clearly be seen, a feature characteristic of gap plasmons. Figure 3.6b shows the maximum field enhancement in the hematite layer for the nanodisk arrays compared to a bare hematite film at above hematite bandgap wavelengths. I believe that it is this enhancement that results in an increase in the IPCE for the gap plasmon electrode at above bandgap wavelengths as shown in Figure 3.4c.

In summary, in this chapter I have demonstrated plasmon-assisted photocurrent enhancement in ultrathin hematite films. The hematite films were grown with pulsed laser deposition on a gold film on Si. A gap-plasmon-based gold-hematite-gold structure was used to achieve the photocurrent enhancement. Our measurements show a two-fold enhancement in photocurrent above the hematite bandgap which is mainly attributed to the enhanced scattering by the gold nanodisks and back reflection from
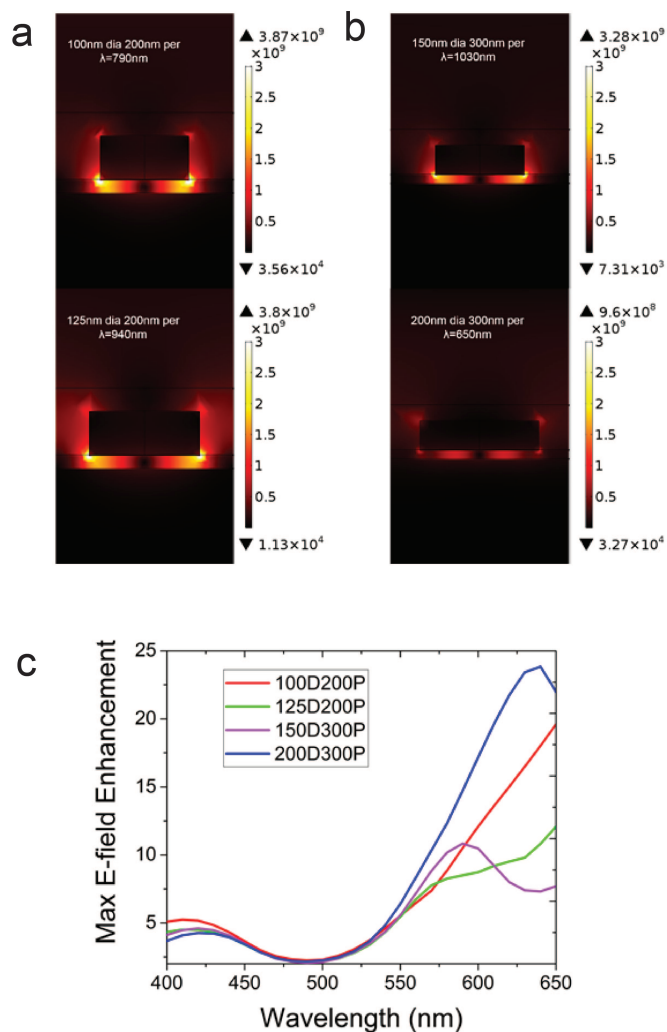
Fig. 3.6. Electric field intensity map for nanodisks with a) 200nm pitch and b) 300nm pitch with two different diameters for each pitch. The field maps are taken at the resonant wavelength corresponding to the absorption peaks in the simulated plots of Figure 3.3c. Gap plasmon resonances leading to high field intensity in the hematite layer can be clearly seen. c) Plot of enhancement of the maximum electric field intensity vs. incident wavelength in the hematite layers for the different arrays compared to a bare film. The simulated enhancement in the above bandgap region is attributed to scattering from the nanodisks and back reflection from the gold mirror. This is believed to lead to the above bandgap photocurrent enhancement observed in experiments. (D:Diameter P:Period in nanometers).

the gold mirror. Below the bandgap, we also observe a wavelength dependent enhancement in the hematite photocurrent. This is attributed to plasmon decay and subsequent hot hole generation, which contributed to the photocurrent measured at near IR wavelengths. These results provide a possible path to enhance the light trapping and photocatalytic response in ultrathin hematite films, thereby addressing the challenging trade-off of small carrier diffusion length and low light absorption. To the best of my knowledge, this is the first time that a gap plasmon based design has been used to achieve this effect experimentally in hematite films. Improvement in hematite film growth by using different back metals such as Pt is believed to lead to further increase in oxidation photocurrent. Also, by using designs of different plasmonic materials and/or nanostructure geometry and shape, it should also be possible to shift the plasmon resonance into the visible above the hematite bandgap. This should lead to even greater enhancement in photocurrent due to increased interband excitation of charge carriers.

4. OPTICS AND MAGNETIC MEMORY DEVICES

Just like light, magnetism has a long history dating back to 600 B.C. Ancient Greek anecdotes speak of materials that attract and repel each other as well as iron, well before the time of Christ. However, it would be almost two millenia before the world would witness the use of magnets for scientific and engineering purposes. The 16th century in Europe saw the advent of the compass for maritime navigation after William Gilbert realized that the Earth itself was a weak magnet. Then, during the 18th and 19th centuries, Carl Freidrich Gauss and Charles Coulomb performed a lot of theoretical and experimental studies on magnetism. In the 19th century, Hans Christian Øersted suggested that electricity and magnetism were in fact linked to each other. His ideas were shortly experimentally verified by André-Marie Ampère and Michael Faraday. It was James Clerk Maxwell who developed a comprehensive theoretical foundations of the physics of electromagnetism in the 19th century. The beginning of the 20th century witnessed the birth of quantum mechanics, which was a paradigm shift compared to the laws of classical mechanics that scientists have been familiar with up to that point. Based on this new understanding of nature, the theory explaining magnetism in materials (called quantum electrodynamics) was developed by two German scientists Ernest Ising and Werner Hiesenberg.

Magnetic materials are actually made up of small domains each of which have their own magnetic dipole moment i.e. each domain acts as a smaller magnet. The overall magnetic moment of the magnet ($\mathbf{M}$) is the vector sum of the moment of its individual domains. The orientation of the magnetic moment, say parallel of anti-parallel to a chosen direction like x-axis, can be used to store information in the form of logical "1" and "0" bits. Writing data then comes down to the ability to flip the magnetic moment of a magnet. A magnet can switch by motion of the domain walls which separate the individual magnetic domains of the magnet. In this case the
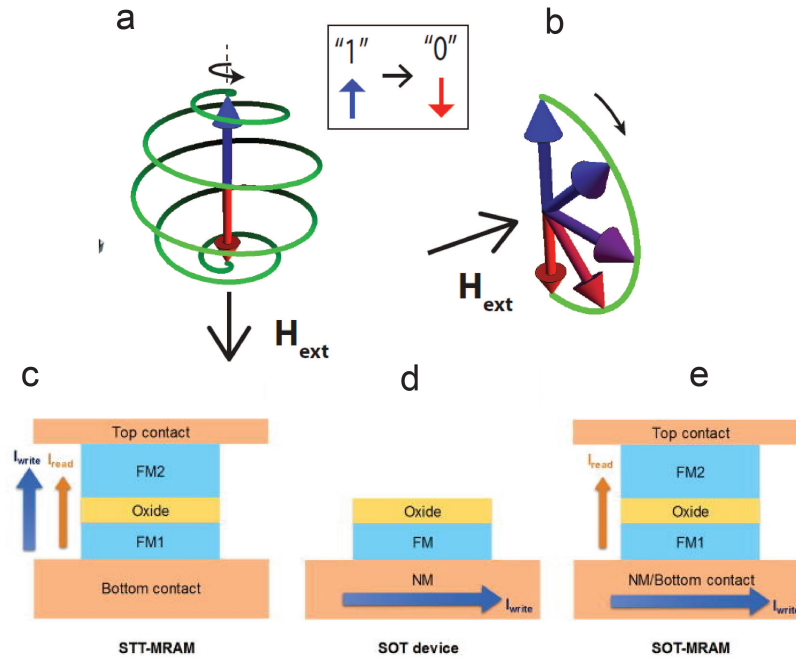
Fig. 4.1. Schematic of precessional switching for a) anti-parallel and b) orthogonal orientation of the external magnetic field (taken from [165]). c) Schematic of a Magnetic Tunnel Junction (MTJ) with FM2 as the reference layer and FM1 as the free layer. d) and e) Schematic of Spin Orbit Torque (SOT) based magnetic memory device. MRAM: Magnetic Random Access Memory (c,d and e are taken from [166])

timescale for switching ranges from tens of μs to hundreds of ns. It can also switch by precessional motion (as shown in Figure 4.1a) where the characteristic switching times are between one ns and tens of ps. These timescales are typically accessible by application of an external magnetic field. As we will see later in the chapter, laser pulses can affect the magnetic moment. Such an interaction happens at the timescales of the spin-orbit interaction ($\sim$ps or lower) and the exchange interaction ($\sim$10 fs), which is the strongest known force in magnetism [167].

As I just mentioned, this magnetic moment $\mathbf{M}$ of a magnet can precess about an effective magnetic field. This precessional motion is given by the famous Landau-Lifshitz-Gilbert equation [168]:

$$(1+\alpha^2)\frac{d\mathbf{M}}{dt} = -\gamma\mu_0(\mathbf{M}\times\mathbf{H}_{eff}) - \alpha\gamma\mu_0(\mathbf{M}\times\mathbf{M}\times\mathbf{H}_{eff}) - (\mathbf{M}\times\mathbf{M}\times\frac{\mathbf{I}_s}{eN_s})\ (4.1)$$

where α is the damping constant and $\mathbf{H}_{eff}$ is the effective magnetic field inside the magnet. $\mathbf{H}_{eff}$ can be the sum of an external magnetic field ($\mathbf{H}_{ext}$) and local fields originating from shape anisotropy, magnetocrystalline anisotropy etc. The first term in the RHS of Eq. 4.1 is related to the precession of the magnetic moment about the effective field and the second term is related to dissipation which allows the magnetic moment to spiral down and align with the effective field. This is depicted in Figure 4.1a. Neglecting anisotropies, when an external magnetic field is applied in a direction opposite to the magnetic moment, the magnet will precess and eventually align itself with the external field [167, 169]. Such motion as mentioned earlier happens in $\sim$1 ns timescales. It was also realized that if an external magnetic field pulse is applied perpendicular to the direction of the magnetic moment, with a duration of half the precession time period, then the magnetic field can switch in $\sim$100 ps timescales [170, 171]. This is depicted in Figure 4.1b. Since the precession time period depends on the external magnetic field, one would think that a larger magnetic field would lead to faster switching. That is not necessarily true. Using uniquely short and strong magnetic field pulses induced by relativistic electron bunches at the Stanford Linear Accelerator, Tudosa et al. have shown that deterministic magnetization switching does not take place for pulses shorter than 2.3 ps [172].

The third term in Eq. 4.1 was incorporated after the development of the field of spintronics. For a detailed discussion on spintronics, the interested reader can refer to the book by Supriyo Datta [168]. Figure 4.1c shows the schematic of one of the devices studied in the field of spintronics. It is called a Magnetic Tunnel Junction (MTJ). MTJs consist of a tunneling barrier sandwiched between a reference magnetic layer (FM2) and a free magnetic layer (FM1). By passing a current through the stack ($\mathbf{I}_{write}$)in one way or the other, the magnetic moment of the free layer can be flipped either up or down. This method of spin current induced magnetic switching is called Spin Transfer Torque or STT. It was theoretically predicted by Slonczewski [173] and Berger [174] in 1996 and shortly thereafter was experimentally demonstrated [175, 176]. The current required to achieve this switching was in the range of 10^6-10^7 A/cm^2. Later with the fabrication of perpendicular anisotropy CoFeB-MgO magnetic tunnel junctions [177, 178] the current requirement could be slightly relaxed, but not to a sufficient extent for widespread adaptation of magnetic tunnel junction based spintronic devices. In 1971, D'yakonov and Perel' [179] theoretically predicted the Spin Hall Effect (SHE) [180,181], which arises from relativistic spin-orbit coupling and generates transverse spin currents from injected charge currents. This is demonstrated in Figure 4.1d. The spin currents obtainable in this way were originally too small. Later on with the demonstration of Giant Spin Hall Effect [182, 183] substantially larger spin currents could be obtained. Figure4.1e shows the schematic of a read-write methods for magnetic memory operating on Spin Orbit Torque or SOT resulting from SHE.

It should be kept in mind that all the spintronic devices are limited, in terms of switching speeds, to about 100 ps (Eq. 4.1). So there is a need to look for alternate methods for magnetic media recording. Optics has played a significant role when it comes to alternate methods for magnetic memory device operation. So from here on now, I will focus on the role of optics in magnetic memory devices. I will first talk about the concept of Heat Assisted Magnetic Memory (HAMR). Here the timescale of switching is still limited to precessional switching, because one still

applies a magnetic field pulse to switch magnetic domains. However, in the discussion on All Optical Magnetization Switching (AOMS) with fs laser pulses, we will see much faster switching timescales. This is so because we would encounter a new domain of physics for AOMS where Eq. 4.1 is no longer a complete description.

4.1 Heat Assisted Magnetic Recording (HAMR)

Heat Assisted Magnetic Recording (HAMR) is a method of data storage that has received a lot of attention in recent years, both from academic and industry research groups. HAMR technology can increase the data storage capacity to over $1\text{Tb}/\text{in}^2$. This would be a significant improvement in memory capacity over the more widely used technology of Hard Disk Drives or HDD. Just recently, Seagate Technology has announced that HAMR drives with 16 TB and 20 TB capacity would be commercially available as early as late 2020. These drives can seemingly replace HDD without any changes in modern-day computer architecture. The magnetic material of choice for HAMR, at least for companies like Seagate and Western Digital, has been perpendicular FePt granular magnetic media. For the interested reader, details on the growth and characterization of such magnetic media can be found in reviews like [188]. Figure 4.2a compares the operation of HDD and HAMR through schematics [184]. A conventional HDD operates with a perpendicular recording head that moves above a disk medium where the data are stored as vertical magnetized bits. The write head, consisting of write coils and a write pole and a return pole is at the vertical trailing end of the scanning head. For HAMR the read/write arrangement is slightly different as shown in Figure 4.2a. In order to achieve high storage density one needs to reduce the magnetic bit size. This calls for a reduction in the size of the magnetic domains. However, one needs to ensure that the magnetic domains are not susceptible to random thermal fluctuations. The size at which magnetic state of a domain is no longer thermally stable is called the superparamagnetic limit [189]. It is given by

$$\frac{K_u V}{k_B T} \geq 60 \tag{4.2}$$
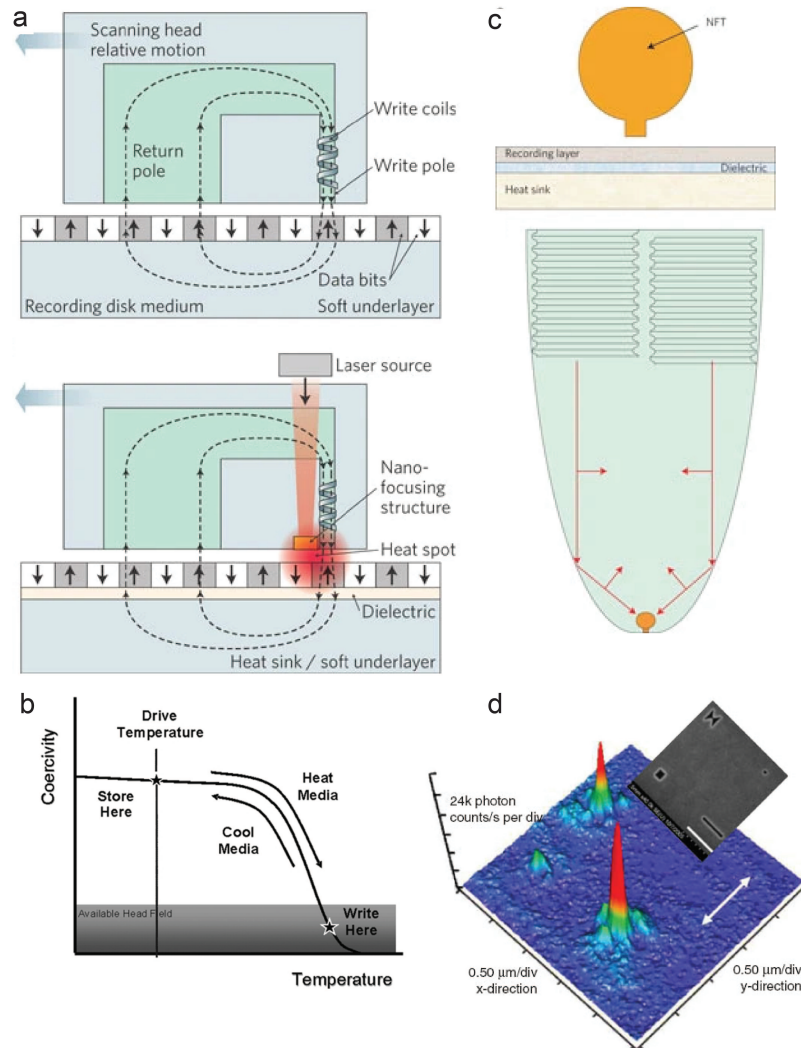
Fig. 4.2. a) Schematic showing the operation of a HDD (top) and HAMR drive (bottom) [184]. b) Plot of reduction of coercivity of magnetic media with increasing temperature [185]. c) (top) Close-up view of the Near Field Transducer (NFT) showing its vertical position with respect to the magnetic medium. (bottom) A planar solid immersion mirror with a dual offset grating is used to focus a waveguide mode onto the lollipop NFT [186]. d) Near-Field Scanning Optical Microscope image for different apertures in a 160 nm Au film for using as a NFT. Inset shows the SEM image of the respective apertures (a bow-tie aperture, larger and smaller square aperture and a rectangular aperture) [187]. White arrow is the electric field polarization of incident light.

where K_u is the uniaxial anisotopy, V is the volume and T is the temperature. In order to avoid the superparamegnetic limit, as the volume V of bits reduce, one needs to design magnetic domains with higher K_u. This invariably leads to higher coercivity and larger write fields for magnetic bits. In order to circumvent this, a laser spot is used to heat up the magnetic bit and reduce its coercivity. Thus in HAMR a laser is used to achieve reasonable write fields to address magnetic bits. Figure 4.2b shows how the write field of magnetic bits can be brought down to reasonable values by increasing the temperature [185].

The use of plasmonic antennas has been suggested in order to improve the laser light collection efficiency of the magnetic media. A review of plasmonic structures (also called Near Field Transducers or NFTs) used in HAMR has been written by Zhou et al. [74]. Figure 4.2c(top) shows the arrangement of a lollipop shaped NFT with respect to the recording medium [186]. The bottom half of the figure shows a planar solid immersion mirror with a dual offset grating that can be used to focus the waveguided laser mode onto the NFT. The red arrows show the direction of the wavevector and the electric field of laser light. The arrangement excites a longitudinal (vertical) mode which results in a high field density at the bottom of the small peg of the lollipop NFT. Figure 4.2d shows the electric field intensity that can be achieved by using several different kinds of apertures as the NFT [187]. These apertures are made in a 160 nm thick Au film and show plasmonic enhancement. Among these apertures, it can be seen that the rectangular aperture and the bow-tie aperture are very suitable for high field enhancement and coupling to the magnetic recording medium.

4.2 All Optical Magnetic Switching (AOMS)

Following the experimental demonstration of ultrafast (few hundreds of fs) demagnetization utilizing 60 fs laser pulses in 1996 [190], the magnetization dynamics in these unprecedented time scales has been extensively investigated both theoreti-

cally and experimentally [191]. Many models have been proposed to explain AOMS. Notable among these are Inverse Faraday Effect to explain All Optical Helicity Dependent Switching (AO-HDS) [191], transfer of angular momentum from light to the magnetic system [192] as well as through a transient ferromagnetic-like state in ferrimagnets like GdFeCo [193]. Laser induced superdiffusive spin currents may also contribute to AO-HDS [194]. Several different mechanisms have also been studied in the context of magnetization dynamics induced by fs laser pulses. These are electron-electron scattering [195], photon-spin coupling [196, 197], electron-phonon coupling [198, 199] and electron-magnon coupling [200, 201]. Moreover there have also been studies focused on the transfer of angular momentum [202], separating the spin and orbital angular moment dynamics [203] as well as probing the timescale of exchange interaction in magnetic materials [204]. In the following sections, I will briefly outline some reported literature on AOMS in ferrimagnets, synthetic ferrimagnets and ferromagnets.

4.2.1 Ferrimagnets

The vast majority of AOMS literature involves ferrimagnets and in particular Gadolinium Iron Cobalt (GdFeCo). The Gd and Fe sublattices are anti-ferromagnetically coupled in this material i.e. they point opposite to each other. However one sublattice has a larger moment than the other which gives the material a net magnetic moment. The magnetic properties of this material such as coercivity, Curie temperature etc. can be tuned by altering the Gd:Fe ratio. Figure 4.3a shows one of the first studies on switching GdFeCo with 40 fs 800 nm laser pulses performed by Stanciu et al. [205]. The left part of the picture shows the two oppositely aligned magnetic domains represented by dark and light areas in the magneto-optical image. The middle part shows the same image but after the sample has been exposed to right circularly (σ^+), left circularly(σ^-) and linearly (L) polarized laser pulses. As can be seen, the right and left circular polarizations alter one of the domains while leaving
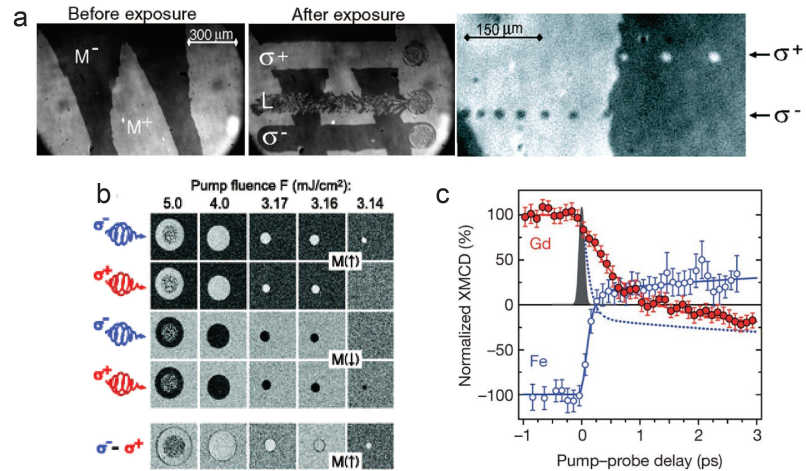
Fig. 4.3. a) Magneto-optical image of a sample of $Gd_{22}Fe_{74.6}Co_{3.4}$ before laser exposure (left) and after laser exposure (middle). (right) The same sample imaged after laser pulse exposure where the sample sweep rate was high enough such that each pulse illuminated a different area. σ^+: right circularly polarized light, σ^-: left circularly polarized light and L: linearly polarized light [205]. b) Magneto-optical images of $Gd_{26}FeCo$ film after it has been exposed to a single 100 fs pulse of varying fluences. The last row is obtained by subtracting the images of the top two rows [206]. c) Dynamics of the Gd and Fe sublattice after exposure to fs laser pulses as obtained from X-ray Magnetic Circular Dichroism studies [193].

the other unaffected. The linearly polarized light leads to a random magnetization of the exposed area. The laser fluence used in this case was 11.4 mJ/cm^2. The right part of Figure 4.3a shows a magneto-optical image where the sample is swept at a higher speed such that each laser pulse illuminates a different area of the sample. The dots shown in the image clearly indicate that a single fs laser pulse is sufficient to switch the magnetic domains. The laser fluence used in this case was 2.9 mJ/cm^2. Since we clearly see a helicity dependent switching, the Inverse Faraday Effect was believed to be the explanation for GdFeCo magnetization reversal with fs laser pulses.

This viewpoint however was corrected later on. Figure 4.3b shows magneto-optical images of Gd$_{26}$FeCo film illuminated with a 100 fs laser pulse of varying fluences ranging from 3.14 mJ/cm^2 to 5 mJ/cm^2. In Figure 4.3a we have already seen the evidence of laser helicity dependent switching. In Figure 4.3b also the authors report an intensity range where they observe helicity dependent switching. This is clearly seen at the 3.14 mJ/cm^2 fluence. However, at higher fluences the authors observe a helicity independent switching. There have also been reports of switching in GdFeCo with linearly polarized laser pulses [193]. In [193], the authors used a linearly polarized 100 fs 800 nm laser pulse to study the dynamics of the Fe and Gd sublattice using 100 fs soft X-ray pulses. The results of their experiments are shown in Figure 4.3c. It can be clearly seen that immediately following the laser pulse (dark shaded) excitation, the two sublattices show widely different dynamics. A detailed theoretical description of ongoing processes in GdFeCo upon fs laser excitation can be found in [207]. Basically, the fs laser pulse heats up the electronic subsystem to several hundred of degrees above the Curie temperature. In such a scenario, the exchange coupling between Gd and Fe is no longer the dominant force and the sublattices demagnetize independent of each other. Consequently, Fe sublattice loses its magnetization in 700 fs whereas the Gd sublattice takes around 1.5 ps (Figure 4.3c). After a few hundred fs following laser excitation, the temperature is lower than the Curie temperature and this means that exchange coupling once again is the dominant force. Therefore, even when the Fe sublattice has lost its magnetic moment, the rate of transfer of angular momentum

for the Fe sublattice is non-zero. This turns the Fe magnetic moment in the same direction as Gd after 700 fs. Therefore there exists a transient ferromagnetic like state where both the sublattices have their magnetic moment in the same direction. Eventually, the Gd sublattice flips due to the exchange interaction at larger timescales of a few ps when the lattice has substantially cooled down. In some other literature, 50 fs laser pulse induced switching in GdFeCo nanostructures have been reported [208]. This is particularly relevant to my research work on GdFeCo nanomagnets which I will outline in Chapter 5. Also Bokor and collaborators have reported that even electric heat currents induced by laser pulses, instead of direct laser absorption, can induce magnetization change in GdFeCo [209].

4.2.2   Synthetic Ferrimagnets and Ferromagnets

Investigations on AOMS for synthetic ferrimagnets and ferromagnets have been relatively limited in number compared to GdFeCo. Personally, I am not very familiar with the physics behind AOMS in these materials, which is believed to be very different from the physics of AOMS in GdFeCo. So I will restrict myself to mentioning a few notable literature pertaining to AOMS in synthetic ferrimagnets and ferromagnets. A magnetic material like GdFeCo is made of a combination of a Transition Metal (TM) element (Fe) and Rare Earth (RE) element (Gd). So a natural question is whether AOMS can be observed in coupled multilayers of RE-TM. The answer is yes and a detailed study on this by Fullerton and coworkers can be found in [210]. In that paper, the authors report All-Optical Helicity Dependent Switching (AO-HDS) in [Tb(2.5 nm)/Co(2.5 nm)]$_5$ multilayers with 100 fs 800 nm laser pulses. Here Tb is the RE and Co is the TM element. The next idea was to test if the RE was essential for a magnetic material to show AOMS. In the same paper, Fullerton and coworkers showed AO-HDS in Ta(4 nm)/Pd(3 nm)/[Co(1 nm)/Ir/Co(0.4 nm)/Ni(0.6 nm)/Pt(0.3 nm)/Co(0.4 nm)/Ir]$_5$/Pd(3 nm) multilayer stack. This is a synthetic ferrimagnet where Co(1 nm) and Co(0.4 nm)/Ni(0.6 nm)/Pt(0.3 nm)/Co(0.4 nm) are

exchange coupled. No RE element was present in the stack. Synthetic ferrimagnets made of Pt/Co/Gd have also been shown to switch with laser pulse fluence as low as 1.2 mJ/cm^2 for a Co thickness of 0.8 nm. Beens et al. have reported on the switching of a Pt/Co(0.2 nm)[Ni(0.6 nm)/Co(0.2 nm)]$_N$Gd multilayer stack in the absence of a magnetization compensation temperature [211]. They believe that the switching mechanism occurs as a front of reversed Co magnetization that nucleates near the Co/Gd interface and propagates through the Co layer driven by exchange scattering. AO-HDS has also been reported in FePtAgC, which is a granular ferromagnetic medium and Co(0.4 nm)/Pt(0.7 nm) multilayers [212]. AO-HDS in FePt granular ferromagnets due to magnetic circular dichroism has also been reported elsewhere [213]. Single shot AOMS has been reported by Bokor and coworkers in Co/Pt multilayers exchange coupled to a GdFeCo ferrimagnetic layer [214]. The switching time in this case has been reported as 7 ps.

4.3   Optomagnetic fields due to Inverse Faraday Effect

As I mentioned earlier, the Inverse Faraday Effect (IFE) has been proposed as a possible explanation for AOMS. IFE can be modeled as an optomagnetic field ($\mathbf{H}_{OM}$) that is generated inside the magnetic material due to the incident laser pulses [215]. Mathematically, the optomagnetic field is given by [206]

$$\mathbf{H}_{OM} = \sigma\beta\varepsilon_0 \mid \mathbf{E} \times \mathbf{E}^* \mid \hat{\mathbf{n}} \tag{4.3}$$

where β is the magneto-optical susceptibility of the magnetic material, ε_0 is the permittivity of free space, $\hat{\mathbf{n}}$ is the direction of electromagnetic wave propagation and $\mathbf{E}$ is the electric field vector of the electromagnetic wave inside the magnetic material. $\sigma = \pm 1$, depending on the helicity of circularly polarized light. It is clear that Eq. 4.3 would give zero optomagnetic field for linearly polarized light. This being said, it should be kept in mind that the derivation of optomagnetic field assumes a dissipation-less medium. Since the optomagnetic field depends on the magnitude of square of the electric field i.e. the intensity of incident electromagnetic wave, one can assume
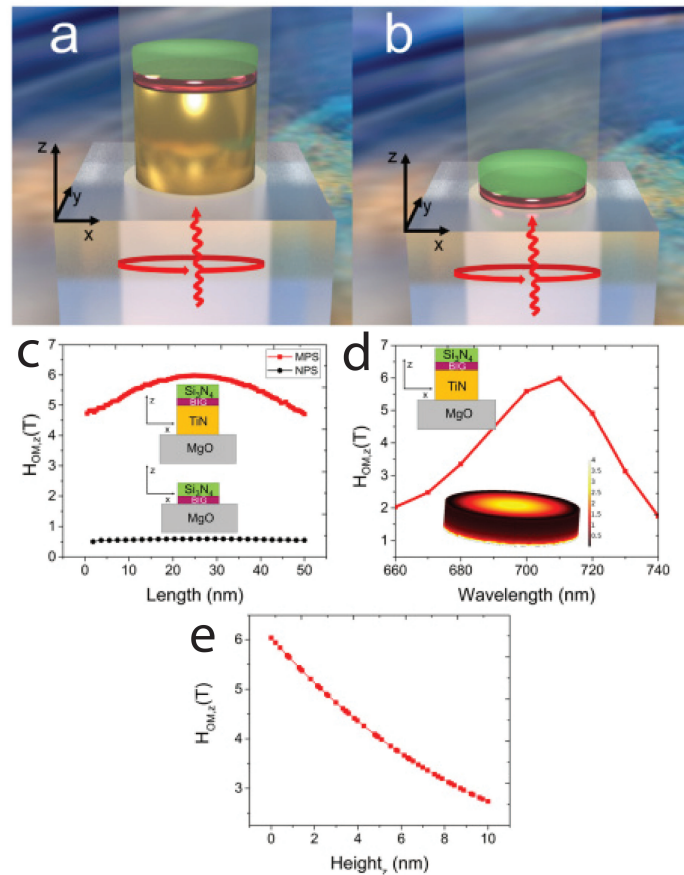
Fig. 4.4. a) Schematic of proposed magnetoplasmonic stack or MPS (yellow-plasmonic antenna, purple-magnetic layer, green-capping layer). (b) Schematic of nonplasmonic stack or NPS (only a nanomagnet with the capping layer). In both figures, the red circular arrow at the bottom indicates that the illumination is with circularly polarized light and the curly red arrow indicates the direction of incidence. Substrate is MgO. c) Comparison of the z-component of the optomagnetic field intensity along the x-axis of BIG-TiN interface for a 10nm thick BIG layer in the MPS (nanomagnet with TiN resonator) and NPS (only nanomagnet) sample. Illumination is with circularly polarized light of intensity $1mJ/cm_2$ at 710 nm wavelength under normal incidence. d) Wavelength dependence of the z-component of the opto-magnetic field for the MPS sample (50 nm diameter) at the stack center at the TiN-BIG interface. Inset: Plot of $\mathbf{H}_{OM,z}$ over the entire volume of the magnet. e) Plot of $\mathbf{H}_{OM,z}$ along the axis of BIG nanomagnet. (z = 0 nm refers to the TiN-BIG interface)

that we should be able to enhance the optomagnetic field generated in magnets when they are coupled to plasmonic resonators. I will present some simulation results next which elucidate this idea. This part is borrowed from my publication [216] which was done in collaboration with Prof. Ernesto Marinero.

The numerical studies were performed with a Finite element based solver in COM-SOL Multiphysics. Figure 4.4a and b show the schematic of the two structures considered for simulations. The former shows a magnetoplasmonic stack (MPS) configuration whereas the latter shows a nonplasmonic stack (NPS) configuration on a MgO substrate. For both the figures, purple and green represent the magnetic layer and the capping layer, whereas the plasmonic resonator in Figure 4.4a is shown in yellow. For the simulations, I chose TiN as the plasmonic metal (thickness 30 nm), Si_3N_4 as the top cap (thickness 20 nm) and Bismuth Iron Garnet or BIG (thickness 10 nm) as the magnet. The diameters of both MPS and NPs were kept at 50 nm and for the chosen dimensions, simulations showed a plasmon resonance at 710 nm wavelength. The simulations were performed at normal incidence, through the MgO substrate, considering circularly polarized light.

Figure 4.4c shows the z-component of the optomagnetic field, $\mathbf{H}_{OM,z}$ along the x-axis at the lower interface of the magnet layer for both MPS and NPS sample. We can clearly see a 10-fold enhancement in $\mathbf{H}_{OM,z}$ due to the plasmon resonance. This is confirmed through the wavelength dependent plot of $\mathbf{H}_{OM,z}$ for the MPS configuration (Figure 4.4d), where the $\mathbf{H}_{OM,z}$ value along the axis of the stack at the bottom interface of the magnet is considered. The highest value of $\mathbf{H}_{OM,z}$ is obtained at 710 nm wavelength corresponding to the plasmon resonance. The inset of Figure 4.4d shows a color map of $\mathbf{H}_{OM,z}$ over the entire volume of the magnet. The simulation predicts a volume averaged value of 2.39 T for $\mathbf{H}_{OM,z}$. Figure 4.4e shows how $\mathbf{H}_{OM,z}$ decreases along the thickness of the BIG layer away from the TiN interface. These results confirm the plasmonic improvements that can be achieved in AOMS when magnets are coupled to plasmonic resonators.

5. PLASMON ASSISTED MAGNETIC RECORDING IN MAGNETOPLASMONIC NANOSTRUTURES

In this chapter I will report on my research in magnetization reversal of nanomagnets coupled to plasmonic resonators. Since GdFeCo has been the most widely researched material for AOMS, that was the magnetic material of choice for me. I should mention at this time that this is of course not the first time plasmonic nanostructures have been used for AOMS demonstration in ferrimagnets composed of a rare earth and transition metal. Figure 5.1 shows the work done by Liu et al. where they show plasmon induced switching in a continuous layer of $Tb_{22}Fe_{69}Co_9$ [217]. As shown in Figure
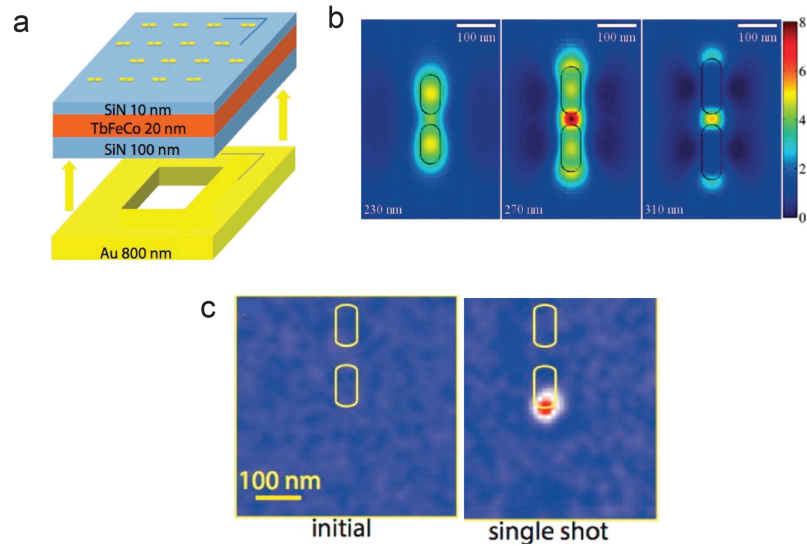
Fig. 5.1. a) Schematic of the sample with Au nanorods on top of TbFeCo sample. b) Numerical simulations that show plasmonic enhancement of the electric field at the gap between two antennas for three different antenna lengths namely 230 nm , 270 nm and 310 nm. c) Magnetic contrast image taken from the difference of left and right circularly polarized X-ray diffraction before and after exposure with a single fs laser pulse [217].

5.1a, the TbFeCo layer was sandwiched between two layers of Si_3N_4 of 10 nm and 100 nm thickness. On top of that, Au nanorod antenna-pair arrays were fabricated. Simulations (at 1030 nm wavelength) showed an electric field enhancement in the gap between the two Au antennas in a pair due to the plasmon resonance (Figure 5.1b). For AOMS, the samples were exposed to single pulses from a 1030 nm 320 kHz 500 fs Calmar Cazadero Er-doped fiber laser. As Figure 5.1c shows, a single laser pulse with an intensity of 3.7 mJ/cm^2 was enough to switch a small area close to the Au nanorod. One thing to note is that the switched area does not coincide with the area of maximum electric field as shown in Figure 5.1b. The images in Figure 5.1c are magnetic contrast images obtained from taking the difference of diffraction patterns of left and right circularly polarized X-rays tuned at 706.8 eV (Fe L_3 resonance).

Figure 5.2 shows polarization dependent layer-selective switching in two layers of GdFeCo as reported by Ignatyeva et al. [218]. The sample is a multilayer stack on glass consisting of (from substrate) Si_3N_4(5 nm)/$Gd_{26}(FeCo)_{74}$(10 nm)/Si_3N_4(80 nm)/$Gd_{27}(FeCo)_{73}$(10 nm)/Si_3N_4(10 nm). A SiO_2 prism is coupled to the other side of the glass to excite surface plasmons in the Kretschmann geometry [12] (Figure 5.2a). Figure 5.2b and c show the partial absorption as a function of stack depth and the total absorption of the two GdFeCo magnetic layers for p and s polarized light illumination respectively. It can be clearly seen that one GdFeCo layer absorbs more for p polarized light and the other absorbs more for s polarization. This is due to the generation of a plasmon in one case and not in the other. And following the discussion of AOMS in GdFeCo in Chapter 4, it is clear how increasing absorption in GdFeCo can lead to efficient magnetizaion reversal. A 800 nm 100 fs Ti:sapphire laser was used for AOMS in this study. Figure 5.2d shows the magneto-optical image obtained after illumination of the sample by a single pulse of p (left) and s (right) polarized light. The fluence used was 12 mJ/cm^2. Over a single spot, different grayscale values show different magnetization of the combined stack as confirmed by magneto-optical contrast measurement (I). For each arrow pair, the left one is for the bottom and the right one is for the top GdFeCo layer.
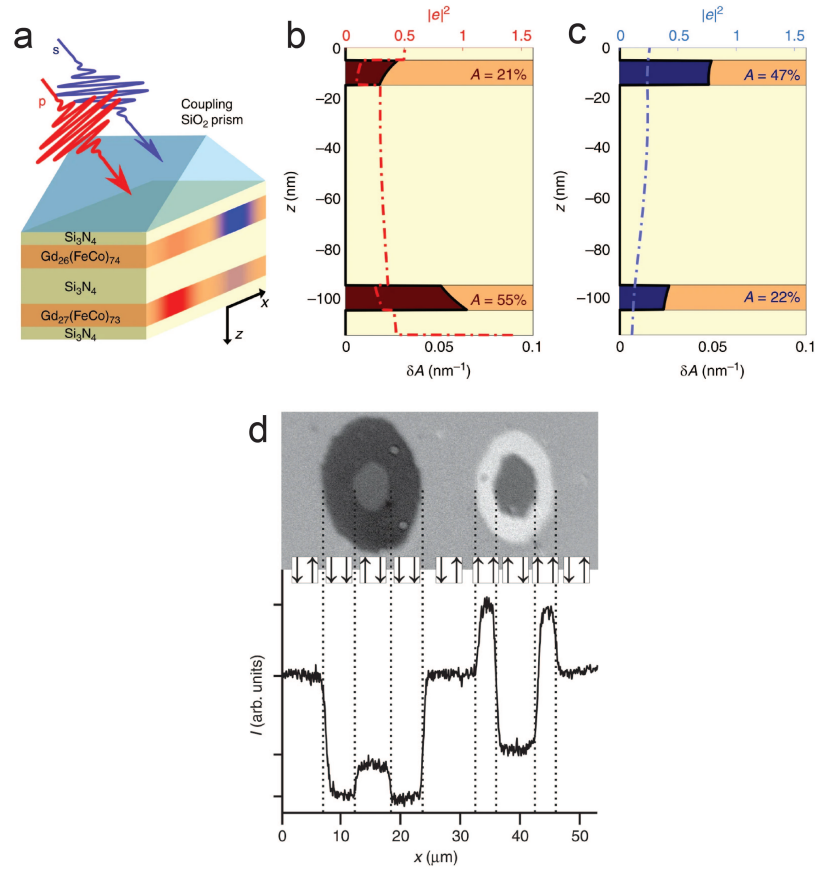
Fig. 5.2. a) Schematic representation of the layer selective magneti-zation reversal. b) Absorption (A) and partial absorption $(\delta A(z))$ for the multilayer stack with p-polarized illumination. c) Absorption (A) and partial absorption $(\delta A(z))$ for the multilayer stack with s-polarized illumination. d) Polarization dependent AOMS where each pair of arrows represent the magnetization orientation of the bottom(left) and top(right) GdFeCo layer. The left spot is for p-polarized laser pulse and the right spot is for s-polarized laser pulse [218].

I will now move on to describing my own experiments. The main difference between my research and the two works that I just outlined is that in my research, I consider plasmonic resonators coupled to nanomagnets as opposed to continuous magnetic layers. This work has been performed in collaboration with Prof. Vladimir Belotelov from the Russian Quantum Center, Prof. Arata Tsukamoto from Nihon University, Japan and Prof. Aleksei V. Kimel from Radboud University, Netherlands.

5.1 Material Growth, Fabrication and Characterization

The magnetic layer in my samples were grown on MgO. The choice of MgO was made because of its high thermal conductivity and optical transparency at wavelengths used for experiments. The magnetic layer consisted of (from substrate) a 20 nm thick Si_3N_4 layer, a 5 nm thick $Gd_{31}Fe_{60.4}Co_{8.6}$ layer and a 3 nm top layer of Si_3N_4. The GdFeCo had a magnetisation compensation temperature of 212 K and a coercivity of 5 Oe. Following this, a composite nanostructure of 5 nm Al_2O_3, 30 nm Au and 50 nm SiO_2 was fabricated on top of the magnetic films using e-beam lithography and lift-off technique. First PMMA495 A4 was spin-coated at 2500 rpm with a ramp of 2 s for 60 s followed by a baking at 180 °C for 3 min. After waiting for about 10 mins, PMMA950 A2 was spin-coated at 4000 rpm with as ramp of 2 s for 60 s followed by a baking at 180 °C for 3 min. E-beam exposure was done with a JEOL-8100FX e-beam writer with 2 nA beam current. After exposure, the patterns were developed in MIBK:IPA (1:3) for 60 s followed by rinsing in IPA for 20 s. After this a composite stack of $Al_2O_3/Au/SiO_2$ was deposited by e-beam evaporation. Finally, the lift-off was done in acetone for 1 hr. Then the top 50 nm SiO_2 layer was used as a mask to etch the magnetic layer in an AJA Ion Mill system where I used an end-point detection scheme to detect Mg ions from the substrate as an etch stop indicator. The etching reduces the thickness of the SiO_2 mask to about 20 nm. This is how the Magnetoplasmonic Stack (MPS) was fabricated. A similar process but without the Al_2O_3 and Au layer was used to fabricate the Nonplasmonic Stack
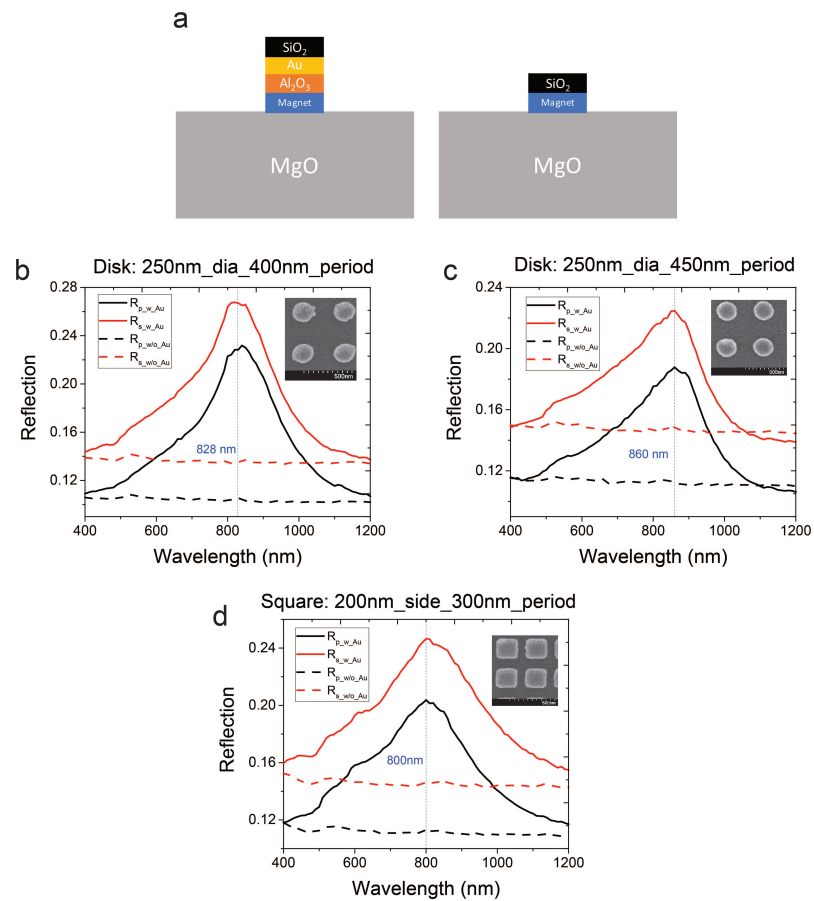
Fig. 5.3. a) Schematic of the Magnetoplasmonic (MPS) and Nonplasmonic (NPS) stack. b) Reflection of p (black) and s (red) polarized light for nanodisk array of 250 nm diameter and 400 nm period. c) Reflection of p (black) and s (red) polarized light for nanodisk array of 250 nm diameter and 450 nm period. d) Reflection of p (black) and s (red) polarized light for nanosquare array of 200 nm side and 300 nm period. Solid lines are for the MPS stack and dashed lines are for the NPS stack
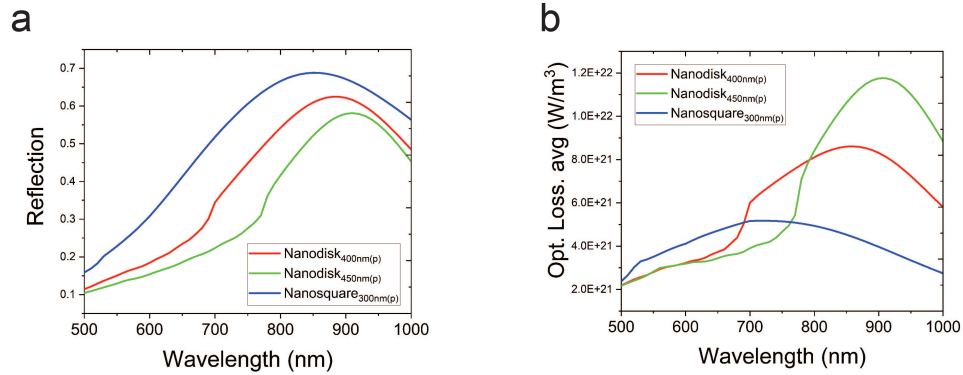
Fig. 5.4. a) Simulated reflection plots for the MPS samples for all three arrays ND-400, ND-450 and NS-300. b) Volume average of the optical loss in the MPS sample in the GdFeCO layer.

(NPS). Figure 5.3a shows the schematic of these two structures. Three different kinds of nanostructure arrays were fabricated; a nanodisk array of 250 nm diameter and 400 nm period (ND-400), a nanodisk array of 250 nm diameter and 450 nm period (ND-450) and a nanosquare array of 200 nm side and 300 nm period (NS-300). The reflection from all these arrays for both the NPS and MPS stack are shown in Figure 5.3b,c and d. Black curves are for the p polarized light and red curves are for s polarized light (dashed lines are for NPS and solid lines are for MPS sample). The peak in reflection for the MPS samples indicates the presence of a plasmon resonance. The measurements were performed at 20° incidence. The inset of Figure 5.3b,c and d show an SEM image of the corresponding MPS sample taken prior to etching the magnetic layer. SEM images of the final arrays were hard to obtain as MgO is an insulating substrate.

Figure 5.4a and b show results obtained on the MPS samples for the three arrays through numerical simulations. For simulations, I used a Finite Element based method in COMSOL Multiphysics. The simulated reflection peaks for all the arrays qualitatively match the experimental data in Figure 5.3b,c and d. The experiment data for reflection is slightly blue-shifted possibly because the nanostructure lateral
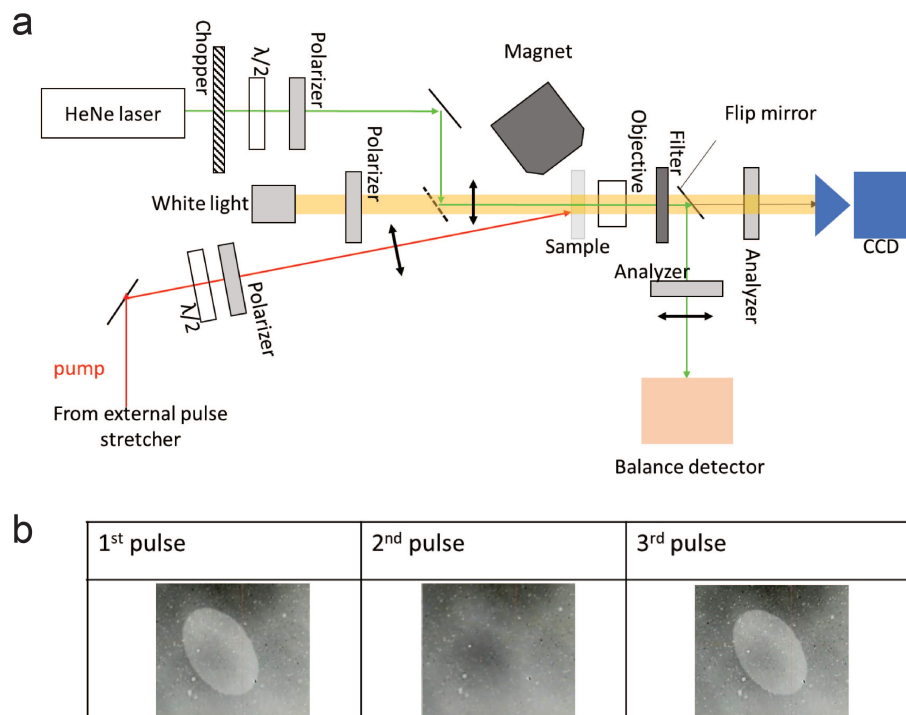
Fig. 5.5. a) Schematic of the laser pump-probe setup for measuring AOMS. b) Single shot reversible switching for a continuous 5 nm GdFeCo magnet layer.

dimensions were reduced during ion mill etching. Figure 5.4b shows the calculated optical loss (volume averaged) in the GdFeCo layer for the MPS sample obtained from simulations. For the ND-400 and ND-450 arrays, the loss peak coincides with the reflection peak but not so for the NS-300 sample. In the simulations, the optical properties of GdFeCo were taken from [219]. It should also be noted that for simulations, I considered a 1W/unit cell illumination for each different array.

5.2 Measurement Setup

Figure 5.5a shows the schematic of the optics setup for measuring AOMS. A 800 nm 100 fs linearly polarized Ti:sapphire laser was used as the optical pump. The beam spot radius was 50 μm, the pulse power was 0.43 mW (which corresponds to a fluence
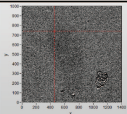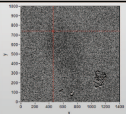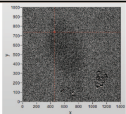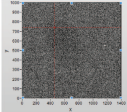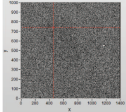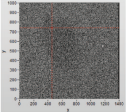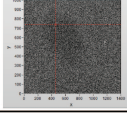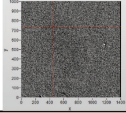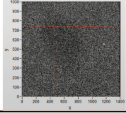
B	1st pulse	2nd pulse	3rd pulse
0mT	+x	-x	+x
0.6mT			
1.5mT			
3mT			
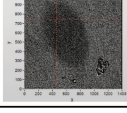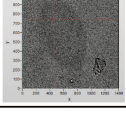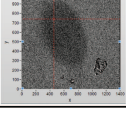
Fig. 5.6. Magneto-optic contrast images obtained from magnetization switching measurements on the ND-400 MPS sample. An external magnetic field is applied normal to the substrate (x-axis) during the measurements. Reversible switching was obtained for magnetic field of 3 mT.

of 5.47 mJ/cm^2/pulse) and the angle of incidence was 15°. Figure 5.5a also shows a white light source used to obtain the magneto-optic contrast images of the sample. A separate He-Ne laser is used to perform MOKE measurements on the sample using an electromagnet. Figure 5.5b shows the AOMS measurement results on a continuous layer of GdFeCo. As can be seen, the magnet layer can be reversibly switched with subsequent laser pulses as has been reported in literature for this material. For us, it was important to do this sanity check so as to confirm that a GdFeCo layer with thickness as low as 5 nm does indeed undergo AOMS (not reported in literature to the best of my knowledge).

5.3 Results and Discussions

Figure 5.6 shows the results for magnetization switching obtained on the ND-400 MPS sample. The first thing to note is that an external magnetic field is needed
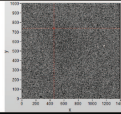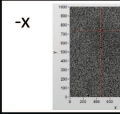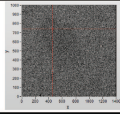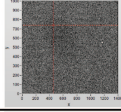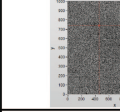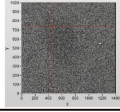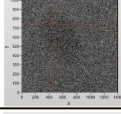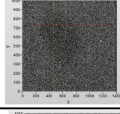
B	1st pulse	2nd pulse	3rd pulse
0mT	+x	-x	+x
0.6mT			
1.5mT			
3mT			
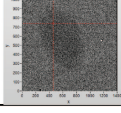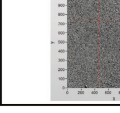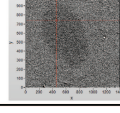
Fig. 5.7. Magneto-optic contrast images obtained from magnetization switching measurements on the ND-450 MPS sample. An external magnetic field is applied normal to the substrate (x-axis) during the measurements. Reversible switching was obtained for magnetic field of 3 mT.

to observe reversible switching for this sample. The field is applied normal to the substrate which is taken as the direction of the x-axis in our case. The field direction is deliberately switched for alternate laser pulses in order to assist laser pulse induced switching. This is in stark contrast to the result obtained for the continuous GdFeCo film where no external field was required. The first row in Figure 5.6 shows that the first three laser pulses barely produce any magneto-optic contrast with zero applied magnetic field. Subsequent rows correspond to slightly higher magnetic fields until we see reversible switching at 3 mT.

Figure 5.7 and 5.8 show measurement results on the ND-450 and NS-300 MPS samples respectively. Both results are very similar to the results obtained for ND-400. I would however note that the NS-300 sample shows a magnetic contrast even at zero applied magnetic field (top row of Figure 5.8). The drawback is that subsequent laser pulses don't show any reversibility of magnetic moment. Also to be noted, all MPS samples show reversible switching at the same external field of 3 mT. The spots in

B	1st pulse	2nd pulse	3rd pulse
0mT	+x	-x	+x
0.6mT			
1.5mT			
3mT			
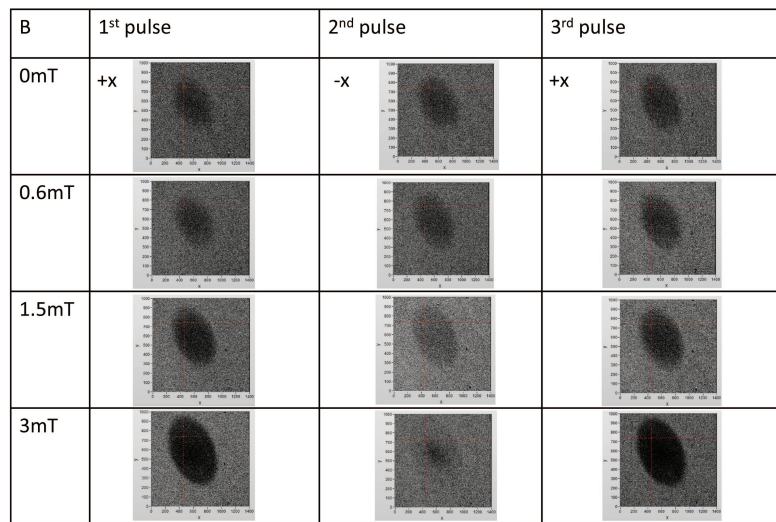
Fig. 5.8. Magneto-optic contrast images obtained from magnetization switching measurements on the NS-300 MPS sample. An external magnetic field is applied normal to the substrate (x-axis) during the measurements. Reversible switching was obtained for magnetic field of 3 mT.
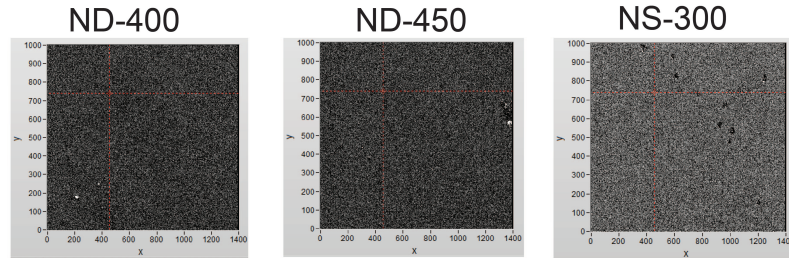
Fig. 5.9. Magneto-optic contrast images obtained from magnetization switching measurement on all three arrays for the NPS sample.

Figure 5.8 for the NS-300 sample are darker because it has the highest areal density of magnetic material (about 36%) compared to 30% for ND-400 and 24% for ND-450. Figure 5.9 shows the magneto-optic contrast images obtained for all three arrays for the NPS sample. No switching is observed in any case, even after application of an external field for multiple laser pulses. This shows that the given fluence is not sufficient to switch free standing GdFeCo nanomagnets. However, coupling with a Au plasmonic resonator allows larger optical absorption in the nanomagnets thereby leading to magnetization reversal (albeit in the presence of an external magnetic field). This verifies my initial hypothesis that plasmonic resonances could lower the optical energy required for magnetization reversal.

The issue of the external magnetic field still needs to be addressed. It could be that nanopatterning altered the coercivity of the nanomagnets, compared to a continuous film and also created magnetic domains without perpendicular anisotropy near the nanostructure edges. Hence the patterned samples behave differently compared to continuous thin magnetic films with regards to AOMS. At this point, we need more experiments such as pump wavelength dependent studies and/or material characterization to answer this question. Unfortunately for me, the COVID-19 pandemic has called for a halt in experimental endeavours and as of this writing, things have not gone back to normal, thereby delaying additional measurements.

6. CONCLUSION

In conclusion I would like to highlight some of the ongoing research in our group (led by Prof. Vladimir M. Shalaev and Prof. Alexandra Boltasseva) which are continuation and/or extension of the research projects I have described in my thesis. I feel that these ongoing endeavours can produce some truly significant results in the future.

In the case of plasmonic photocatalysis, I feel that the field has a more promising future not in solar energy harvesting but in photothermal/photodynamic cancer therapy [73, 220]. This is because, the cost for nanopatterning plasmonic structures on top of the active semiconductor material for efficient solar energy collection would not be commercially viable. One can use random distribution of nanoparticles, but that doesn't leave much room for designing solutions to cater to specific problems. On the other hand, photothermal therapy, which is laser induced heating of plasmonic nanoparticles to kill cancerous cells, would be a much more reasonable problem to tackle. While a lot of research work has already happened in this regard, photodynamic therapy (PDT) [221] is a more sophisticated version of photothermal therapy and has recently received a lot of attention. PDT involves localized generation of $^1O_2$ and other reactive species in a photoactive semiconductor upon laser illumination to treat cancerous cells. I have participated in such a research project here at Purdue which has been led by my colleague Xiaohui Xu [222]. In this work we used commercially available plasmonic TiN nanoparticles, instead of the more expensive Au nanoparticles and coated them with a thin layer of photoactive TiO_2. We showed that when illuminated with a 700 nm 100 fs laser, these nanoparticles showed increased production of reactive $^1O_2$ which can be used for PDT. The laser light excites plasmons in the TiN core which decays into hot electrons, which in turn are injected into the TiO_2 shell, on the outer surface of which $^1O_2$ production happens. While

we are yet to demonstrate PDT in actual cells using these nanoparticles, I am very optimistic about the future of this work.

I am also very optimistic for the project involving magnetic material and nanophotonics. While plasmon enhanced magnetic switching still has more to offer, I feel that generation of magnons using nanophotonics will be a more lucrative research direction. The excitation of magnons using fs laser pulses have been already reported in literature [223–225]. Incorporating nanophotonics would not only enhance the generation of magnons but also provide well-define nanoscale sources. These sources can be used to address spin qubits like NV-centers in diamond, which have been recently used to demonstrate a solid state quantum processor at room temperature [226]. Some of my colleagues here in Purdue are working in this direction and I hope they can show some exciting results in the near future.

REFERENCES

REFERENCES

[1] H. E. Burton, "The optics of Euclid1," *Jornal of the Optical Society of America*, vol. 35, no. 5, pp. 357–372, 1945.

[2] I. Newton, "A new theory about light and colors," *American Journal of Physics*, vol. 61, no. 2, pp. 108–112, 1993.

[3] L. Mandel and E. Wolf, *Optical Coherence and Quantum Optics*. Cambridge University Press, 1995.

[4] T. H. Maiman, "Stimulated optical radiation in Ruby," *Nature*, vol. 187, no. 4736, pp. 493–494, 1960.

[5] P. Franken, A. Hill, C. Peters, and G. Weinreich, "Generation of optical harmonics," *Physical Review Letters*, vol. 7, no. 4, pp. 118–119, 1961.

[6] R. H. Ritchie, "Plasma losses by fast electrons in thin films," *Physical Review*, vol. 106, pp. 874–881, 1957.

[7] C. J. Powell and J. B. Swan, "Origin of the characteristic electron energy losses in Aluminum," *Physical Review*, vol. 115, pp. 869–875, 1959.

[8] ——, "Origin of the characteristic electron energy losses in Magnesium," *Physical Review*, vol. 116, pp. 81–83, 1959.

[9] E. Kretschmann and H. Raether, "Radiative decay of non radiative surface plasmons excited by light," *Zeitschrift für Naturforschung A*, vol. 23, pp. 2135–2136, 1968.

[10] A. Otto, "Excitation of nonradiative surface plasma waves in silver by the method of frustrated total reflection," *Zeitschrift für Physik A Hadrons and Nuclei*, vol. 216, no. 4, pp. 398–410, 1968.

[11] E. Kretschmann, "Decay of non radiative surface plasmons into light on rough silver films. comparison of experimental and theoretical results," *Optics Communications*, vol. 6, no. 2, pp. 185 – 187, 1972.

[12] S. A. Maier, *Plasmonics : Fundamentals and Applications*, 1st ed. Springer US, 2007.

[13] H. Raether, *Surface Plasmons on Smooth and Rough Surfaces and on Gratings*, 1st ed. Springer-Verlag Berlin Heidelberg, 1988.

[14] C. Haffner, D. Chelladurai, Y. Fedoryshyn, A. Josten, B. Baeuerle, W. Heni, T. Watanabe, T. Cui, B. Cheng, S. Saha, D. L. Elder, L. R. Dalton, A. Boltasseva, V. M. Shalaev, N. Kinsey, and J. Leuthold, "Low-loss plasmon-assisted electro-optic modulator," *Nature*, vol. 556, no. 7702, pp. 483–486, 2018.

[15] J. Burch, D. Wen, X. Chen, and A. Di Falco, "Conformable holographic meta-surfaces," *Scientific Reports*, vol. 7, no. 1, p. 4520, 2017.

[16] K. Wang, E. Schonbrun, P. Steinvurzel, and K. B. Crozier, "Trapping and rotating nanoparticles using a plasmonic nano-tweezer with an integrated heat sink," *Nature Communications*, vol. 2, no. 1, p. 469, 2011.

[17] J. C. Ndukaife, A. V. Kildishev, A. G. A. Nnanna, V. M. Shalaev, S. T. Wereley, and A. Boltasseva, "Long-range and rapid transport of individual nano-objects by a hybrid electrothermoplasmonic nanotweezer," *Nature Nanotechnology*, vol. 11, no. 1, pp. 53–59, 2016.

[18] K. B. Crozier, W. Zhu, D. Wang, S. Lin, M. D. Best, and J. P. Camden, "Plasmonics for surface enhanced raman scattering: Nanoantennas for single molecules," *IEEE Journal of Selected Topics in Quantum Electronics*, vol. 20, no. 3, pp. 152–162, 2014.

[19] X. Ren, E. Cao, W. Lin, Y. Song, W. Liang, and J. Wang, "Recent advances in surface plasmon-driven catalytic reactions," *RSC Advances*, vol. 7, pp. 31 189–31 203, 2017.

[20] A. Naldoni, F. Riboni, U. Guler, A. Boltasseva, V. M. Shalaev, and A. V. Kildishev, "Solar-powered plasmon-enhanced heterogeneous catalysis," *Nanophotonics*, vol. 5, no. 1, pp. 112 – 133, 2016.

[21] M. I. Stockman, "Spasers explained," *Nature Photonics*, vol. 2, no. 6, pp. 327–329, 2008.

[22] M. A. Noginov, G. Zhu, A. M. Belgrave, R. Bakker, V. M. Shalaev, E. E. Narimanov, S. Stout, E. Herz, T. Suteewong, and U. Wiesner, "Demonstration of a spaser-based nanolaser," *Nature*, vol. 460, no. 7259, pp. 1110–1112, 2009.

[23] J. N. Anker, W. P. Hall, O. Lyandres, N. C. Shah, J. Zhao, and R. P. Van Duyne, "Biosensing with plasmonic nanosensors," *Nature Materials*, vol. 7, no. 6, pp. 442–453, 2008.

[24] W. L. Barnes, "Surface plasmon–polariton length scales: a route to sub-wavelength optics," *Journal of Optics A: Pure and Applied Optics*, vol. 8, no. 4, pp. S87–S93, 2006.

[25] P. Berini, "Long-range surface plasmon polaritons," *Advances in Optics and Photonics*, vol. 1, no. 3, pp. 484–588, 2009.

[26] S. Linic, P. Christopher, and D. B. Ingram, "Plasmonic-metal nanostructures for efficient conversion of solar to chemical energy," *Nature Materials*, vol. 10, no. 12, pp. 911–921, 2011.

[27] C. F. Bohren and D. R. Huffman, *Absorption and Scattering of Light by Small Particles*. John Wiley & Sons, Ltd, 1998.

[28] P. K. Jain, K. S. Lee, I. H. El-Sayed, and M. A. El-Sayed, "Calculated absorption and scattering properties of gold nanoparticles of different size, shape, and composition: Applications in biological imaging and biomedicine," *The Journal of Physical Chemistry B*, vol. 110, no. 14, pp. 7238–7248, 2006.

[29] G. Mie, "Beiträge zur optik trüber medien, speziell kolloidaler metallösungen," *Annalen der Physik*, vol. 330, no. 3, pp. 377–445, 1908.

[30] A. Derkachova, K. Kolwas, and I. Demchenko, "Dielectric function for gold in plasmonics applications: Size dependence of plasmon resonance frequencies and damping rates for nanospheres," *Plasmonics*, vol. 11, no. 3, pp. 941–951, 2016.

[31] J. Boken, P. Khurana, S. Thatai, D. Kumar, and S. Prasad, "Plasmonic nanoparticles and their analytical applications: A review," *Applied Spectroscopy Reviews*, vol. 52, no. 9, pp. 774–820, 2017.

[32] H. Fujiwara, *Spectroscopic Ellipsometry*. John Wiley & Sons, Ltd, 2007.

[33] H. Tompkins and E. Irene, *Handbook of Ellipsometry*, H. G. Tompkins and E. A. Irene, Eds. Norwich, NY: William Andrew Publishing, 2005.

[34] X. Huang, P. K. Jain, I. H. El-Sayed, and M. A. El-Sayed, "Gold nanoparticles: interesting optical properties and recent applications in cancer diagnostics and therapy," *Nanomedicine*, vol. 2, no. 5, pp. 681–693, 2007.

[35] A. Huck, S. Smolka, P. Lodahl, A. S. Sørensen, A. Boltasseva, J. Janousek, and U. L. Andersen, "Demonstration of quadrature-squeezed surface plasmons in a gold waveguide," *Physical Review Letters*, vol. 102, p. 246802, 2009.

[36] J. T. Kim, J. J. Ju, S. Park, M. su Kim, S. K. Park, and M.-H. Lee, "Chip-to-chip optical interconnect using gold long-range surface plasmon polariton waveguides," *Optics Express*, vol. 16, no. 17, pp. 13 133–13 138, 2008.

[37] Z. Li, S. Zhang, N. J. Halas, P. Nordlander, and H. Xu, "Coherent modulation of propagating plasmons in silver-nanowire-based structures," *Small*, vol. 7, no. 5, pp. 593–596, 2011.

[38] Y.-J. Lu, J. Kim, H.-Y. Chen, C. Wu, N. Dabidian, C. E. Sanders, C.-Y. Wang, M.-Y. Lu, B.-H. Li, X. Qiu, W.-H. Chang, L.-J. Chen, G. Shvets, C.-K. Shih, and S. Gwo, "Plasmonic nanolaser using epitaxially grown silver film," *Science*, vol. 337, no. 6093, pp. 450–453, 2012.

[39] L. Sun, C. Zhang, C.-Y. Wang, P.-H. Su, M. Zhang, S. Gwo, C.-K. Shih, X. Li, and Y. Wu, "Enhancement of plasmonic performance in epitaxial silver at low temperature," *Scientific Reports*, vol. 7, no. 1, p. 8917, 2017.

[40] M. W. Knight, N. S. King, L. Liu, H. O. Everitt, P. Nordlander, and N. J. Halas, "Aluminum for plasmonics," *ACS Nano*, vol. 8, no. 1, pp. 834–840, 2014.

[41] S. Ramadurgam, T.-G. Lin, and C. Yang, "Aluminum plasmonics for enhanced visible light absorption and high efficiency water splitting in core–multishell nanowire photoelectrodes with ultrathin hematite shells," *Nano Letters*, vol. 14, no. 8, pp. 4517–4522, 2014.

[42] C. Delacour, S. Blaize, P. Grosse, J. M. Fedeli, A. Bruyant, R. Salas-Montiel, G. Lerondel, and A. Chelnokov, "Efficient directional coupling between silicon and copper plasmonic nanoslot waveguides: toward metal-oxide-silicon nanophotonics," *Nano Letters*, vol. 10, no. 8, pp. 2922–2926, 2010.

[43] D. Y. Fedyanin, D. I. Yakubovsky, R. V. Kirtaev, and V. S. Volkov, "Ultralow-loss cmos copper plasmonic waveguides," *Nano Letters*, vol. 16, no. 1, pp. 362–366, 2016.

[44] Q.-C. Sun, Y. Ding, S. M. Goodman, H. H. Funke, and P. Nagpal, "Copper plasmonics and catalysis: role of electron–phonon interactions in dephasing localized surface plasmons," *Nanoscale*, vol. 6, pp. 12 450–12 457, 2014.

[45] J. S. Biggins, S. Yazdi, and E. Ringe, "Magnesium nanoparticle plasmonics," *Nano Letters*, vol. 18, no. 6, pp. 3752–3758, 2018.

[46] J. M. McMahon, G. C. Schatz, and S. K. Gray, "Plasmonics in the ultraviolet with the poor metals al, ga, in, sn, tl, pb, and bi," *Physical Chemistry Chemical Physics*, vol. 15, pp. 5415–5423, 2013.

[47] S. Bagheri, N. Strohfeldt, M. Ubl, A. Berrier, M. Merker, G. Richter, M. Siegel, and H. Giessen, "Niobium as alternative material for refractory and active plasmonics," *ACS Photonics*, vol. 5, no. 8, pp. 3298–3304, 2018.

[48] G. Albrecht, S. Kaiser, H. Giessen, and M. Hentschel, "Refractory plasmonics without refractory materials," *Nano Letters*, vol. 17, no. 10, pp. 6402–6408, 2017.

[49] G. Baraldi, M. Carrada, J. Toudert, F. J. Ferrer, A. Arbouet, V. Paillard, and J. Gonzalo, "Preventing the degradation of ag nanoparticles using an ultrathin a-al2o3 layer as protective barrier," *The Journal of Physical Chemistry C*, vol. 117, no. 18, pp. 9431–9439, 2013.

[50] P. West, S. Ishii, G. Naik, N. Emani, V. Shalaev, and A. Boltasseva, "Searching for better plasmonic materials," *Laser & Photonics Reviews*, vol. 4, no. 6, pp. 795–808, 2010.

[51] G. V. Naik, V. M. Shalaev, and A. Boltasseva, "Alternative plasmonic materials: Beyond gold and silver," *Advanced Materials*, vol. 25, no. 24, pp. 3264–3294, 2013.

[52] G. V. Naik, J. L. Schroeder, X. Ni, A. V. Kildishev, T. D. Sands, and A. Boltasseva, "Titanium nitride as a plasmonic material for visible and near-infrared wavelengths," *Optical Materials Express*, vol. 2, no. 4, pp. 478–489, 2012.

[53] U. Guler, G. V. Naik, A. Boltasseva, V. M. Shalaev, and A. V. Kildishev, "Performance analysis of nitride alternative plasmonic materials for localized surface plasmon applications," *Applied Physics B*, vol. 107, no. 2, pp. 285–291, 2012.

[54] J. A. Briggs, G. V. Naik, T. A. Petach, B. K. Baum, D. Goldhaber-Gordon, and J. A. Dionne, "Fully cmos-compatible titanium nitride nanoantennas," *Applied Physics Letters*, vol. 108, no. 5, p. 051110, 2016.

[55] U. Guler, J. C. Ndukaife, G. V. Naik, A. G. A. Nnanna, A. V. Kildishev, V. M. Shalaev, and A. Boltasseva, "Local heating with lithographically fabricated plasmonic titanium nitride nanoparticles," *Nano Letters*, vol. 13, no. 12, pp. 6078–6083, 2013.

[56] A. Lalisse, G. Tessier, J. Plain, and G. Baffou, "Plasmonic efficiencies of nanoparticles made of metal nitrides (tin, zrn) compared with gold," *Scientific Reports*, vol. 6, no. 1, p. 38647, 2016.

[57] H. W. Lee, G. Papadakis, S. P. Burgos, K. Chander, A. Kriesch, R. Pala, U. Peschel, and H. A. Atwater, "Nanoscale conducting oxide plasmostor," *Nano Letters*, vol. 14, no. 11, pp. 6463–6468, 2014.

[58] J. Kim, A. Dutta, G. V. Naik, A. J. Giles, F. J. Bezares, C. T. Ellis, J. G. Tischler, A. M. Mahmoud, H. Caglayan, O. J. Glembocki, A. V. Kildishev, J. D. Caldwell, A. Boltasseva, and N. Engheta, "Role of epsilon-near-zero substrates in the optical response of plasmonic antennas," *Optica*, vol. 3, no. 3, pp. 339–346, 2016.

[59] L. Caspani, R. P. M. Kaipurath, M. Clerici, M. Ferrera, T. Roger, J. Kim, N. Kinsey, M. Pietrzyk, A. Di Falco, V. M. Shalaev, A. Boltasseva, and D. Faccio, "Enhanced nonlinear refractive index in ϵ-near-zero materials," *Physical Review Letters*, vol. 116, p. 233901, 2016.

[60] M. Z. Alam, I. De Leon, and R. W. Boyd, "Large optical nonlinearity of indium tin oxide in its epsilon-near-zero region," *Science*, vol. 352, no. 6287, pp. 795–797, 2016.

[61] I. V. Bondarev and V. M. Shalaev, "Universal features of the optical properties of ultrathin plasmonic films," *Optical Materials Express*, vol. 7, no. 10, pp. 3731–3740, 2017.

[62] D. Shah, Z. A. Kudyshev, S. Saha, V. M. Shalaev, and A. Boltasseva, "Trans-dimensional material platforms for tunable metasurface design," *MRS Bulletin*, vol. 45, no. 3, p. 188–195, 2020.

[63] A. N. Grigorenko, M. Polini, and K. S. Novoselov, "Graphene plasmonics," *Nature Photonics*, vol. 6, no. 11, pp. 749–758, 2012.

[64] F. J. García de Abajo, "Graphene plasmonics: Challenges and opportunities," *ACS Photonics*, vol. 1, no. 3, pp. 135–152, 2014.

[65] G. X. Ni, A. S. McLeod, Z. Sun, L. Wang, L. Xiong, K. W. Post, S. S. Sunku, B.-Y. Jiang, J. Hone, C. R. Dean, M. M. Fogler, and D. N. Basov, "Fundamental limits to graphene plasmonics," *Nature*, vol. 557, no. 7706, pp. 530–533, 2018.

[66] S. Manzeli, D. Ovchinnikov, D. Pasquier, O. V. Yazyev, and A. Kis, "2d transition metal dichalcogenides," *Nature Reviews Materials*, vol. 2, no. 8, p. 17033, 2017.

[67] J. Zhu, E. Ha, G. Zhao, Y. Zhou, D. Huang, G. Yue, L. Hu, N. Sun, Y. Wang, L. Y. S. Lee, C. Xu, K.-Y. Wong, D. Astruc, and P. Zhao, "Recent advance in mxenes: A promising 2d material for catalysis, sensor and chemical adsorption," *Coordination Chemistry Reviews*, vol. 352, pp. 306 – 327, 2017.

[68] K. Chaudhuri, M. Alhabeb, Z. Wang, V. M. Shalaev, Y. Gogotsi, and A. Boltasseva, "Highly broadband absorber using plasmonic titanium carbide (mxene)," *ACS Photonics*, vol. 5, no. 3, pp. 1115–1122, 2018.

[69] P. Narang, R. Sundararaman, and H. A. Atwater, "Plasmonic hot carrier dynamics in solid-state and chemical systems for energy conversion," *Nanophotonics*, vol. 5, no. 1, pp. 96 – 111, 2016.

[70] M. L. Brongersma, N. J. Halas, and P. Nordlander, "Plasmon-induced hot carrier science and technology," *Nature Nanotechnology*, vol. 10, no. 1, pp. 25–34, 2015.

[71] Y. K. Lee, H. Lee, C. Lee, E. Hwang, and J. Y. Park, "Hot-electron-based solar energy conversion with metal–semiconductor nanodiodes," *Journal of Physics: Condensed Matter*, vol. 28, no. 25, p. 254006, 2016.

[72] J. B. Herzog, M. W. Knight, and D. Natelson, "Thermoplasmonics: Quantifying plasmonic heating in single nanowires," *Nano Letters*, vol. 14, no. 2, pp. 499–503, 2014.

[73] R. S. Riley and E. S. Day, "Gold nanoparticle-mediated photothermal therapy: applications and opportunities for multimodal cancer treatment," *WIREs Nanomedicine and Nanobiotechnology*, vol. 9, no. 4, p. e1449, 2017.

[74] N. Zhou, X. Xu, A. T. Hammack, B. C. Stipe, K. Gao, W. Scholz, and E. C. Gage, "Plasmonic near-field transducer for heat-assisted magnetic recording," *Nanophotonics*, vol. 3, no. 3, pp. 141 – 155, 2014.

[75] Z. Chen, X. Shan, Y. Guan, S. Wang, J.-J. Zhu, and N. Tao, "Imaging local heating and thermal diffusion of nanomaterials with plasmonic thermal microscopy," *ACS Nano*, vol. 9, no. 12, pp. 11 574–11 581, 2015.

[76] T. Bora, D. Zoepfl, and J. Dutta, "Importance of plasmonic heating on visible light driven photocatalysis of gold nanoparticle decorated zinc oxide nanorods," *Scientific Reports*, vol. 6, no. 1, p. 26913, 2016.

[77] A. Fujishima and K. Honda, "Electrochemical photolysis of water at a semiconductor electrode," *Nature*, vol. 238, no. 5358, pp. 37–38, 1972.

[78] M. G. Walter, E. L. Warren, J. R. McKone, S. W. Boettcher, Q. Mi, E. A. Santori, and N. S. Lewis, "Solar water splitting cells," *Chemical Reviews*, vol. 110, no. 11, pp. 6446–6473, 2010.

[79] F. E. Osterloh, "Inorganic nanostructures for photoelectrochemical and photocatalytic water splitting," *Chem. Soc. Rev.*, vol. 42, pp. 2294–2320, 2013.

[80] M. Grätzel, "Photoelectrochemical cells," *Nature*, vol. 414, no. 6861, pp. 338–344, 2001.

[81] A. G. Tamirat, J. Rick, A. A. Dubale, W.-N. Su, and B.-J. Hwang, "Using hematite for photoelectrochemical water splitting: a review of current progress and challenges," *Nanoscale Horizons*, vol. 1, pp. 243–267, 2016.

[82] J. L. Young, M. A. Steiner, H. Döscher, R. M. France, J. A. Turner, and T. Deutsch, "Direct solar-to-hydrogen conversion via inverted metamorphic multi-junction semiconductor architectures," *Nature Energy*, vol. 2, no. 4, p. 17028, 2017.

[83] E. Verlage, S. Hu, R. Liu, R. J. R. Jones, K. Sun, C. Xiang, N. S. Lewis, and H. A. Atwater, "A monolithically integrated, intrinsically safe, 10% efficient, solar-driven water-splitting system based on active, stable earth-abundant electrocatalysts in conjunction with tandem iii–v light absorbers protected by amorphous tio$_2$ films," *Energy Environ. Sci.*, vol. 8, pp. 3166–3172, 2015.

[84] W.-H. Cheng, M. H. Richter, M. M. May, J. Ohlmann, D. Lackner, F. Dimroth, T. Hannappel, H. A. Atwater, and H.-J. Lewerenz, "Monolithic photoelectrochemical device for direct water splitting with 19% efficiency," *ACS Energy Letters*, vol. 3, no. 8, pp. 1795–1800, 2018.

[85] S. Hu, M. R. Shaner, J. A. Beardslee, M. Lichterman, B. S. Brunschwig, and N. S. Lewis, "Amorphous tio$_2$ coatings stabilize si, gaas, and gap photoanodes for efficient water oxidation," *Science*, vol. 344, no. 6187, pp. 1005–1009, 2014.

[86] K. Sun, F. H. Saadi, M. F. Lichterman, W. G. Hale, H.-P. Wang, X. Zhou, N. T. Plymale, S. T. Omelchenko, J.-H. He, K. M. Papadantonakis, B. S. Brunschwig, and N. S. Lewis, "Stable solar-driven oxidation of water by semiconducting photoanodes protected by transparent catalytic nickel oxide films," *Proceedings of the National Academy of Sciences of the United States of America*, vol. 112, no. 12, pp. 3612–3617, 2015.

[87] J. H. Kim, J.-W. Jang, Y. H. Jo, F. F. Abdi, Y. H. Lee, R. van de Krol, and J. S. Lee, "Hetero-type dual photoanodes for unbiased solar water splitting with extended light harvesting," *Nature Communications*, vol. 7, no. 1, p. 13380, 2016.

[88] H.-J. Ahn, A. Goswami, F. Riboni, S. Kment, A. Naldoni, S. Mohajernia, R. Zboril, and P. Schmuki, "Hematite photoanode with complex nanoarchitecture providing tunable gradient doping and low onset potential for photoelectrochemical water splitting," *ChemSusChem*, vol. 11, no. 11, pp. 1873–1879, 2018.

[89] I. Cesar, K. Sivula, A. Kay, R. Zboril, and M. Grätzel, "Influence of feature size, film thickness, and silicon doping on the performance of nanostructured hematite photoanodes for solar water splitting," *The Journal of Physical Chemistry C*, vol. 113, no. 2, pp. 772–782, 2009.

[90] K. Sivula and R. van de Krol, "Semiconducting materials for photoelectrochemical energy conversion," *Nature Reviews Materials*, vol. 1, no. 2, p. 15010, 2016.

[91] T. G. U. Ghobadi, A. Ghobadi, E. Ozbay, and F. Karadas, "Strategies for plasmonic hot-electron-driven photoelectrochemical water splitting," *ChemPhotoChem*, vol. 2, no. 3, pp. 161–182, 2018.

[92] M. Valenti, M. P. Jonsson, G. Biskos, A. Schmidt-Ott, and W. A. Smith, "Plasmonic nanoparticle-semiconductor composites for efficient solar water splitting," *Journal of Materials Chemistry A*, vol. 4, pp. 17 891–17 912, 2016.

[93] N. Wu, "Plasmonic metal–semiconductor photocatalysts and photoelectrochemical cells: a review," *Nanoscale*, vol. 10, pp. 2679–2696, 2018.

[94] A. Naldoni, F. Riboni, U. Guler, A. Boltasseva, V. M. Shalaev, and A. V. Kildishev, "Solar-powered plasmon-enhanced heterogeneous catalysis," *Nanophotonics*, vol. 5, no. 1, pp. 112 – 133, 2016.

[95] T. Klar, M. Perner, S. Grosse, G. von Plessen, W. Spirkl, and J. Feldmann, "Surface-plasmon resonances in single metallic nanoparticles," *Phys. Rev. Lett.*, vol. 80, pp. 4249–4252, 1998.

[96] C. Sönnichsen, T. Franzl, T. Wilk, G. von Plessen, J. Feldmann, O. Wilson, and P. Mulvaney, "Drastic reduction of plasmon damping in gold nanorods," *Phys. Rev. Lett.*, vol. 88, p. 077402, 2002.

[97] S. K. Cushing, J. Li, F. Meng, T. R. Senty, S. Suri, M. Zhi, M. Li, A. D. Bristow, and N. Wu, "Photocatalytic activity enhanced by plasmonic resonant energy transfer from metal to semiconductor," *Journal of the American Chemical Society*, vol. 134, no. 36, pp. 15 033–15 041, 2012.

[98] J. Li, S. K. Cushing, F. Meng, T. R. Senty, A. D. Bristow, and N. Wu, "Plasmon-induced resonance energy transfer for solar energy conversion," *Nature Photonics*, vol. 9, no. 9, pp. 601–607, 2015.

[99] T. Hertel, E. Knoesel, M. Wolf, and G. Ertl, "Ultrafast electron dynamics at cu(111): Response of an electron gas to optical excitation," *Phys. Rev. Lett.*, vol. 76, pp. 535–538, 1996.

[100] F. Ladstädter, U. Hohenester, P. Puschnig, and C. Ambrosch-Draxl, "First-principles calculation of hot-electron scattering in metals," *Phys. Rev. B*, vol. 70, p. 235125, 2004.

[101] H. Inouye, K. Tanaka, I. Tanahashi, and K. Hirao, "Ultrafast dynamics of nonequilibrium electrons in a gold nanoparticle system," *Phys. Rev. B*, vol. 57, pp. 11 334–11 340, 1998.

[102] M. Lisowski, P. A. Loukakos, U. Bovensiepen, J. Stähler, C. Gahl, and M. Wolf, "Ultra-fast dynamics of electron thermalization, cooling and transport effects in ru(001)," *Applied Physics A*, vol. 78, no. 2, pp. 165–176, 2004.

[103] S. Link and M. A. El-Sayed, "Spectral properties and relaxation dynamics of surface plasmon electronic oscillations in gold and silver nanodots and nanorods," *The Journal of Physical Chemistry B*, vol. 103, no. 40, pp. 8410–8426, 1999.

[104] C. Voisin, N. Del Fatti, D. Christofilos, and F. Vallée, "Ultrafast electron dynamics and optical nonlinearities in metal nanoparticles," *The Journal of Physical Chemistry B*, vol. 105, no. 12, pp. 2264–2280, 2001.

[105] G. Baffou and R. Quidant, "Thermo-plasmonics: using metallic nanostructures as nano-sources of heat," *Laser & Photonics Reviews*, vol. 7, no. 2, pp. 171–187, 2013.

[106] G. Baffou, C. Girard, and R. Quidant, "Mapping heat origin in plasmonic structures," *Phys. Rev. Lett.*, vol. 104, p. 136805, 2010.

[107] A. Furube, L. Du, K. Hara, R. Katoh, and M. Tachiya, "Ultrafast plasmon-induced electron transfer from gold nanodots into tio$_2$ nanoparticles," *Journal of the American Chemical Society*, vol. 129, no. 48, pp. 14 852–14 853, 2007.

[108] L. Du, A. Furube, K. Yamamoto, K. Hara, R. Katoh, and M. Tachiya, "Plasmon-induced charge separation and recombination dynamics in gold-tio$_2$ nanoparticle systems: Dependence on tio$_2$ particle size," *The Journal of Physical Chemistry C*, vol. 113, no. 16, pp. 6454–6462, 2009.

[109] R. Long and O. V. Prezhdo, "Instantaneous generation of charge-separated state on tio$_2$ surface sensitized with plasmonic nanoparticles," *Journal of the American Chemical Society*, vol. 136, no. 11, pp. 4343–4354, 2014.

[110] K. Wu, J. Chen, J. R. McBride, and T. Lian, "Efficient hot-electron transfer by a plasmon-induced interfacial charge-transfer transition," *Science*, vol. 349, no. 6248, pp. 632–635, 2015.

[111] L. Mascaretti, A. Dutta, v. Kment, V. M. Shalaev, A. Boltasseva, R. Zbořil, and A. Naldoni, "Plasmon-enhanced photoelectrochemical water splitting for efficient renewable energy storage," *Advanced Materials*, vol. 31, no. 31, p. 1805513, 2019.

[112] M. Valenti, E. Kontoleta, I. A. Digdaya, M. P. Jonsson, G. Biskos, A. Schmidt-Ott, and W. A. Smith, "The role of size and dimerization of decorating plasmonic silver nanoparticles on the photoelectrochemical solar water splitting performance of bivo4 photoanodes," *ChemNanoMat*, vol. 2, no. 7, pp. 739–747, 2016.

[113] P. Peerakiatkhajohn, T. Butburee, J.-H. Yun, H. Chen, R. M. Richards, and L. Wang, "A hybrid photoelectrode with plasmonic au@tio2 nanoparticles for enhanced photoelectrochemical water splitting," *Journal of Materials Chemistry A*, vol. 3, pp. 20 127–20 133, 2015.

[114] P. S. Archana, N. Pachauri, Z. Shan, S. Pan, and A. Gupta, "Plasmonic enhancement of photoactivity by gold nanoparticles embedded in hematite films," *The Journal of Physical Chemistry C*, vol. 119, no. 27, pp. 15 506–15 516, 2015.

[115] U. Kreibig and M. Vollmer, *Optical Properties of Metal Clusters*. Springer-Verlag Berlin Heidelberg, 1995.

[116] H. A. Atwater and A. Polman, "Plasmonics for improved photovoltaic devices," *Nature Materials*, vol. 9, no. 3, pp. 205–213, 2010.

[117] H. Dotan, K. Sivula, M. Grätzel, A. Rothschild, and S. C. Warren, "Probing the photoelectrochemical properties of hematite (α-fe$_2$o$_3$) electrodes using hydrogen peroxide as a hole scavenger," *Energy Environ. Sci.*, vol. 4, pp. 958–964, 2011.

[118] L. Zhang, L. O. Herrmann, and J. J. Baumberg, "Size dependent plasmonic effect on bivo$_4$ photoanodes for solar water splitting," *Scientific Reports*, vol. 5, no. 1, p. 16660, 2015.

[119] Y. K. Lee, C. H. Jung, J. Park, H. Seo, G. A. Somorjai, and J. Y. Park, "Surface plasmon-driven hot electron flow probed with metal-semiconductor nanodiodes," *Nano Letters*, vol. 11, no. 10, pp. 4251–4255, 2011.

[120] M. W. Knight, H. Sobhani, P. Nordlander, and N. J. Halas, "Photodetection with active optical antennas," *Science*, vol. 332, no. 6030, pp. 702–704, 2011.

[121] L. V. Besteiro, X.-T. Kong, Z. Wang, G. Hartland, and A. O. Govorov, "Understanding hot-electron generation and plasmon relaxation in metal nanocrystals: Quantum and classical mechanisms," *ACS Photonics*, vol. 4, no. 11, pp. 2759–2781, 2017.

[122] W. Schottky, "Zur halbleitertheorie der sperrschicht- und spitzengleichrichter," *Zeitschrift für Physik*, vol. 113, no. 5, pp. 367–414, 1939.

[123] N. F. Mott, "The theory of crystal rectifiers," *Proceedings of the Royal Society of London, Series A, Mathematical and Physical Sciences*, vol. 171, no. 944, pp. 27–38, 1939.

[124] R. T. Tung, "The physics and chemistry of the schottky barrier height," *Applied Physics Reviews*, vol. 1, no. 1, p. 011304, 2014.

[125] S.-F. Hung, F.-X. Xiao, Y.-Y. Hsu, N.-T. Suen, H.-B. Yang, H. M. Chen, and B. Liu, "Iridium oxide-assisted plasmon-induced hot carriers: Improvement on kinetics and thermodynamics of hot carriers," *Advanced Energy Materials*, vol. 6, no. 8, p. 1501339, 2016.

[126] J. Sá, G. Tagliabue, P. Friedli, J. Szlachetko, M. H. Rittmann-Frank, F. G. Santomauro, C. J. Milne, and H. Sigg, "Direct observation of charge separation on au localized surface plasmons," *Energy & Environmental Science*, vol. 6, pp. 3584–3588, 2013.

[127] C. R. Crowell, W. G. Spitzer, L. E. Howarth, and E. E. LaBate, "Attenuation length measurements of hot electrons in metal films," *Physical Review*, vol. 127, pp. 2006–2015, 1962.

[128] R. H. Fowler, "The analysis of photoelectric sensitivity curves for clean metals at various temperatures," *Physical Review*, vol. 38, pp. 45–56, 1931.

[129] A. O. Govorov, H. Zhang, and Y. K. Gun'ko, "Theory of photoinjection of hot plasmonic carriers from metal nanostructures into semiconductors and surface molecules," *The Journal of Physical Chemistry C*, vol. 117, no. 32, pp. 16 616–16 631, 2013.

[130] H. Zhang and A. O. Govorov, "Optical generation of hot plasmonic carriers in metal nanocrystals: The effects of shape and field enhancement," *The Journal of Physical Chemistry C*, vol. 118, no. 14, pp. 7606–7614, 2014.

[131] A. M. Brown, R. Sundararaman, P. Narang, W. A. Goddard, and H. A. Atwater, "Nonradiative plasmon decay and hot carrier dynamics: Effects of phonons, surfaces, and geometry," *ACS Nano*, vol. 10, no. 1, pp. 957–966, 2016.

[132] R. Sundararaman, P. Narang, A. S. Jermyn, W. A. Goddard III, and H. A. Atwater, "Theoretical predictions for hot-carrier generation from surface plasmon decay," *Nature Communications*, vol. 5, no. 1, p. 5788, 2014.

[133] A. Manjavacas, J. G. Liu, V. Kulkarni, and P. Nordlander, "Plasmon-induced hot carriers in metallic nanoparticles," *ACS Nano*, vol. 8, no. 8, pp. 7630–7638, 2014.

[134] M. Bernardi, J. Mustafa, J. B. Neaton, and S. G. Louie, "Theory and computation of hot carriers generated by surface plasmon polaritons in noble metals," *Nature Communications*, vol. 6, no. 1, p. 7044, 2015.

[135] J. B. Khurgin, "Hot carriers generated by plasmons: where are they generated and where do they go from there?" *Faraday Discussions*, vol. 214, pp. 35–58, 2019.

[136] G. V. Hartland, L. V. Besteiro, P. Johns, and A. O. Govorov, "What's so hot about electrons in metal nanoparticles?" *ACS Energy Letters*, vol. 2, no. 7, pp. 1641–1653, 2017.

[137] A. Naldoni, U. Guler, Z. Wang, M. Marelli, F. Malara, X. Meng, L. V. Besteiro, A. O. Govorov, A. V. Kildishev, A. Boltasseva, and V. M. Shalaev, "Broadband hot-electron collection for solar water splitting with plasmonic titanium nitride," *Advanced Optical Materials*, vol. 5, no. 15, p. 1601031, 2017.

[138] S. Tan, A. Argondizzo, J. Ren, L. Liu, J. Zhao, and H. Petek, "Plasmonic coupling at a metal/semiconductor interface," *Nature Photonics*, vol. 11, no. 12, pp. 806–812, 2017.

[139] D. A. Wheeler, G. Wang, Y. Ling, Y. Li, and J. Z. Zhang, "Nanostructured hematite: synthesis, characterization, charge carrier dynamics, and photoelectrochemical properties," *Energy & Environmental Science*, vol. 5, pp. 6682–6702, 2012.

[140] K. Sivula, F. Le Formal, and M. Grätzel, "Solar water splitting: Progress using hematite (α-Fe$_2$O$_3$) photoelectrodes," *Chemistry-Sustainability-Energy-Materials*, vol. 4, no. 4, pp. 432–449, 2011.

[141] F. Le Formal, M. Grätzel, and K. Sivula, "Controlling photoactivity in ultrathin hematite films for solar water-splitting," *Advanced Functional Materials*, vol. 20, no. 7, pp. 1099–1107, 2010.

[142] A. Murphy, P. Barnes, L. Randeniya, I. Plumb, I. Grey, M. Horne, and J. Glasscock, "Efficiency of solar water splitting using semiconductor electrodes," *International Journal of Hydrogen Energy*, vol. 31, no. 14, pp. 1999 – 2017, 2006.

[143] A. G. Joly, G. Xiong, C. Wang, D. E. McCready, K. M. Beck, and W. P. Hess, "Synthesis and photoexcited charge carrier dynamics of β-FeOOH nanorods," *Applied Physics Letters*, vol. 90, no. 10, p. 103504, 2007.

[144] N. J. Cherepy, D. B. Liston, J. A. Lovejoy, H. Deng, and J. Z. Zhang, "Ultrafast studies of photoexcited electron dynamics in γ- and α-Fe$_2$O$_3$ semiconductor nanoparticles," *The Journal of Physical Chemistry B*, vol. 102, no. 5, pp. 770–776, 1998.

[145] D. L. Stojić, M. P. Marčeta, S. P. Sovilj, and Šćepan S. Miljanić, "Hydrogen generation from water electrolysis—possibilities of energy saving," *Journal of Power Sources*, vol. 118, no. 1, pp. 315 – 319, 2003.

[146] J. H. Kennedy, "Photooxidation of water at α-Fe$_2$O$_3$ electrodes," *Journal of The Electrochemical Society*, vol. 125, no. 5, p. 709, 1978.

[147] G. Goodlet, S. Faty, S. Cardoso, P. P. Freitas, A. M. P. Simoes, M. G. S. Ferreira, and M. da Cunha Belo, "The electronic properties of sputtered chromium and iron oxide films," *Corrosion Science*, 2004.

[148] I. Cesar, A. Kay, J. A. Gonzalez Martinez, and M. Grätzel, "Translucent thin film fe₂o₃ photoanodes for efficient water splitting by sunlight: Nanostructure-directing effect of si-doping," *Journal of the American Chemical Society*, vol. 128, no. 14, pp. 4582–4583, 2006.

[149] P. Zhang, A. Kleiman-Shwarsctein, Y.-S. Hu, J. Lefton, S. Sharma, A. J. Forman, and E. McFarland, "Oriented ti doped hematite thin film as active photoanodes synthesized by facile apcvd," *Energy Environ. Sci.*, vol. 4, pp. 1020–1028, 2011.

[150] A. Kay, I. Cesar, and M. Grätzel, "New benchmark for water photooxidation by nanostructured α-Fe₂O₃ films," *Journal of the American Chemical Society*, vol. 128, no. 49, pp. 15 714–15 721, 2006.

[151] G. Wang, Y. Ling, D. A. Wheeler, K. E. N. George, K. Horsley, C. Heske, J. Z. Zhang, and Y. Li, "Facile synthesis of highly photoactive α-Fe₂O₃-based films for water oxidation," *Nano Letters*, vol. 11, no. 8, pp. 3503–3509, 2011.

[152] S. D. Tilley, M. Cornuz, K. Sivula, and M. Grätzel, "Light-induced water splitting with hematite: Improved nanostructure and iridium oxide catalysis," *Angewandte Chemie International Edition*, vol. 49, no. 36, pp. 6405–6408, 2010.

[153] S. J. Kim, I. Thomann, J. Park, J.-H. Kang, A. P. Vasudev, and M. L. Brongersma, "Light trapping for solar fuel generation with mie resonances," *Nano Letters*, vol. 14, no. 3, pp. 1446–1452, 2014.

[154] J. Li, S. K. Cushing, P. Zheng, F. Meng, D. Chu, and N. Wu, "Plasmon-induced photonic and energy-transfer enhancement of solar water splitting by a hematite nanorod array," *Nature Communications*, vol. 4, no. 1, p. 2651, 2013.

[155] I. Thomann, B. A. Pinaud, Z. Chen, B. M. Clemens, T. F. Jaramillo, and M. L. Brongersma, "Plasmon enhanced solar-to-fuel energy conversion," *Nano Letters*, vol. 11, no. 8, pp. 3440–3446, 2011.

[156] E. Thimsen, F. Le Formal, M. Grätzel, and S. C. Warren, "Influence of plasmonic au nanoparticles on the photoactivity of fe₂o₃ electrodes for water splitting," *Nano Letters*, vol. 11, no. 1, pp. 35–43, 2011.

[157] H. Gao, C. Liu, H. E. Jeong, and P. Yang, "Plasmon-enhanced photocatalytic activity of iron oxide on gold nanopillars," *ACS Nano*, vol. 6, no. 1, pp. 234–240, 2012.

[158] M. G. Nielsen, D. K. Gramotnev, A. Pors, O. Albrektsen, and S. I. Bozhevolnyi, "Continuous layer gap plasmon resonators," *Opt. Express*, vol. 19, no. 20, pp. 19 310–19 322, 2011.

[159] D. O. Sigle, L. Zhang, S. Ithurria, B. Dubertret, and J. J. Baumberg, "Ultrathin cdse in plasmonic nanogaps for enhanced photocatalytic water splitting," *The Journal of Physical Chemistry Letters*, vol. 6, no. 7, pp. 1099–1103, 2015.

[160] A. Dutta, A. Naldoni, F. Malara, A. O. Govorov, V. M. Shalaev, and A. Boltasseva, "Gap-plasmon enhanced water splitting with ultrathin hematite films: the role of plasmonic-based light trapping and hot electrons," *Faraday Discussions*, vol. 214, pp. 283–295, 2019.

[161] I. V. Chernyshova, M. F. Hochella Jr, and A. S. Madden, "Size-dependent structural transformations of hematite nanoparticles. 1. phase transition," *Physical Chemistry Chemical Physics*, vol. 9, pp. 1736–1750, 2007.

[162] Z. Liu, W. Hou, P. Pavaskar, M. Aykol, and S. B. Cronin, "Plasmon resonant enhancement of photocatalytic water splitting under visible illumination," *Nano Letters*, vol. 11, no. 3, pp. 1111–1116, 2011.

[163] Y. Fang, Y. Jiao, K. Xiong, R. Ogier, Z.-J. Yang, S. Gao, A. B. Dahlin, and M. Käll, "Plasmon enhanced internal photoemission in antenna-spacer-mirror based au/tio$_2$ nanostructures," *Nano Letters*, vol. 15, no. 6, pp. 4059–4065, 2015.

[164] S. Dal Forno, L. Ranno, and J. Lischner, "Material, size, and environment dependence of plasmon-induced hot carriers in metallic nanoparticles," *The Journal of Physical Chemistry C*, vol. 122, no. 15, pp. 8517–8527, 2018.

[165] A. R. Khorsand, "Spectroscopic study of ultrafast laser-induced magnetization reversal," Ph.D. dissertation, Radboud University Nijmegen, 2013.

[166] R. Ramaswamy, J. M. Lee, K. Cai, and H. Yang, "Recent advances in spin-orbit torques: Moving towards device applications," *Applied Physics Reviews*, vol. 5, no. 3, p. 031107, 2018.

[167] J. Stöhr and H. C. Siegmann, *Magnetism, From Fundamentals to Nanoscale Dynamics.* Springer-Verlag Berlin Heidelberg, 2006.

[168] S. Datta, *Lessons from Nanoelectronics*, 2nd ed. World Scientific, 2018.

[169] W. K. Hiebert, G. E. Ballentine, and M. R. Freeman, "Comparison of experimental and numerical micromagnetic dynamics in coherent precessional switching and modal oscillations," *Physical Review B*, vol. 65, p. 140404, 2002.

[170] C. H. Back, R. Allenspach, W. Weber, S. S. P. Parkin, D. Weller, E. L. Garwin, and H. C. Siegmann, "Minimum field strength in precessional magnetization reversal," *Science*, vol. 285, no. 5429, pp. 864–867, 1999.

[171] H. W. Schumacher, C. Chappert, R. C. Sousa, P. P. Freitas, and J. Miltat, "Quasiballistic magnetization reversal," *Physical Review Letters*, vol. 90, p. 017204, 2003.

[172] I. Tudosa, C. Stamm, A. B. Kashuba, F. King, H. C. Siegmann, J. Stöhr, G. Ju, B. Lu, and D. Weller, "The ultimate speed of magnetic switching in granular recording media," *Nature*, vol. 428, no. 6985, pp. 831–833, 2004.

[173] J. Slonczewski, "Current-driven excitation of magnetic multilayers," *Journal of Magnetism and Magnetic Materials*, vol. 159, no. 1, pp. L1 − L7, 1996.

[174] L. Berger, "Emission of spin waves by a magnetic multilayer traversed by a current," *Physical Review B*, vol. 54, pp. 9353–9358, 1996.

[175] E. B. Myers, D. C. Ralph, J. A. Katine, R. N. Louie, and R. A. Buhrman, "Current-induced switching of domains in magnetic multilayer devices," *Science*, vol. 285, no. 5429, pp. 867–870, 1999.

[176] J. A. Katine, F. J. Albert, R. A. Buhrman, E. B. Myers, and D. C. Ralph, "Current-driven magnetization reversal and spin-wave excitations in co /cu /co pillars," *Physical Review Letters*, vol. 84, pp. 3149–3152, 2000.

[177] S. Ikeda, K. Miura, H. Yamamoto, K. Mizunuma, H. D. Gan, M. Endo, S. Kanai, J. Hayakawa, F. Matsukura, and H. Ohno, "A perpendicular-anisotropy cofeb–mgo magnetic tunnel junction," *Nature Materials*, vol. 9, no. 9, pp. 721–724, 2010.

[178] H. Sato, E. C. I. Enobio, M. Yamanouchi, S. Ikeda, S. Fukami, S. Kanai, F. Matsukura, and H. Ohno, "Properties of magnetic tunnel junctions with a mgo/cofeb/ta/cofeb/mgo recording structure down to junction diameter of 11 nm," *Applied Physics Letters*, vol. 105, no. 6, p. 062403, 2014.

[179] M. D'yakonov and V. Perel, "Possibility of orienting electron spins with current," *JETP Letters*, vol. 13, no. 11, p. 467, 1971.

[180] J. Sinova, S. O. Valenzuela, J. Wunderlich, C. H. Back, and T. Jungwirth, "Spin hall effects," *Reviews of Modern Physics*, vol. 87, pp. 1213–1260, 2015.

[181] T. Jungwirth, J. Wunderlich, and K. Olejník, "Spin hall effect devices," *Nature Materials*, vol. 11, no. 5, pp. 382–390, 2012.

[182] L. Liu, C.-F. Pai, Y. Li, H. W. Tseng, D. C. Ralph, and R. A. Buhrman, "Spin-torque switching with the giant spin hall effect of tantalum," *Science*, vol. 336, no. 6081, pp. 555–558, 2012.

[183] I. M. Miron, K. Garello, G. Gaudin, P.-J. Zermatten, M. V. Costache, S. Auffret, S. Bandiera, B. Rodmacq, A. Schuhl, and P. Gambardella, "Perpendicular switching of a single ferromagnetic layer induced by in-plane current injection," *Nature*, vol. 476, no. 7359, pp. 189–193, 2011.

[184] L. Pan and D. B. Bogy, "Heat-assisted magnetic recording," *Nature Photonics*, vol. 3, no. 4, pp. 189–190, 2009.

[185] R. E. Rottmayer, S. Batra, D. Buechel, W. A. Challener, J. Hohlfeld, Y. Kubota, L. Li, B. Lu, C. Mihalcea, K. Mountfield, K. Pelhos, C. Peng, T. Rausch, M. A. Seigler, D. Weller, and X. . Yang, "Heat-assisted magnetic recording," *IEEE Transactions on Magnetics*, vol. 42, no. 10, pp. 2417–2421, 2006.

[186] W. A. Challener, C. Peng, A. V. Itagi, D. Karns, W. Peng, Y. Peng, X. Yang, X. Zhu, N. J. Gokemeijer, Y.-T. Hsia, G. Ju, R. E. Rottmayer, M. A. Seigler, and E. C. Gage, "Heat-assisted magnetic recording by a near-field transducer with efficient optical energy transfer," *Nature Photonics*, vol. 3, no. 4, pp. 220–224, 2009.

[187] E. X. Jin and X. Xu, "Plasmonic effects in near-field optical transmission enhancement through a single bowtie-shaped aperture," *Applied Physics B*, vol. 84, no. 1, pp. 3–9, 2006.

[188] D. Weller, G. Parker, O. Mosendz, A. Lyberatos, D. Mitin, N. Y. Safonova, and M. Albrecht, "Review article: Fept heat assisted magnetic recording media," *Journal of Vacuum Science & Technology B*, vol. 34, no. 6, p. 060801, 2016.

[189] P. Lu and S. H. Charap, "Magnetic viscosity in high-density recording," *Journal of Applied Physics*, vol. 75, no. 10, pp. 5768–5770, 1994.

[190] E. Beaurepaire, J.-C. Merle, A. Daunois, and J.-Y. Bigot, "Ultrafast spin dynamics in ferromagnetic nickel," *Phys. Rev. Lett.*, vol. 76, pp. 4250–4253, 1996.

[191] A. Kirilyuk, A. V. Kimel, and T. Rasing, "Ultrafast optical manipulation of magnetic order," *Review of Modern Physics*, vol. 82, pp. 2731–2784, 2010.

[192] C. D. Stanciu, A. V. Kimel, F. Hansteen, A. Tsukamoto, A. Itoh, A. Kirilyuk, and T. Rasing, "Ultrafast spin dynamics across compensation points in ferrimagnetic GdFeCo: The role of angular momentum compensation," *Phys. Rev. B*, vol. 73, p. 220402, 2006.

[193] I. Radu, K. Vahaplar, C. Stamm, T. Kachel, N. Pontius, H. A. Dürr, T. A. Ostler, J. Barker, R. F. L. Evans, R. W. Chantrell, A. Tsukamoto, A. Itoh, A. Kirilyuk, T. Rasing, and A. V. Kimel, "Transient ferromagnetic-like state mediating ultrafast reversal of antiferromagnetically coupled spins," *Nature*, vol. 472, no. 7342, pp. 205–208, 2011.

[194] C. E. Graves, A. H. Reid, T. Wang, B. Wu, S. de Jong, K. Vahaplar, I. Radu, D. P. Bernstein, M. Messerschmidt, L. Müller, R. Coffee, M. Bionta, S. W. Epp, R. Hartmann, N. Kimmel, G. Hauser, A. Hartmann, P. Holl, H. Gorke, J. H. Mentink, A. Tsukamoto, A. Fognini, J. J. Turner, W. F. Schlotter, D. Rolles, H. Soltau, L. Strüder, Y. Acremann, A. V. Kimel, A. Kirilyuk, T. Rasing, J. Stöhr, A. O. Scherz, and H. A. Dürr, "Nanoscale spin reversal by non-local angular momentum transfer following ultrafast laser excitation in ferrimagnetic GdFeCo," *Nature Materials*, vol. 12, no. 4, pp. 293–298, 2013.

[195] M. Krauß, T. Roth, S. Alebrand, D. Steil, M. Cinchetti, M. Aeschlimann, and H. C. Schneider, "Ultrafast demagnetization of ferromagnetic transition metals: The role of the coulomb interaction," *Physical Review B*, vol. 80, p. 180407, 2009.

[196] J.-Y. Bigot, M. Vomir, and E. Beaurepaire, "Coherent ultrafast magnetism induced by femtosecond laser pulses," *Nature Physics*, vol. 5, no. 7, pp. 515–520, 2009.

[197] H. Vonesch and J.-Y. Bigot, "Ultrafast spin-photon interaction investigated with coherent magneto-optics," *Physical Review B*, vol. 85, p. 180407, 2012.

[198] B. Koopmans, J. J. M. Ruigrok, F. D. Longa, and W. J. M. de Jonge, "Unifying ultrafast magnetization dynamics," *Physical Review Letters*, vol. 95, p. 267207, 2005.

[199] K. Carva, M. Battiato, D. Legut, and P. M. Oppeneer, "Ab initio theory of electron-phonon mediated ultrafast spin relaxation of laser-excited hot electrons in transition-metal ferromagnets," *Physical Review B*, vol. 87, p. 184425, 2013.

[200] E. Carpene, E. Mancini, C. Dallera, M. Brenna, E. Puppin, and S. De Silvestri, "Dynamics of electron-magnon interaction and ultrafast demagnetization in thin iron films," *Physical Review B*, vol. 78, p. 174422, 2008.

[201] A. B. Schmidt, M. Pickel, M. Donath, P. Buczek, A. Ernst, V. P. Zhukov, P. M. Echenique, L. M. Sandratskii, E. V. Chulkov, and M. Weinelt, "Ultrafast magnon generation in an fe film on cu(100)," *Physical Review Letters*, vol. 105, p. 197401, 2010.

[202] C. Stamm, T. Kachel, N. Pontius, R. Mitzner, T. Quast, K. Holldack, S. Khan, C. Lupulescu, E. F. Aziz, M. Wietstruk, H. A. Dürr, and W. Eberhardt, "Femtosecond modification of electron localization and transfer of angular momentum in nickel," *Nature Materials*, vol. 6, no. 10, pp. 740–743, 2007.

[203] C. Boeglin, E. Beaurepaire, V. Halté, V. López-Flores, C. Stamm, N. Pontius, H. A. Dürr, and J.-Y. Bigot, "Distinguishing the ultrafast dynamics of spin and orbital moments in solids," *Nature*, vol. 465, no. 7297, pp. 458–461, 2010.

[204] S. Mathias, C. La-O-Vorakiat, P. Grychtol, P. Granitzka, E. Turgut, J. M. Shaw, R. Adam, H. T. Nembach, M. E. Siemens, S. Eich, C. M. Schneider, T. J. Silva, M. Aeschlimann, M. M. Murnane, and H. C. Kapteyn, "Probing the timescale of the exchange interaction in a ferromagnetic alloy," *Proceedings of the National Academy of Sciences*, vol. 109, no. 13, pp. 4792–4797, 2012.

[205] C. D. Stanciu, F. Hansteen, A. V. Kimel, A. Kirilyuk, A. Tsukamoto, A. Itoh, and T. Rasing, "All-optical magnetic recording with circularly polarized light," *Phys. Rev. Lett.*, vol. 99, p. 047601, 2007.

[206] K. Vahaplar, A. M. Kalashnikova, A. V. Kimel, S. Gerlach, D. Hinzke, U. Nowak, R. Chantrell, A. Tsukamoto, A. Itoh, A. Kirilyuk, and T. Rasing, "All-optical magnetization reversal by circularly polarized laser pulses: Experiment and multiscale modeling," *Phys. Rev. B*, vol. 85, p. 104402, 2012.

[207] J. H. Mentink, J. Hellsvik, D. V. Afanasiev, B. A. Ivanov, A. Kirilyuk, A. V. Kimel, O. Eriksson, M. I. Katsnelson, and T. Rasing, "Ultrafast spin dynamics in multisublattice magnets," *Phys. Rev. Lett.*, vol. 108, p. 057202, 2012.

[208] L. Le Guyader, S. El Moussaoui, M. Buzzi, R. V. Chopdekar, L. J. Heyderman, A. Tsukamoto, A. Itoh, A. Kirilyuk, T. Rasing, A. V. Kimel, and F. Nolting, "Demonstration of laser induced magnetization reversal in GdFeCo nanostructures," *Applied Physics Letters*, vol. 101, no. 2, p. 022410, 2012.

[209] R. B. Wilson, J. Gorchon, Y. Yang, C.-H. Lambert, S. Salahuddin, and J. Bokor, "Ultrafast magnetic switching of GdFeCo with electronic heat currents," *Phys. Rev. B*, vol. 95, p. 180409, 2017.

[210] S. Mangin, M. Gottwald, C.-H. Lambert, D. Steil, V. Uhlíř, L. Pang, M. Hehn, S. Alebrand, M. Cinchetti, G. Malinowski, Y. Fainman, M. Aeschlimann, and E. E. Fullerton, "Engineered materials for all-optical helicity-dependent magnetic switching," *Nature Materials*, vol. 13, pp. 286–292, 2014.

[211] M. Beens, M. L. M. Lalieu, A. J. M. Deenen, R. A. Duine, and B. Koopmans, "Comparing all-optical switching in synthetic-ferrimagnetic multilayers and alloys," *Phys. Rev. B*, vol. 100, p. 220409, 2019.

[212] C.-H. Lambert, S. Mangin, B. S. D. C. S. Varaprasad, Y. K. Takahashi, M. Hehn, M. Cinchetti, G. Malinowski, K. Hono, Y. Fainman, M. Aeschlimann, and E. E. Fullerton, "All-optical control of ferromagnetic thin films and nanostructures," *Science*, vol. 345, no. 6202, pp. 1337–1340, 2014.

[213] M. O. A. Ellis, E. E. Fullerton, and R. W. Chantrell, "All-optical switching in granular ferromagnets caused by magnetic circular dichroism," *Scientific Reports*, vol. 6, no. 1, p. 30522, 2016.

[214] J. Gorchon, C.-H. Lambert, Y. Yang, A. Pattabi, R. B. Wilson, S. Salahuddin, and J. Bokor, "Single shot ultrafast all optical magnetization switching of ferromagnetic Co/Pt multilayers," *Applied Physics Letters*, vol. 111, no. 4, p. 042401, 2017.

[215] P. S. Pershan, J. P. van der Ziel, and L. D. Malmstrom, "Theoretical discussion of the inverse faraday effect, raman scattering, and related phenomena," *Physical Review*, vol. 143, pp. 574–583, 1966.

[216] A. Dutta, A. V. Kildishev, V. M. Shalaev, A. Boltasseva, and E. E. Marinero, "Surface-plasmon opto-magnetic field enhancement for all-optical magnetization switching," *Optical Materials Express*, vol. 7, no. 12, pp. 4316–4327, 2017.

[217] T.-M. Liu, T. Wang, A. H. Reid, M. Savoini, X. Wu, B. Koene, P. Granitzka, C. E. Graves, D. J. Higley, Z. Chen, G. Razinskas, M. Hantschmann, A. Scherz, J. Stöhr, A. Tsukamoto, B. Hecht, A. V. Kimel, A. Kirilyuk, T. Rasing, and H. A. Dürr, "Nanoscale confinement of all-optical magnetic switching in TbFeCo - competition with nanoscale heterogeneity," *Nano Letters*, vol. 15, no. 10, pp. 6862–6868, 2015.

[218] D. O. Ignatyeva, C. S. Davies, D. A. Sylgacheva, A. Tsukamoto, H. Yoshikawa, P. O. Kapralov, A. Kirilyuk, V. I. Belotelov, and A. V. Kimel, "Plasmonic layer-selective all-optical switching of magnetization with nanometer resolution," *Nature Communications*, vol. 10, no. 1, p. 4786, 2019.

[219] A. R. Khorsand, M. Savoini, A. Kirilyuk, A. V. Kimel, A. Tsukamoto, A. Itoh, and T. Rasing, "Role of magnetic circular dichroism in all-optical magnetic recording," *Physcal Review Letters*, vol. 108, p. 127205, 2012.

[220] S. Lal, S. E. Clare, and N. J. Halas, "Nanoshell-enabled photothermal cancer therapy: Impending clinical impact," *Accounts of Chemical Research*, vol. 41, no. 12, pp. 1842–1851, 2008.

[221] Á. Juarranz, P. Jaén, F. Sanz-Rodríguez, J. Cuevas, and S. González, "Photodynamic therapy of cancer. basic principles and applications," *Clinical and Translational Oncology*, vol. 10, no. 3, pp. 148–154, 2008.

[222] X. Xu, A. Dutta, J. Khurgin, A. Wei, V. M. Shalaev, and A. Boltasseva, "Plasmonic photosensitizers: $TiN@TiO_2$ core–shell nanoparticles as plasmon-enhanced photosensitizers: The role of hot electron injection," *Laser & Photonics Reviews*, vol. 14, no. 5, p. 2070031, 2020.

[223] I. Yoshimine, T. Satoh, R. Iida, A. Stupakiewicz, A. Maziewski, and T. Shimura, "Phase-controllable spin wave generation in iron garnet by linearly polarized light pulses," *Journal of Applied Physics*, vol. 116, no. 4, p. 043907, 2014.

[224] M. Deb, M. Vomir, J.-L. Rehspringer, and J.-Y. Bigot, "Ultrafast optical control of magnetization dynamics in polycrystalline bismuth doped iron garnet thin films," *Applied Physics Letters*, vol. 107, no. 25, p. 252404, 2015.

[225] A. V. Kimel, A. Kirilyuk, P. A. Usachev, R. V. Pisarev, A. M. Balbashov, and T. Rasing, "Ultrafast non-thermal control of magnetization by instantaneous photomagnetic pulses," *Nature*, vol. 435, no. 7042, pp. 655–657, 2005.

[226] Y. Wu, Y. Wang, X. Qin, X. Rong, and J. Du, "A programmable two-qubit solid-state quantum processor under ambient conditions," *npj Quantum Information*, vol. 5, no. 1, p. 9, 2019.

VITA

VITA

I, Aveek Dutta, obtained my Master of Technology from the Instrumentation and Applied Physics department at the Indian Institute of Science, Bangalore in 2013. During that time, I worked on the concept of self-healing circuits and thermodynamic computing based on combined drift-diffusion of nanoparticles in an applied electric field. Prior to that I obtained my Bachelor degree from the Department of Instrumentation and Electronics Engineering at Jadavpur University, Kolkata, India in 2011. During that time, I worked on heuristic algorithms for clustering and classification. I also worked on the software design of an automated three-axis gimbals system for motion tracking.

At Purdue, I have been working in the joint research group of Prof. Vladimir M. Shalaev and Prof. Alexandra Boltasseva. My research is in the field of plasmonics. Specifically I have studied the role of plasmonics for addressing solar energy harvesting and magnetization reversal for high density magnetic memory devices. Through my research I have contributed to 12 peer-reviewed journal articles to date. Besides research, I have served as the President of the Nanotechnology Student Advisory Council at Birck Nanotechnology Center in Purdue for the academic year 2016-17. I have also served as an office bearer for the OSA and SPIE Purdue Student Chapter, during which time I have participated in organising in-house technical conferences as well as workshops and demos for the general public interested in scientific research. I have also served as a Graduate Ambassador for the Birck Nanotechnology Center and provided over 50 tours to individuals ranging from government officials to high school and middle school students.